Dynamics and Shear Alignment Behavior of a Model Thermotropic Liquid Crystalline Polymer

Thesis by

Weijun Zhou

In Partial Fulfillment of the Requirements

for the Degree of

Doctor of Philosophy

California Institute of Technology

Pasadena, California

2001

(Defended September 29, 2000)

To my parents

Abstract

Although liquid crystalline polymers (LCPs) emerged as important engineering materials in the early 1970s, the current level of understanding still falls short of allowing deliberate manipulation of macroscopic orientation, leading to poor control of morphology and material properties. The flow behavior of rod-like LCP solutions (lyotropic) are fairly well understood, yet little progress has been made on LCP melts (thermotropic) because of the formidable experimental difficulties with commercial thermotropes. A simple extension of the knowledge obtained from rod-like LCP solutions to thermotropic LCPs is unlikely to hold due to the enhanced molecular flexibility and intimate molecular contact in LCP melts.

The primary concern of this thesis is therefore the flow behavior of thermotropic LCPs, with an emphasis on how flow influences orientation and morphology and how this depends on molecular structure. For this purpose we synthesized a model thermotropic LCP selected for its chemical stability, wide nematic range and optical transparency. This main-chain LCP, designated as DHMS-7,9, has alternating mesogen and spacer structure with dihydroxy-α-methylstilbene as mesogen and two different lengths of alkyl spacers (-C_7H_{14}- and -C_9H_{18}-). A range of molecular weights were prepared to probe the effects of chain flexibility (ratio of chain length of persistence length). Synthesis was scaled up to provide adequate quantities for physical studies (rheology, rheo-conoscopy and rheo-WAXS).

The director response of a monodomain during shear flow is followed by *in situ* optical conoscopy using a custom-made shear cell. We observe that the director rotates opposite to the vorticity in shear for DHMS-7,9 using planar monodomain samples, demonstrating conclusively that it is flow aligning throughout its nematic temperature range. Director rotation is solely a function of applied strain, independent of shear rate, showing that the Leslie-Ericksen theory is applicable to polymeric nematics for shear rates that are low relative to their molecular relaxation. Comparisons of the observed tumbling parameter of DHMS-7,9 with predictions from available molecular models lead us to infer that molecular flexibility produces shear alignment for this class of thermotropic LCPs. To identify the effect of chain flexibility on the dynamics of this LCP, the rotational viscosity and shear viscosity were measured as functions of molecular weight. Both viscosities showed

weaker sensitivity to molecular weight above a characteristic molecular weight, suggesting a crossover to semiflexible character at high molecular weight.

Rheology and shear orientation behavior of DHMS-7,9 are markedly different from that of nematic lyotropic LCPs. Synchrotron WAXS measurements in steady shear show that molecular orientation is relatively high and nearly independent of shear rate. In transient shear during flow inception, flow reversal, and step up/down shear rate, neither shear stress nor orientation parameter shows multiple oscillations. Thus, both steady and transient responses of DHMS-7,9 are characteristic of flow-aligning liquid crystals, in contrast to tumbling rod-like LCPs, which show complex shear rate dependence in steady shear and oscillatory response to these transient flows.

An interesting feature of DHMS-7,9 is the existence of a mysterious liquid crystalline phase—Phase X. The flow behavior of Phase X is completely different from that of the nematic phase. A striking flip of the orientation from the flow direction to the vorticity direction occurs below a critical shear rate. This orientational flipping is reversible in response to step changes of temperature and/or shear rate. In addition, we found that oscillatory shear flow also induces a similar type of orientational flipping. Examination of the linear viscoelastic properties as a function of orientation in Phase X suggests rheological similarity to layered fluids.

Acknowledgements

I have been very fortunate to have met many special people and friends who have contributed to my education and learning. Without them, my success would not have been possible and they all deserve my heartfelt thanks.

First and foremost, I would like to thank my academic advisor, Professor Julia Kornfield, for her tremendous enthusiasm, constant support, and unfailing patience with me over the past five years. I am very grateful to her for allowing me considerable freedom in conducting this research while simultaneously exacting her very high standards and keen insights. I would also like to thank my committee members, Professor Zhen-Gang Wang, Professor David Tirrell and Professor George Gavalas for their interest and insight to my thesis.

This work has greatly benefited from collaboration with people outside Caltech. I am deeply indebted to Victor Ugaz, Nitin Vaish and Professor Wesley Burghardt at Northwestern University. Victor performed beautiful X-ray scattering experiments that have been described in this thesis, and numerous interactions between two of us have been helping me tremendously to refine my understanding of liquid crystalline polymer dynamics. He set up a model for me how to implement and enjoy research collaboration in the future. Nitin helped me to pursue some oscillatory shear alignment studies of DHMS-7,9. Professor Burghardt has been key in teaching me the ins and outs of polymer rheology, and his support and willingness to answer even the most mundane questions seemed endless! I am also grateful to Scott Clingman and Professor Chris Ober at Cornell University for help and discussion concerning scale-up synthesis. Thanks are also due to Darren Link and Professor Noel Clark at University of Colorado for help on high resolution powder X-ray diffraction experiments. I would also like to thank Professor Peter Palffy-Muhoray at Liquid Crystal Institute of Kent State University for teaching me how to prepare liquid crystal alignment layer, Professor George Rossman at Caltech, Professor Pat Mather at University of Connecticut and Professor Mohan Srinivasarao at Georgia Institute of Technology for many helpful discussions and insights on optical conoscopy.

I would like to express my sincere appreciation to members of Kornfield group, all current (Giyoong, Mike, Wei, Eric, Derek, Jagdish, Chris, James) and past (Susan, Zhong-

Ren, Sunil, Guru, Ani), who have provided a great work environment. I would especially like to thank Guru for innumerable stimulating discussions over years; Jagdish, for his expert advice on polymer synthesis as well as many other lab unrelated things. Zhong-Ren, my "buddy" ever since I was a still prospective student, has helped me in various ways to adjust to life at Caltech. I would be remiss if I failed to acknowledge our group secretary, Anne Hormann, for keeping everything in the group running smoothly and for voluntarily helping me to improve my English writing. Thanks are also due to Suresh Gupta who serves as an indispensable resource for computer-related problems.

I owe an incredibly huge amount to my family. My father has been key to my success at various stages of study, and I will forever be grateful to him for teaching me the value of learning although he passed away in the summer of 1997. My mother may never understand why I need to stay in the school for such a long time, yet her unwavering love and support, in a different way from my father, has been felt clearly despite the distance. I also want to thank my sister for encouraging me to study abroad and for all the good days we spent together.

My deepest gratitude goes to my wife, Lin, for her understanding, support and love. Her companionship and tenderness has made my graduate life much more enjoyable, and I simply wish I could do the same for her as we embark on a new life at the east coast.

Contents

Abstract iv

Acknowledgements vi

1 Background 1

1.1 Introduction 1

1.2 Structure of LCPs from Å to μm 2

1.2.1 Liquid Crystalline Phases 2

1.2.2 Molecular Architecture of LCPs 4

1.2.3 Orientation at Continuum Level 6

1.2.4 Defects and Polydomain Textures 7

1.3 Flow Behavior of LCPs 9

1.3.1 Director Tumbling and Flow-Aligning 9

1.3.2 Rheology of Thermotropic LCPs vs. Lyotropic LCPs 12

1.4 Role of Chain Flexibility in LCP Dynamics 13

1.4.1 The Doi Model of Rod-like LCPs 14

1.4.2 Incorporating Chain Flexibility in Molecular Models 15

1.4.3 Crossover from Rod-like to Semiflexible Behavior 16

1.5 Objectives and Thesis Organization 16

Bibliography 18

2 Quantitative Determination of Shear Aligning Properties 21

2.1 Introduction 21

2.2 Experimental Section 23

2.3 Conoscopy and Data Analysis 24

2.4 Results 26

2.4.1 Qualitative Determination of Shear Aligning vs. Tumbling Character 26

2.4.2 Quantitative Determination of the Tumbling Parameter λ 26

2.4.3 Temperature Dependence of the Tumbling Parameter 27
2.4.4 Temperature Dependence of the Order Parameter 28
2.4.5 Transient Director Response 29
2.5 Discussion 30
2.5.1 A Unifying View of Aligning Properties for Mesogen-spacer LCP . . 30
2.5.2 Comparison of $\lambda(S)$ with Small Molecule LCs 30
2.5.3 Comparisons with Molecular Models 31
2.5.4 Physical Insights for the Effect of Flexibility 32
2.6 Conclusion 32
Bibliography 44

3 Rheology and Shear Orientation in the Nematic Phase **47**
3.1 Introduction 47
3.2 Experimental Section 48
3.2.1 Materials and Characterization 48
3.2.2 Rheological Measurements 49
3.2.3 Rheo-X-ray Protocol and Data Analysis 50
3.3 Linear Viscoelastic Behavior 51
3.4 Steady Shear Rheology and Orientation 52
3.4.1 Flow Curve 52
3.4.2 Orientation in Steady Shear 52
3.5 Transient Shear Rheology and Orientation 54
3.5.1 Relaxation Following Cessation of Steady Shear 54
3.5.2 Rheology and Orientation During Flow Inception 55
3.5.3 Rheology During Step Up/Down Flow 55
3.5.4 Rheology and Orientation During Flow Reversal 56
3.5.5 Rheology and Orientation During Non-Steady-State Reversal 56
3.5.6 Rheology and Orientation During Oscillatory Shear 57
3.6 Model Predictions of Rheology and Orientation 58
3.6.1 Prediction of Orientation Development 59
3.6.2 Prediction of Shear Stress 59
3.7 Discussion 60

3.7.1 Steady Shear Flow 60
3.7.2 Transient Shear Flow 62
3.7.3 Success and Limitation of Ericksen Polydomain Model 62
3.8 Conclusions 63
Bibliography 83

4 Effect of Molecular Weight on Viscous Properties of a Main Chain LCP 85
4.1 Introduction 85
4.2 Experimental Section 87
4.2.1 Materials and Characterization 87
4.2.2 Magnetic Alignment and Director Reorientation 88
4.2.3 Rheological Measurements 89
4.3 Results 90
4.3.1 Molecular Flexibility Inferred from Intrinsic Viscosity 90
4.3.2 Effect of Chain Length on Rotational Viscosity 91
4.3.3 Effect of Chain Length on Shear Viscosity 93
4.4 Discussion 95
4.5 Conclusion 98
Bibliography 112

5 Flow Behavior of A Distinct Liquid Crystalline Phase 114
5.1 Introduction 114
5.2 Experimental 115
5.2.1 Materials 115
5.2.2 Powder X-ray Diffractometry 115
5.2.3 Rheology and Orientation Measurements 115
5.3 Phase Behavior 116
5.3.1 Subtle Structure of Phase X from Powder X-ray Diffraction 116
5.3.2 Rheological Signatures of Phase X 117
5.4 Shear Rheology and Orientation 119
5.4.1 Flow Curve 119
5.4.2 Observation of Parallel and Perpendicular Orientations 120
5.4.3 Orientation Flipping by Steady Shear 122

5.5 Oscillatory Shear Alignment 123
5.5.1 Selection of Alignment Trajectory by Varying Frequency 124
5.5.2 Role of Oscillatory Strain in Alignment Process 124
5.5.3 Orientation Flipping by Oscillatory Shear 125
5.6 Effect of Orientation on Linear Viscoelasticity 126
5.7 Discussion 127
5.7.1 Elusive Nature of Phase X 127
5.7.2 A Working Hypothesis for Orientational Flipping 129
5.8 Conclusion 131
Bibliography 150

6 Concluding Remarks **152**

List of Figures

1.1 Axial modulus as a function of the orientation parameter S for a thermotropic copolyester 2
1.2 Examples of small molecule liquid crystals 3
1.3 Molecular arrangements in nematic and smectic liquid crystalline phases. . 3
1.4 Schematic illustrations for the molecular architecture of liquid crystalline polymers 4
1.5 Chemical structures of several typical lyotropic and thermotropic LCPs. . . 5
1.6 The geometry of three possible types of elastic distortion. 7
1.7 Schematic representation of the disclination structures with different values of strength s 8
1.8 Schematic illustration of director tumbling and flow-aligning for nematics . 11
1.9 Schematic distinction between the director orientation and molecular orientation 14

2.1 Representative conoscopic interference figures in a plannar nematic monodomain 34
2.2 Director rotation θ as a function of applied strain at 130°C in DHMS-7,9 momodomain 35
2.3 Director rotation θ as a function of applied strain upon stepwise imposition of strain 36
2.4 Transient director rotation as a function of applied strain during flow startup 37
2.5 Tumbling parameter λ as a function of reduced temperature (T/T_{ni}) 38
2.6 Temperaure variation of optical anisotropy 39
2.7 Evolution of the director orientation as a function of time during relaxation 40
2.8 The transient director response of a planar DHMS-7,9 monodomain when the flow is applied orthogonal to initial director orientation 41
2.9 Tumbling parameter as a function of order parameter (S) for DHMS-7,9 and comparisons with predictions from molecular models 42

2.10 Schematic illustration for the effect of molecular flexibility on the aligning properies of main chain LCP 43

3.1 DSC scan of DHMS-7,9 65
3.2 Illustration of molecular orientation distribution $\Psi(\mathbf{u})$ at the local molecular level and director orientation distribution at the macroscopic level 66
3.3 Linear viscoelastic spectrum of DHMS-7,9 in the isotropic and nematic phases 67
3.4 Flow curves of DHMS-7,9 in the nematic phase 68
3.5 Representative X-ray scattering patterns of DHMS-7,9 69
3.6 Steady shear-induced orientation in the nematic phase as a function of shear rate and temperature 70
3.7 Evolution of the orientation parameter during relaxation upon shear cessation 71
3.8 Evolution of the dynamic modulus G^* during relaxation upon shear cessation 72
3.9 Optical micrographs of texture relaxation after steady shear in the nematic phase 73
3.10 Stress and orientation response during flow inception in the nematic phase . 74
3.11 Temperature effect on the evolution of shear stress and orientation parameter during flow inception 75
3.12 Transient stress response of 28K DHMS-7,9 following step changes of shear rate in the nematic phase 76
3.13 Evolution of the stress and orientation parameter after flow reversal in the nematic phase 77
3.14 Evolution of the stress and orientation parameter during interrupted shear flow reversal in the nematic phase 78
3.15 Evolution of complex shear viscosity as a function of time during oscillatory shear alignment in the nematic phase 79
3.16 Evolution of the anisotropic factor as a function of time during oscillatory shear alignment 80
3.17 Predictions of the Ericksen polydomain model for the evolution of anisotropy in the 1-3 plane 81
3.18 The shear stress predictions of the Ericksen polydomain model during flow inception 82

4.1 Intrinsic viscosity of DHMS-7,9 as a function of molecular weight M_w . . . 101
4.2 A re-plot of intrinsic viscosity following Bohadanecky's treatment 102
4.3 Determination of the rotational viscosity from the kinetics of director reorientation in the magnetic field 103
4.4 Molecular weight dependence of the rotational viscosity γ_1 104
4.5 The steady shear viscosity as a function of shear rate for different molecular weight samples 105
4.6 The complex viscosity as a function of oscillatory frequency for different molecular weight samples 106
4.7 The flow activation energy of DHMS-7,9 in the nematic phase 107
4.8 The shear viscosity of the nematic phase as a function of molecular weight . 108
4.9 Viscosity ratio, γ_1/η, as a function of molecular weight 109
4.10 SEC chromatograms of DHMS-7.6K with signals from the light scattering detector and the refractive index detector 110
4.11 Debye plot of one data slice from the SEC chromatogram of DHMS-28K sample. 111

5.1 High resolution powder X-ray diffraction of 28K DHMS-7,9 132
5.2 Apparent shear viscosity η and $|\eta^*|$ as a function of temperature 134
5.3 Storage modulus as a function of frequency in Phase X 135
5.4 Cole-Cole plots of 28K DHMS-7,9 136
5.5 Steady shear viscosity and first normal stress difference as a function of shear rate in Phase X of 28K DHMS-7,9 137
5.6 2-D orientation parameter and apparent shear viscosity as a function of temperature 138
5.7 Orientation parameter as a function of shear rate at different temperature in Phase X 139
5.8 Effect of thermal history on the stability of perpendicular alignment in Phase X of 28K DHMS-7,9 140
5.9 Mapping diagram of molecular orientation in temperature-shear rate space . 141
5.10 Orientational flipping by step change of shear rate or temperature 142

5.11 Evolution of shear stress as a function of strain in response to orientation flipping 143
5.12 Evolution of anisotropic factor and complex viscosity during large amplitude oscillatory shear alignment 144
5.13 Effect of oscillatory strain amplitude on the development of perpendicular alignment in the x-phase 145
5.14 Evolution of anisotropic factor after a temperature jump from 140°C to 110°C in the middle of continuous oscillation 146
5.15 Evolution of anisotropic factor as a function of time after switching shear mode from steady shear to oscillatory shear 147
5.16 Effect of orientation on linear viscoelasticity behavior 148
5.17 Schematic illustration of a tentative mechanism to explain the observed viscoelastic behavior for unaligned, parallel and perpendicular orientation states 149

List of Tables

4.1 Materials and phase characterization of DHMS-7,9 with different molecular weights 100

Chapter 1 Background

1.1 Introduction

The unique feature of liquid crystalline polymers (LCPs)—high local orientational order, which is retained in the solid state—has significant implications for commercial applications that utilize the mechanical properties of polymers [1], particularly in situations where weight savings are critical. This has been primarily driven by the discovery that fibers spun from liquid crystalline polymer solutions have remarkable mechanical strength. Melt processable LCPs have additional advantages, for example, enabling fabrication of intricate high strength parts by injection molding. They are attractive candidates in the packaging of electronic components because of their excellent strength, high temperature stability and low thermal expansion. LCPs also have distinctive processing advantages over conventional thermoplastics, which suffer tradeoffs between ease of processing and service performance. Processing of LCPs is facilitated by the flow-induced molecular alignment and the resulting low viscosity. The same flow-induced molecular alignment leads directly to the enhancement of mechanical strength (Figure 1.1). Thus, it is of great importance to understand how molecular orientation develops and evolves during processing flows.

Despite the fact that melt processable LCPs are amenable to a wide range of fabrication methods, relatively little progress has been made in understanding their flow behavior. This situation reflects the formidable experimental difficulties (i.e., thermal stability, turbidity, etc.) associated with structural and rheological studies of commercial LCP melts. The lack of structural data has particularly hampered progress in theoretical modeling of thermotropic LCP dynamics, which can eventually lead to rational design and control of materials processing. The goal of this work is therefore to use a combination of model materials and techniques to overcome many of the previously encountered experimental difficulties inherent to LCP melts, so that we can obtain comprehensive rheological and structural measurements. These results are understood in the framework of current theoretical models in order to identify some fundamental features intrinsic to LCP melts. The

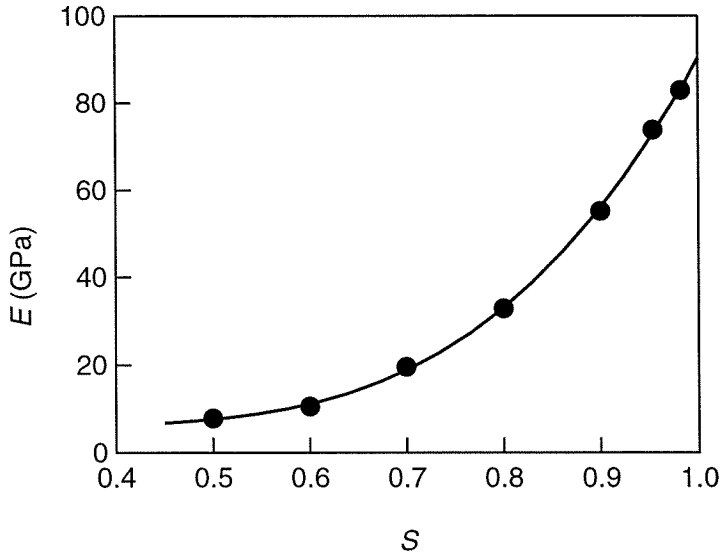

Figure 1.1: Axial modulus as a function of the orientation parameter, S, for a series of fibre samples drawn from a commercial thermotropic copolyester. (Adapted from Donald and Windle, *Liquid Crystalline Polymers*, © 1992 by Cambridge University Press.)

focus of this work has been on semiflexible LCP melts, leading to new insights into the role of molecular flexibility in LCP dynamics.

We begin this chapter with a brief introduction to the important structural features of liquid crystalline polymers, followed by a comparison between the rheological characteristics of LCP solutions and melts. We then give a brief review of current theoretical models that seek to describe the rheological behavior of liquid crystalline polymers, with an emphasis on those models that account for chain flexibility. Finally, we lay out the main objectives of this thesis.

1.2 Structure of LCPs from Å to μm

1.2.1 Liquid Crystalline Phases

Liquid crystalline order is intermediate between that of crystalline solids and isotropic liquids. At rest, liquid crystals possess at least some long range *orientational order*, but lack the full three-dimensional *positional order* of crystalline solids. They can generally flow like liquid; however, other anisotropic physical properties such as birefringence are reminiscent of the crystalline phase. This combination explains the name liquid crystal, which is in fact a contradiction in terms.

Molecules that form liquid crystalline phases are either oblate or prolate in shape, with aspect ratios of three or more. The strong anisotropy at the molecular level frustrates the ability of these molecules to adopt random orientations in the liquid state due to strong excluded volume interactions. Two examples of liquid crystals are shown in Figure 1.2, one with rod-like geometry and the other having disc-like shape.

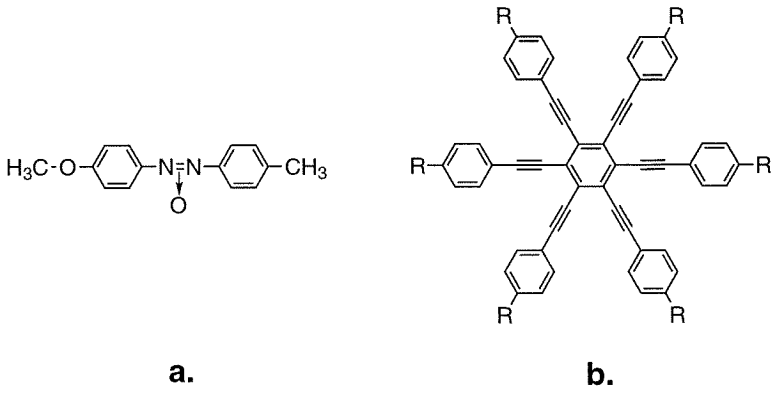

Figure 1.2: Examples of (a) rod-like and (b) disc-like molecules that can form liquid crystalline phase.

Nematic and *smectic* phases are two of the most common liquid crystalline phases for elongated molecules. Nematics possess orientational, but no positional order (Figure 1.3). The direction of preferred orientation is called the *director*, denoted by a unit vector **n**. Smectics are characterized in addition by positional order in at least one dimension (Figure 1.3). Many types of smectic phases are possible depending on the detailed molecular arrangements.

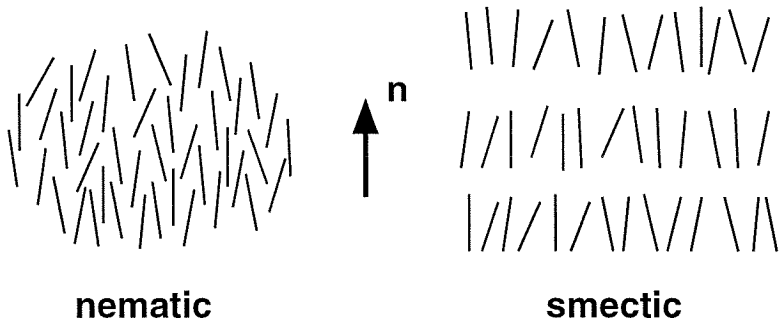

Figure 1.3: Molecular arrangements in nematic and smectic liquid crystalline phases.

Single component systems that show liquid crystalline phases in a definite temperature range are called *thermotropic*. On heating, thermotropic liquid crystals typically pass from the crystalline state, possibly through one or more smectic states, then a nematic state, and

finally to an isotropic state. Liquid crystalline behavior can also be induced by a change in concentration in solutions of anisotropic molecules or anisotropic assemblies of many molecules (micelles). These systems are called *lyotropic* liquid crystals.

1.2.2 Molecular Architecture of LCPs

Like the case of small molecules, liquid crystalline polymers can also be divided into two classes: lyotropic and thermotropic. Molecules that can form lyotropic nematic phase are usually in the form of rigid rods through the direct linkage of phenyl groups, whereas polymers capable of producing liquid crystalline melts are either semirigid, or contain rigid units, called *mesogens* (Figure 1.4a). Mesogens contain similar structural features (i.e., rigid

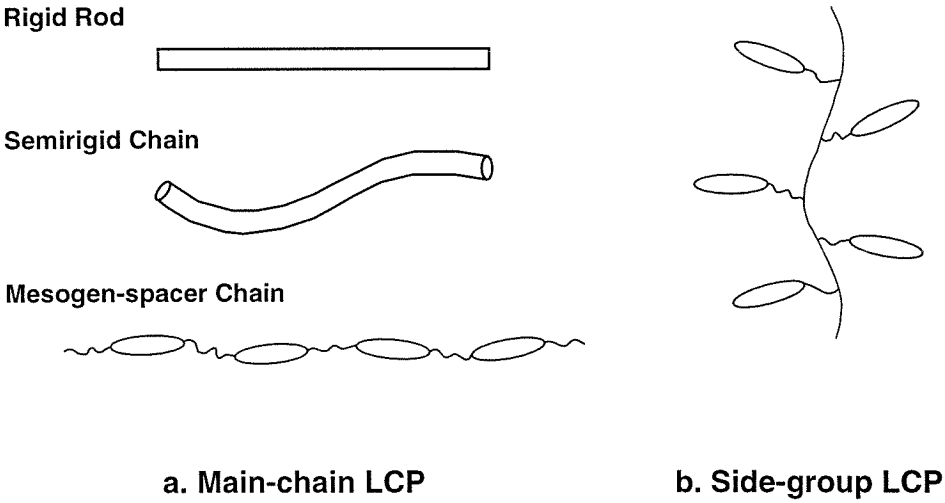

Figure 1.4: Schematic illustrations for the molecular architecture of liquid crystalline polymers: (a) main-chain LCP and (b) side-group LCP. Small ellipsoid and short curly line in the mesogen-spacer chain and side-group LCP represent mesogen and flexible spacer, respectively.

biphenyl or terphenyl groups) to small molecule liquid crystals. By varying the position of mesogen on the polymer chain, two different types of liquid crystalline polymers are possible, namely *main-chain* LCPs and *side-group* LCPs. In main-chain LCPs, mesogens are either directly connected or separated by some flexible spacers (e.g., -$(CH_2)_n$-) to form the polymer backbone (Figure 1.4a), whereas in side-group LCPs the mesogens are attached to the side of the chain via flexible spacers (Figure 1.4b). The focus of this thesis is on main-chain thermotropic LCPs with alternating mesogen and spacer structure.

Main-chain liquid crystalline polymers based on the simple addition of rigid monomer units (e.g., Figure 1.5 a&b) tend to be intractable during thermal processing. The prob-

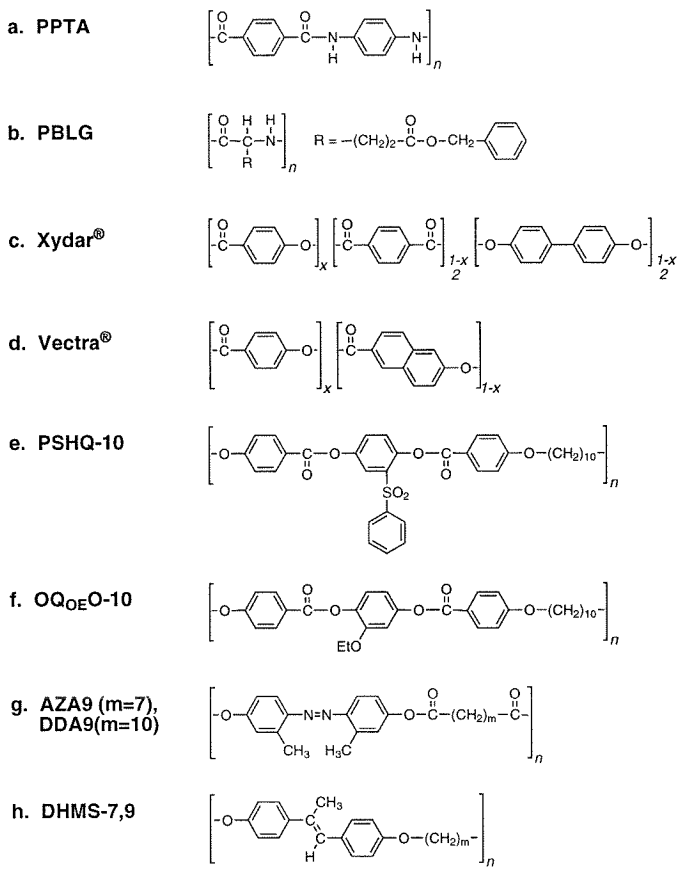

Figure 1.5: Chemical structures of several typical lyotropic and thermotropic LCPs. The top two (a and b) structures are usually used as lyotropic polymers, and the bottom six (c to h) structures are thermotropes. Vectra and Xydar polymers are commercially trademarked thermotropic LCPs by Hoechst and BP Amoco, respectively. PSHQ-10, $OQ_{OE}O$-10, AZA9, DDA9 and DHMS-7,9 are several mesogen-spacer type thermotropes with accessible isotropization point reported in the literature, among which DHMS-7,9 is the model material used in this study.

lem is that they are highly crystalline and on heating they decompose before they finally melt. Reducing the melting temperature is one of the primary objectives in molecular design of thermotropic LCPs. Most commercial thermotropes have two or more monomer units randomly distributed along the polymer chain to suppress their melting point into a useful working range without destroying the mesophase stability. Amoco's Xydar and Hoechst's Vectra polymers (Figure 1.5 c&d) are two examples of this strategy. Alternatively, introducing flexible aliphatic spacers between mesogenic units can effectively disrupt crystallinity. Although this type of main-chain LCPs is of limited commercial value, these

mesogen-spacer type LCPs provide valuable model systems for physical studies to clarify the processes that govern the flow behavior LCPs.

This has motivated development of model materials with accessible isotropic transitions ($T_{ni} < 250°C$), including a number of polyesters [2, 3, 4, 5, 6] (e.g., Figure 1.5 e-g) and a polyether [7] (Figure 1.5 h). We choose the latter type because of its greater thermal stability (no transesterification occurs at elevated temperatures). The thermotropic polyether based on a dihydroxymethylstilbene (DHMS) mesogen first synthesized by Percec and coworkers [7] has been proven to be a good model system for rheological characterization. In this study, we examine DHMS-7,9, in which DHMS is copolymerized randomly with 7- and 9-methylene spacer groups (Figure 1.5 h). As a model system, DHMS-7,9 offers an accessible isotropic state, a stable chemical structure, a modest melting point ($T_m \approx 90°C$) with a wide nematic range ($T_{ni} - T_{xn} \approx 80°C$), and good optical transparency. In addition, DHMS-7,9 is soluble in common solvents (e.g., CH_2Cl_2 and THF), enabling us to determine its absolute molecular weight using multi-angle light scattering. The ability to characterize molecular characteristics of DHMS-7,9, such as molecular weight, enables a molecular understanding of its flow behavior.

1.2.3 Orientation at Continuum Level

The orientation of the director at bounding surfaces often differs from that in the bulk state, leading to spatial variations in the director field. The spatial inhomogeneity of director orientation disrupts the molecular packing and thus incurs a free energy penalty, the minimization of which determines the equilibrium state of the director field $\mathbf{n}(\vec{r})$. If the length scale over which director orientation change is large compared to molecular length, the continuum expression of free energy density W_d constructed by F.C. Frank is appropriate [8],

$$2W_d = K_1(\nabla \cdot \mathbf{n})^2 + K_2(\mathbf{n} \cdot \nabla \times \mathbf{n})^2 + K_3(\mathbf{n} \times \nabla \times \mathbf{n})^2, \tag{1.1}$$

where $\nabla \cdot \mathbf{n}$ and $\nabla \times \mathbf{n}$ are the divergence and the curl of $\mathbf{n}$. The three terms represent independent contributions from three possible types of distortions in the director field, commonly referred to as *splay*, *twist* and *bend* respectively (Figure 1.6). The K_is are called Frank elastic constants, and their values are usually on the order of 10^{-7} dyne for small

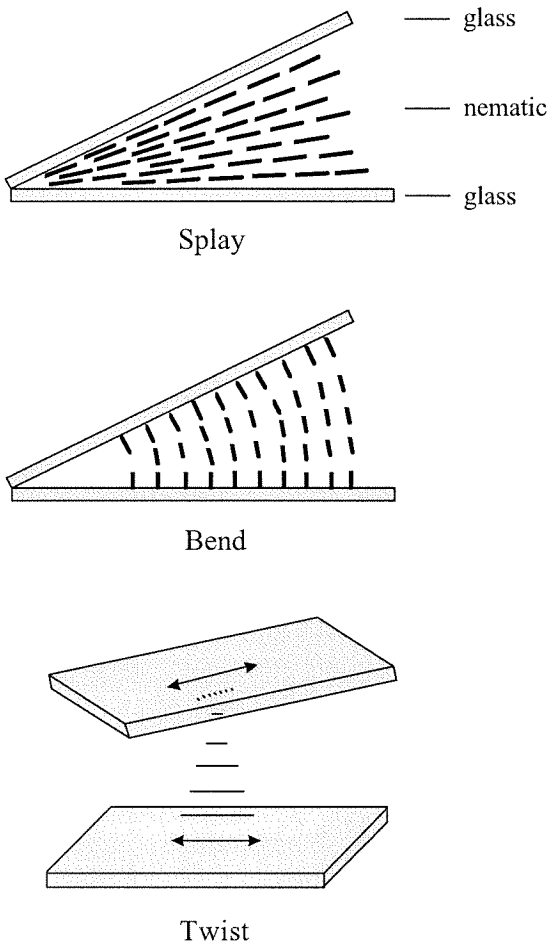

Figure 1.6: The geometry of three possible types of elastic distortion: splay, bend, and twist in nematic liquid crystals. (Adapted from de Gennes and Prost, *The Physics of Liquid Crystals*, 1993, Oxford University Press, Inc.)

molecule LCs. In main-chain LCPs, K_1 and K_3 are greatly increased relative to small molecule LCs, while K_2 remains similar in magnitude to small molecule LCs [9].

1.2.4 Defects and Polydomain Textures

Though the director varies smoothly and continuously on large length scale, singularities may occur in the director field $\mathbf{n}(\vec{r})$ where the director abruptly changes orientation. These singularities are known as *disclinations*, which can be in the form of either *point* or *line* defects. By analogy to a crystal where a dislocation is regarded as a discontinuity in positional translation, in a liquid crystal a disclination is a discontinuity in orientation. Disclinations are characterized by their strength, s, which is the number of counter-clockwise

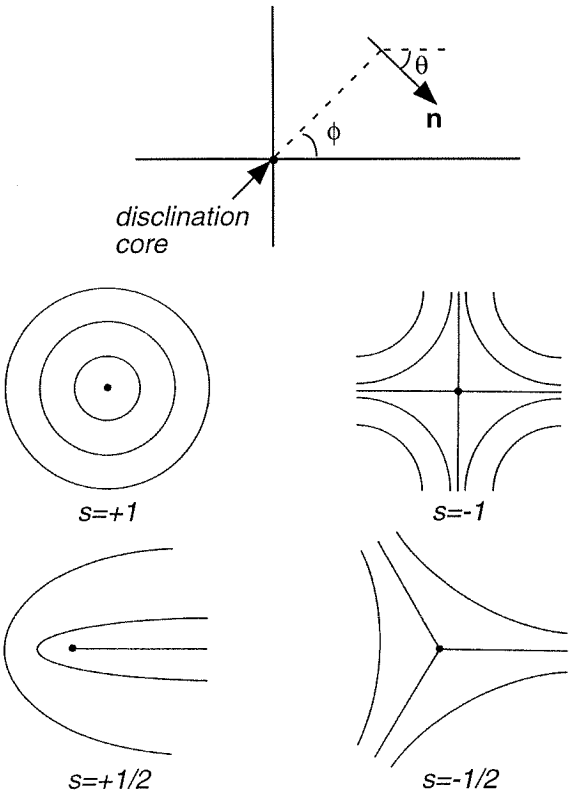

Figure 1.7: Schematic representation of the molecular orientation field near disclinations with different strength s. The director field $\mathbf{n}$ around a disclination core can be defined by two parameters θ and ϕ, illustrated in the above polar coordinates.

rotations that the director suffers as one moves in a closed-loop in the counter-clockwise direction around the disclination core (Figure 1.7). Individual disclinations in nematic liquid crystals often exhibit characteristic dark "brushes" (two or four extinction lines) between crossed polarizers, known as *Schlieren* textures. These are disclinations of line singularities with strength $|s| = \frac{1}{2}$ or $|s| = 1$.

Disclinations disrupt molecular orientation field, and a high density of these orientational defects in LCPs leads to a *polydomain* morphology in which the director maintains orientational correlation only in localized regions, usually on the length scale of microns. These localized regions are often referred to as *domains* [10]. The polydomain morphology is highly textured and clearly visible under the polarizing microscope. The polydomain texture has important consequence on the structure and rheology of liquid crystalline polymers, since rheological and structural data obtained generally reflect a macroscopic average over the polydomain structure, unless monodomain samples are specially prepared.

1.3 Flow Behavior of LCPs

The flow properties of nematic LCPs are often very complicated due to a complex interplay between their molecular anisotropy and the applied flow field. Several distinct levels of structure require consideration. At the most basic level, it is important to understand how a director field $\mathbf{n}(\vec{r})$ interacts with an applied flow field. This question may be addressed through the linear continuum theory of of Leslie and Ericksen (Section 1.3.1), which assumes that flow is not strong enough to perturb the local molecular orientation order of liquid crystal, but merely alters its direction of orientation. The Leslie-Ericksen theory is originally developed for small molecule nematics, and should also be valid for polymeric nematics at shear rate slow relative to their molecular relaxation process.

The second structural level of importance is the change in local molecular orientation distribution during flow at high shear rate. This gives rise to nonlinear viscoelastic effects. The appropriate structural variable to account for the effect of flow on molecular configurations is the orientation distribution function $\Psi(\mathbf{u})$ that characterizes the orientation of the entire collection of molecules in the system, where $\mathbf{u}$ represents orientation of each individual molecule. Extensive modeling efforts have been made to derive $\Psi(\mathbf{u})$ and may be found in an excellent review article [11]. Our intent here is to review some general aspects of LCPs rheological observations and to help identify some key differences between lyotropes and thermotropes (Section 1.3.2).

The third structural level needs to account for the evolution of the polydomain structure during flow. A complete description of LCP dynamics needs to incorporate both local and mesoscopic orientation, i.e., the distribution of *molecular orientation* $\Psi(\mathbf{u})$ with respect to the director, and a distribution of *director orientations* $\Psi(\mathbf{n})$ with respect to an arbitrary direction in a laboratory reference frame (e.g., the flow direction). To date, there has only been limited progress on theoretical modeling of polydomain rheology because of little information available for defect structure and dynamics of LCPs.

1.3.1 Director Tumbling and Flow-Aligning

According to the continuum formulation of Leslie-Ericksen theory [12, 13], the viscous response of nematics to deformation is determined by the six Leslie coefficients, $\alpha_1 - \alpha_6$. Of these, α_2 and α_3 play a particularly important role in determining the qualitative orientation

behavior in shear. The evolution of director orientation during flow can be described by:

$$\frac{\partial \mathbf{n}}{\partial t} = \mathbf{n} \cdot \boldsymbol{\omega} + \lambda(\mathbf{n} \cdot \mathbf{D} - \mathbf{nnn} : \mathbf{D}), \tag{1.2}$$

where $\boldsymbol{\omega} = \frac{1}{2}\left(\nabla \mathbf{v} - \nabla \mathbf{v}^T\right)$ is the vorticity tensor, $\mathbf{D} = \frac{1}{2}\left(\nabla \mathbf{v} + \nabla \mathbf{v}^T\right)$ is the rate of strain tensor, and $\lambda = (\alpha_2 + \alpha_3)/(\alpha_2 - \alpha_3)$ is commonly known as tumbling parameter. The rate change of the director orientation (left side of Eq. 1.2) has two contributions: one is the rotation of the surrounding fluid and the other is the change of orientation due to straining effect (right side of Eq. 1.2).

The flow behavior of the director described by Eq. 1.2 depends on the specific liquid crystal only through the critical parameter λ. This equation is very similar to the dynamics of rigid ellipsoids suspension [14]. In the case of $|\lambda| < 1$, which is always true for ellipsoidal particles, the rotational component of the flow prevails, and the particle tends to precess indefinitely in the shear plane (flow-gradient plane) following a periodic orbit known as its *Jeffrey orbit* [15]. Similar in liquid crystals with $|\lambda| < 1$, the hydrodynamic torques act to rotate the director during shear. The continuous rotation of the director in the shear plane is referred to as *director tumbling* (Figure 1.8a).

In contrast, liquid crystals with $|\lambda| > 1$ exhibit a very different director response, since the straining effect dominates over vorticity rotation. The director does not tumble in steady shear, but tends to stabilize at a fixed angle, θ_L, with respect to the flow direction (see Figure 1.8b), given by

$$\tan\theta_L = \sqrt{\frac{\lambda - 1}{\lambda + 1}} \equiv \sqrt{\frac{\alpha_3}{\alpha_2}}, \tag{1.3}$$

where θ_L is called Leslie alignment angle. This type of behavior is referred to as *flow-aligning*. It is known that most small molecule nematics are flow-aligning, and their flow behavior is relatively simple due to the fact that all the molecules tend to orient at the Leslie alignment angle.

The flow properties of tumbling nematics are much more complicated than those of flow-aligning nematics. The rotation of the director in the shear flow could continue through multiple periods of π until distortional elasticity becomes large enough to counteract the hydrodynamic torques and eventually arrest the tumbling motion. An immediate rheological consequence of director tumbling is a series of stress oscillations in start-up of shearing flow,

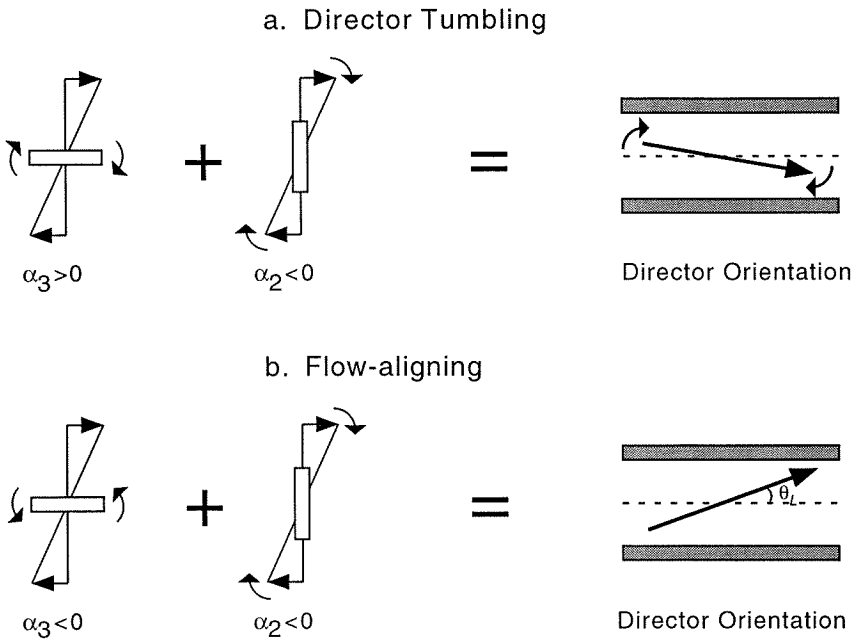

Figure 1.8: Schematic illustration of (a) director tumbling and (b) flow-aligning for nematic liquid crystals. The Leslie-Ericksen viscosities α_2 and α_3 determine the direction and rate of rotation of the director (represented by the rectangles). When α_2 (usually negative for rod-like nematics) and α_3 are of different signs, the two hydrodynamic torques act to continuously rotate the director in the shear plane, leading to director tumbling. When α_2 and α_3 are both negative, two hydrodynamic torques are balanced at the Leslie alignment angle θ_L, giving rise to flow-alignment.

observed for both small molecule LCs [16] and lyotropic LCPs [17]. In addition, shear flow of tumbling nematics is highly susceptible to flow instabilities, leading to complex fluid textures [18, 19].

Despite the extreme qualitative differences between flow aligning and director tumbling, quantitative determination of the tumbling parameter λ for polymeric nematics has progressed very slowly. The high viscosity of liquid crystalline polymers impedes preparation of the defect-free monodomain samples that are required for most techniques to measure the fundamental viscoelastic properties of nematics. Nevertheless, it has been directly confirmed that lyotropic LCPs are of tumbling type [20, 21], in agreement with predictions of molecular theory [22]. For thermotropic LCPs, however, similar advances are lacking, and it is largely unknown whether they are flow aligning or tumbling. Since flow behavior of LCPs is strongly dependent on whether λ is above or below unity [23], which also has profound consequences on their average molecular orientation state under shear flow [10], one of the

central goals of this thesis is to provide comprehensive, quantitative characterization of the shear aligning properties of a thermotropic LCP.

1.3.2 Rheology of Thermotropic LCPs vs. Lyotropic LCPs

Along with the unknown nature of flow-aligning vs. tumbling character for thermotropic LCPs, relatively little progress has been made in understanding their rheological behavior. Existing experimental data for thermotropes are scattered and sometimes contradictory, largely due to difficulties associated with the materials themselves (Section 1.2.2).

As a point of departure for examining the flow behavior of thermotropes, it is useful to recall some general features of lyotropic LCP rheology. Among the unusual rheological phenomena observed in lyotropic systems are the so called three-region flow curve [24], negative values of steady state first normal stress difference (N_1) [25, 26, 27, 28], and multiple oscillations in transient stress response upon flow start up or stepwise change of shear rate [29, 30]. A three-region flow curve, which consists of shear thinning at low and high shear rates (Region I, III) and pseudo-Newtonian (Region II) at intermediate rates, is believed to originate from the polydomain nature of liquid crystalline polymers. The occurrence of negative steady state N_1 and multiple stress oscillations during transient flows, however, is directly attributed to the tumbling nature of rod-like lyotropic LCPs. The negative values of N_1 are usually located at shear rates close to the onset of Region III, where the orientation distribution function $\Psi(\mathbf{u})$ departs considerably from its equilibrium shape, and the departure is in the direction of a *reduced* molecular anisotropy. Since the nematic potential has the tendency to drive molecules back into a more anisotropic equilibrium state, the reduction in molecular anisotropy is unfavorable, leading to the occurrence of negative N_1.

In contrast to lyotropic LCPs, many of the unusual rheological features described above have not been observed in thermotropes. In relation to the variation of viscosity with shear rate, observed behavior includes completely shear thinning, shear thickening and three-region flow curves [31, 32]. Negative steady state values of N_1 have been reported for some thermotropic LCPs [33, 34], but unlike the case of lyotropic LCPs, none of these has shown double sign changes (positive $\rightarrow$ negative $\rightarrow$ positive) with increasing shear rate. In fact, it now appears more likely that all the reported negative values of the steady state N_1 in thermotropes are due to experimental artifacts [35]. The multiple oscillations of transient

shear stress, characteristic of lyotropic LCPs upon step change of shear rate, have not been observed in thermotropes at all.

The implication of these rheological disparities between thermotropes and lyotropes should not be overlooked. In particular, the absence of negative steady state N_1 and multiple stress oscillations during transient flow may imply thermotropic LCPs are flow-aligning type. This raises an interesting question regarding the effect of chain flexibility on the dynamical behavior of LCP, since the major molecular difference from lyotropic LCPs is increased molecular flexibility for thermotropes. Recent theoretical models have indeed predicted that semiflexible nematic chains tend to be flow-aligning with increasing chain flexibility [36, 37, 38]. To obtain physical insights into the aligning properties of LCPs, we briefly review molecular models that account for the effect of chain flexibility on the aligning dynamics of LCPs in the following section.

1.4 Role of Chain Flexibility in LCP Dynamics

The prevailing Doi model for rigid rods has achieved remarkable success in describing the rheology of lyotropic LCPs. However, LCPs may possess some internal degrees of freedom and thus deviate considerably from the ideal situation of rigid rods. This is often the case for thermotropic materials, in which chain flexibility is deliberately introduced to suppress their melting points. Since semiflexible thermotropes are the main subject of this thesis, it is instructive to seek out theoretical treatments which incorporate some degree of molecular flexibility in order to determine what effect, if any, it will have on the structure and rheology of thermotropic LCPs.

In this section, we will briefly outline the predictions of the Doi model [39] and its extension to semiflexible chains [36] and slightly flexible rods [41], followed by discussions of two other molecular models, the nematic dumbbell model [37] and nematic Rouse model [38]. The focus of this section will be on theoretical predictions of LCP aligning properties, and how tumbling parameter varies as a function of chain flexibility. A crossover transition from rigid to semiflexible conformation may occur with increasing chain flexibility, and implications of such a transition for rheological behavior of LCPs will also be presented.

1.4.1 The Doi Model of Rod-like LCPs

Instead of using variables on the continuum level, such as the director $\mathbf{n}$, to describe the dynamical behavior of LCPs, the Doi model express macroscopic observable quantities (e.g., stresses, degree of orientation, etc.) in terms of the molecular orientation distribution function $\Psi(\mathbf{u})$. Here we must be cautious not to confuse the *individual* molecular orientation $\mathbf{u}$ with the continuum description of the director orientation $\mathbf{n}$ (Figure 1.9). The second

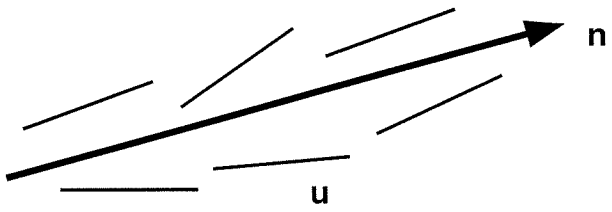

Figure 1.9: Schematic distinction between the director orientation $\mathbf{n}$ and the orientation of each individual molecule $\mathbf{u}$.

moment of $\Psi(\mathbf{u})$ is related to the order parameter tensor $\mathbf{S}$, defined as:

$$\mathbf{S} = \langle \mathbf{uu} \rangle - \frac{1}{3}\boldsymbol{\delta}, \tag{1.4}$$

where $\langle \cdots \rangle$ denotes an ensemble average over all molecules, and $\boldsymbol{\delta}$ is the unit tensor. In an equilibrium nematic phase, the molecular distribution is uniaxial about the director $\mathbf{n}$, and the order parameter tensor $\mathbf{S}$ is directly related to $\mathbf{n}$ by

$$\mathbf{S} = S(\mathbf{nn} - \frac{1}{3}\boldsymbol{\delta}), \tag{1.5}$$

where S is the scalar order parameter that can be experimentally determined.

The essence of the Doi model is to solve the Smoluchowski equation for the orientation distribution function $\Psi(\mathbf{u})$, or equivalently, a set of constitutive equations built on the order parameter tensor $\mathbf{S}$ [39]. A closed-form solution of the Doi model is generally very difficult to obtain, and requires a closure approximation for the fourth moment tensor $\langle \mathbf{uuuu} \rangle$. Care must be taken about which type of closure approximation should be used since an incorrect choice, for example, pre-averaging approximation (i.e., $\langle \mathbf{uuuu} \rangle = \langle \mathbf{uu} \rangle \langle \mathbf{uu} \rangle$), can lead to erroneous predictions even regarding the qualitative distinction between flow aligning vs. director tumbling [40]. One of the most important predictions from the Doi model is that rod-like lyotropic LCPs are exclusively of the tumbling type [22]. This prediction marked

an initial success of the Doi model when tumbling was directly observed in lyotropic LCP solutions [20, 21].

The major limitation of the Doi model is its inability to account for the effect of chain flexibility on aligning properties of LCPs. Although a general formulation to predict the tumbling parameter λ is yet to be developed, a couple of limits have been examined. For a highly flexible main-chain LCP (the limit of infinite ratio of chain length L to persistence length q, $L/q \to \infty$), Semenov found λ is always above unity [36]; therefore, flexible polymeric nematics are predicted to be flow aligning for all values of the order parameter. In contrast, for slightly flexible rods ($0 < L/q \ll 1$), Subbotin found that λ is less than predicted for perfectly rigid rods except at high order parameter [41]. Thus, for moderate S, an increase in chain flexibility at first produces a decrease in λ (greater tumbling), but eventually λ rises above unity (flow aligning) when chain becomes sufficiently flexible.

1.4.2 Incorporating Chain Flexibility in Molecular Models

Aside from evaluating the effect of flexibility for the limiting cases of the Doi model, two alternative formalisms have been developed to incorporate molecular flexibility into the description of LCP dynamics, the *nematic dumbbell model* [37] and the *nematic Rouse model* [38]. These two models are essentially an anisotropic generalization of ordinary dumbbell model and Rouse model, respectively, which consider nematic chains as consisting of a series of nematogens separated by elastic springs.

An important prediction of the nematic dumbbell model is that flow alignment occurs at all values of the order parameter S, and the tumbling parameter λ decreases with increasing S, but remains above unity (flow aligning) for $S < 1$:

$$\lambda = \frac{2+S}{3S}. \tag{1.6}$$

Thus, the flexibility of a chain as a whole prevails in dictating the flow-aligning behavior although the constituent rigid "building block" would generate a tumbling nematic.

The nematic Rouse model has considered the effect of hairpins on the shear aligning properties of LCPs. Here, a hairpin represents an abrupt U-turn of mesogen orientation along the chain contour. Two limiting cases of chain character have been evaluated, a *direct chain* (DC) without hairpin and an *anisotropic Gaussian chain* (AGC) with a large number

of hairpins. The nematic Rouse model predicts that DCs maintain tumbling character with the director orientation strongly coupled to the Rouse relaxation of the chain conformation, while AGCs (in the viscous limit) are flow aligning with identical predictions for all the Leslie-Ericksen viscosity coefficients to those of the nematic dumbbell model. Thus, long flexible nematic chains are predicted to be exclusively flow-aligning from both models.

1.4.3 Crossover from Rod-like to Semiflexible Behavior

Typical nematic LCPs neither adhere to the description of rigid rods nor to that of infinitely flexible chains. With increasing chain length, LCPs may go from very rigid to semirigid (i.e., undulated rod with no hairpin), and to semiflexible (with hairpins). For rod-like LCP, such as polybenzyl-γ-glutamate (Figure 1.5b), a crossover transition to semirigid behavior occurs at a characteristic length-to-diameter ratio (L/d) around 55 [42]. In contrast, LCPs with alternating mesogen and spacer structure may not behave like rigid rods even at short chain length due to the internal molecular flexibility provided by alkyl spacers. Indeed, the flexibility of a mesogen-spacer type LCP can be very high, resulting in several hairpins along a given chain [43]. The nematic chain with many hairpins falls within semiflexible regime.

The dynamics of polymeric nematics depends strongly on the chain flexibility. In the limiting case of rigid rods, the Doi model predicts that the viscosity has a highly non-linear molecular weight dependence (M^6) [39]; in the semirigid regime, the viscosity is predicted to depend quadratically on the molecular weight [44]; and in the semiflexible regime, the viscosity is predicted to have a linear dependence on molecular weight [44]. The trend of less sensitivity to molecular weight with increasing chain length also applies to the Frank elastic constants, for example, the bending elastic constant K_3 of lyotropic PBG (Figure 1.5b) is found to first increase with molecular weight and then saturate after a critical molecular weight [42]. Thus, measurements of viscoelastic properties of LCPs provides an indirect way to evaluate the chain flexibility.

1.5 Objectives and Thesis Organization

Thermotropic LCPs have been synthesized in hopes of beginning a new era of light-weight and high-strength materials suitable for high use temperatures. The key to attaining high-

strength in LCPs centers on the understanding of structural and orientational behavior during processing flows. Unfortunately, development of a molecular theory that fully describes flow behavior of thermotropes has been slow to emerge due to the lack of direct structural measurements of thermotropic LCPs during flow. Our study is therefore aimed to address this need for structural data of thermotropic LCPs, with emphasis on how molecular orientation responds to the applied flow as probed by *in situ* optical and X-ray techniques.

The main theme of this study will be the issue of shear aligning properties for main-chain thermotropic LCPs. To date, only one qualitative observation has been reported [45], showing very intriguing temperature dependent aligning behavior—shear aligning at high temperature and tumbling at low temperature. Thus, it has yet to be conclusively demonstrated for thermotropic LCPs whether they are shear aligning or director tumbling (Chapter 2). In Chapter 3, we aim to develop understanding of how bulk mechanical properties correlate with orientation response during flow and how this depends on the shear aligning properties of thermotropic LCPs. The effect of molecular weight on the dynamical behavior of LCPs is addressed in Chapter 4. This comprehensive set of mechanical and *in situ* orientation measurements lead to new insight into the effect of molecular flexibility on the dynamics of liquid crystalline polymers.

We switch to a complete different topic in Chapter 5 and discuss an interesting (yet still unidentified) liquid crystalline phase. Rheology and shear orientation behavior of this mystery phase are dramatically different from those of the nematic phase. Most strikingly, shear flow induces a remarkable orientational flipping that is reminiscent of lamellar block copolymer.

The final chapter (Chapter 6) summarizes the main contribution of this work and its broad relevance to the field of LCP rheology, and possible areas for future study.

Bibliography

[1] NMAB Committee on Liquid Crystalline Polymers. *Liquid Crystalline Polymers.* National Academic Press, Washington D.C., 1990.

[2] R. W. Lenz. *Faraday Discuss. Chem. Soc.*, 79:21, 1985.

[3] A. Blumstein, O. Thomas, and S. Kumar. *J. Polym. Sci. Part B: Polym. Phys.*, 24:27, 1986.

[4] P. Esnault, F. Volino, A. F. Martins, S. Kumar, and A. Blumstein. *Mol. Cryst. Liq. Cryst.*, 153:143, 1987.

[5] P. Driscoll, T. Masuda, and K. Fujiwara. *Macromolecules*, 24:1567, 1991.

[6] S. S. Kim and C. D. Han. *Macromolecules*, 26:6633, 1993.

[7] V. Percec, H. Nava, and H. Jonsson. *J. Polym. Sci. Polym. Chem.*, 25:1943, 1987.

[8] F. C. Frank. *Disc. Faraday Soc.*, 25:19, 1958.

[9] S. Zheng-Min and M. Kleman. *Mol. Cryst. Liq. Cryst.*, 111:321, 1984.

[10] W. R. Burghardt. *Macromol. Chem. Phys.*, 199:471, 1998.

[11] G. Marrucci and F. Greco. *Adv. Chem. Phys.*, LXXXVI:331, 1993.

[12] F. M. Leslie. *Arch. Rat. Mech. Ana.*, 28:265, 1968.

[13] J. L. Ericksen. *Arch. Rat. Mech. Ana.*, 4:231, 1960.

[14] R. G. Larson. *Constitutive Equations for Polymer Melts and Solutions.* Butterworths, 1988.

[15] G. B. Jeffery. *Proc. Royal. Soc. Lond. A*, 102:161, 1922.

[16] D.-F. Gu, A. M. Jamieson, and S. Q. Wang. *J. Rheol.*, 37:985, 1993.

[17] P. Moldenaers and J. Mewis. *J. Non-Newt. Fluid Mech.*, 34:359, 1990.

[18] P. Pieranski and E. Guyon. *Phys. Rev. Letts.*, 32:924, 1974.

[19] P. E. Cladis and S. Torza. *Phys. Rev. Letts.*, 35:1283, 1975.

[20] W. R. Burghardt and G. G. Fuller. *Macromolecules*, 24:2546, 1991.

[21] M. Srinivasarao and G. C. Berry. *J. Rheol.*, 35:379, 1991.

[22] N. Kuzuu and M. Doi. *Jpn. J. Phys. Soc.*, 53:1031, 1984.

[23] R. G. Larson. *The Structure and Rheology of Complex Fluids.* Oxford University Press, Oxford, 1999.

[24] S. Onogi and T. Asada. In G. Astarita, G. Marrucci, and L. Nicolais, editors, *Rheology*, volume 1. Plenum Press, New York, 1980.

[25] G. Kiss and R. S. Porter. *J. Polym. Sci.: Polym. Symp.*, 65:193, 1978.

[26] P. Moldenaers and J. Mewis. *J. Rheol.*, 30:567, 1986.

[27] J. J. Magda, S. G. Baek, K. L. DeVries, and R. G. Larson. *Macromolecules*, 24:4460, 1991.

[28] S. G. Baek, J. J. Magda, and R. G. Larson. *J. Rheol.*, 37:1201, 1993.

[29] J. Mewis and P. Moldenaers. *Mol. Cryst. Liq. Cryst.*, 153:291, 1987.

[30] P. Moldenaers, M. Mortier, and J. Mewis. *Chem. Eng. Sci.*, 49:699, 1994.

[31] D. S. Kalika, David W. Giles, and M. M. Denn. *J. Rheol.*, 34:139, 1990.

[32] K. F. Wissbrun. *British Polymer Journal*, 12:163, 1980.

[33] A. D. Gotsis and D. G. Baird. *J. Rheol.*, 25:275, 1986.

[34] S. M. Guskey and H. H. Winter. *J. Rheol.*, 35:1191, 1991.

[35] C. D. Han and S. Chang. *J. Rheol*, 38:241, 1994.

[36] A. N. Semenov. *Sov. Phys. J. E. T. P.*, 66:712, 1987.

[37] P. L. Maffettone and G. Marrucci. *J. Rheol.*, 36:1547, 1992.

[38] D. Long and D. C. Morse. *Europhys. Letts*, 49:255, 2000.

[39] M Doi and S. F. Edwards. *The Theory of Polymer Dynamics*. Oxford University Press, New York, 1986.

[40] G. Marrucci. *Mol. Cryst. Liq. Cryst.*, 72:153, 1982.

[41] A. Subbotin. *Macromolecules*, 26:2562, 1993.

[42] S.-D. Lee and R. B. Meyer. *Phys. Rev. Letts.*, 61:2217, 1988.

[43] M. H. Li, A. Brulet, P. Davidson, P. Keller, and J. P. Cotton. *Phys. Rev. Letts.*, 70:2297, 1993.

[44] P. G. de Gennes. In A. Ciferri, W. R. Krigbaum, and R. B. Meyer, editors, *Polymer Liquid Crystal*, chapter 5. Academic Press, New York, 1982.

[45] M. Srinivasarao, R. O. Garay, H. H. Winter, and R. S. Stein. *Mol. Cryst. Liq. Cryst.*, 223:29, 1992.

Chapter 2 Quantitative Determination of Shear Aligning Properties

2.1 Introduction

The key to attaining high mechanical performance for liquid crystalline polymers (LCPs) centers on the understanding of structural and orientational behavior during processing flows. The qualitative orientation response in shear flow is strongly dependent on whether LCP is flow-aligning or director tumbling. Flow alignment occurs when two hydrodynamic torques on the director balance at a particular angle (the "Leslie angle") with respect to the flow direction, while director tumbling occurs when no such alignment angle exists and hydrodynamic torques act to rotate the director indefinitely in the shear plane (i.e., the flow-velocity gradient plane). Shear flow promotes macroscopic orientation of aligning nematics, while shear flow of tumbling nematics is highly susceptible to flow instabilies [1, 2], and generally leads to low macroscopic orientation and complex morphology.

Despite the extreme qualitative differences between flow aligning and director tumbling behavior, definitive classification of polymeric nematics is rare. This situation is mainly because the fundamental viscoelastic properties can only be obtained on defect-free monodomain samples, and for polymeric nematics, these are hard to prepare due to the high viscosity of liquid crystalline polymers. Nevertheless, the classification of flow-aligning vs. tumbling has been successfully carried out on two lyotropic solutions of rod-like polymers, both of which showed tumbling behavior [3, 4], in agreement with predictions of Doi model for rod-like LCPs [5]. This discovery has profoundly impacted our understanding of lyotropic LCP rheology. It is now firmly established that tumbling is directly responsible for many of the unusual rheological features (e.g., negative steady state values of first normal stress difference, N_1) and shear orientation behavior of lyotropic LCPs [6, 7].

Similar advances are lacking for thermotropes. The added molecular flexibility in most thermotropic LCPs may alter their shear aligning properties in a non-trivial manner. In contrast to the Doi model's prediction for tumbling, all molecular theories for semiflexible

polymeric nematics predict shear aligning behavior when chain gets sufficiently flexible [8, 9, 10]. In the limit of infinite ratio of chain length L to persistence length q, i.e., $L/q \rightarrow \infty$, Semenov found that polymeric nematics are exclusively flow aligning for all values of the order parameter [8]. Similar predictions have also been made by the nematic dumbbell model [9] and the nematic Rouse model [10]. Unfortunately, it is largely unknown whether thermotropes are flow aligning or tumbling. There is accumulated indirect evidence from mechanical and orientational studies suggesting that thermotropes with alternating mesogen and spacer structure may be flow aligning [11, 12, 13, 14]; however, only one direct observation has been reported on a mesogen-spacer type monodomain thermotrope ($OQ_{OE}O$-10) [15], showing a qualitative transition from shear aligning behavior at high temperature (close to its isotropization point, T_{ni}) to tumbling behavior as temperature approaches its nematic-to-smectic A transition (T_{nS_A}). The tumbling behavior near T_{nS_A} for $OQ_{OE}O$-10 is probably related to pre-transitional fluctuations of smectic phase and may not be general to other polymeric nematics.

Given the importance that qualitative nature of aligning properties dictates the flow behavior of LCPs, the ambiguous situation of thermotropes has to be conclusively resolved by more comprehensive optical studies on well-defined monodomain samples. Quantitative optical studies on monodomain will enable a direct comparison of structural data with predictions from theoretical models, yielding important physical insights into the effect of molecular flexibility on the dynamics of thermotropic LCP.

Recently, our group has made significant progress toward understanding of the flow behavior of main chain thermotropic LCP, observing indirect evidence that it is of the shear aligning type [14]. In this paper, we present direct, quantitative measurements of the director response in a monodomain to a variety of shear flows. *In situ* flow-conoscopy has been employed to monitor the director orientation during shear, similar to approaches used in the previous literature [3, 4, 15]. Quantitative determination of tumbling parameter λ as a function of molecular order parameter S for LCPs provides the first opportunity to compare with theoretical predictions of $\lambda(S)$ from available molecular models. The feed of λ value into modeling efforts enables us to directly predict rheological and orientational behavior of LCPs in complex flows.

2.2 Experimental Section

The model thermotropic polymer used here is a random copolyether of dihydroxy-α-methyl stilbene (DHMS) mesogens coupled with two different lengths of alkyl spacers (7- and 9-$(CH)_2$) to suppress its melting point. This polymer is referred to as DHMS-7,9 [14, 16]. The synthesis and characterization of DHMS-7,9 have been described in a previous paper [14]. All of our monodomain experiments were performed on the polymer with polystyrene-equivalent M_w of 11 000 g/mol and polydispersity of 2.1. The nematic phase of this polymer spans from 104°C to 157°C as determined by differential scanning calorimetry (Perkin-Elmer DSC 7) and high resolution powder X-ray diffraction, yet some remanent birefringent structure may persist up to 181°C under hot-stage polarizing light microscope. This is attributed to the wide distribution of molecular weights. Since T_{ni} determined by DSC and powder X-ray diffraction reflects the sample's bulk properties, we will use $T_{ni} = 157$°C as the nematic-to-isotropic transition point.

Experiments were conducted on a custom-made shear cell. The design of our flow cell was inspired from several apparatus available in the literature [17, 18, 19], with the added capability for magnetic alignment due to its small size. The essential features of this device comprise a static quartz window which can be accurately positioned using three micrometers with respect to a window mounted onto a spring-loaded mechanical translation stage. The interference fringes of the sample cell are used to adjust the parallelism of two window surfaces, giving ± 2.5 μm unparallelism across $\sim$ 1 cm field of view. Each window is independently heated by a mica heater (Minco, Inc.) and controlled by a process controller (CN-76000, Omega Inc.) with temperature stability to ± 0.2°C. The temperature variation over the whole window is estimated to be within ± 1°C. The motion of the bottom window is controlled by a micro-stepping motor (ζ-6104, Compumotor, Inc.).

The shear cell is used for monodomain preparation and *in situ* conoscopy studies at elevated temperature. The sample is sandwiched between two optical windows bearing rubbed polyimide alignment layers (SE-150, Nissan Chemical, Inc.). The rubbing directions of alignment layers have been kept either along the flow direction (1) or along the neutral direction (3). The gap thickness is 500 μm or 600 μm with uncertainty of 2.5 μm. This sample thickness enables an observation of approximately $8 \sim 10$ orders of interference. After loading the sample at a desired temperature in the nematic phase, we placed the

sample cell inside a strong magnetic field ($\sim$ 7 Tesla) to enhance bulk alignment. The magnetic field is oriented collinear to the rubbing direction. In the magnetic field, the polymer samples were first heated to the isotropic state and then slowly cooled down ($\sim$ 10°C/hr) to the nematic phase for annealing (typically 30-50 hrs) until a monodomain is achieved, as evidenced by formation of a conoscopic pattern. The shear cell was then transferred to a polarizing optical microscope. Conoscopic interference figures were observed using monochromatic light ($\lambda_0 = 633$ nm), and photographed for subsequent analysis.

2.3 Conoscopy and Data Analysis

Conoscopy provides a non-invasive interference technique to observe the optical anisotropy and orientation of minerals and crystals. Since nematic monodomain is a uniaxial crystal with its director orientation equivalent to its optical axis, conoscopy has been widely used to probe the director orientation of nematics during shear flow [3, 4, 19, 20, 21, 22, 23], and to measure the refractive indices of LCPs [24]. A thorough treatment of conoscopy principles may be found in monographs [25], and our intent here is to briefly review some optical results relevant to our experiments and analysis.

The conoscopic interference figure is generated by passing a highly convergent cone of light through the sample placed between crossed polarizers. Light rays having different incident angle experience distinct optical path length differences between their ordinary and extraordinary rays, and the interference figures that result are imaged on the back focal plane of objective lens. Visualization of the conoscopic interference figures is made possible by the use of a Bertrand lens. For an undistorted planar nematic monodomain, a typical conoscopy pattern consists of symmetric hyperbola-like principle isochromates placed parallel and perpendicular to the director orientation.

The conoscopic pattern may be used to extract the two refractive indices n_o and n_e, for the ordinary ray and extraordinary ray, respectively. When the plane of light incidence (containing light wave propagation vector $\mathbf{k}$ and electric field vector $\mathbf{E}$) is parallel to the director $\mathbf{n}$, the optical path difference, $\delta_{||}$, is given by [26]

$$\delta_{||}(\theta_i) = \frac{2\pi(\Delta n)d}{\lambda_0}\left(1 - \left(\frac{\sin\theta_i}{n_o}\right)^2\right)^{\frac{1}{2}}, \tag{2.1}$$

where θ_i is the incident angle from air into the window, and Δn is the birefringence of the nematic. When the plane of light incidence is perpendicular to $\mathbf{n}$, $\delta_\perp$ is given by [27]

$$\delta_\perp(\theta_i) \simeq \frac{2\pi(\Delta n)d}{\lambda_0}\left(1-\left(\frac{\sin\theta_i}{n_{eff}}\right)^2\right)^{-\frac{1}{2}}, \tag{2.2}$$

where n_{eff} is an effective refractive index of the equivalent isotropic medium, defined as

$$n_{eff} = \frac{n_e + 2n_o}{3}. \tag{2.3}$$

The two refractive indices can be obtained by fitting Eq. 2.1 and 2.2 to the positions of minima and maxima of transmitted light intensity on conoscopic interference figure. It is interesting to note that $\delta_{||}$ decreases monotonically with increasing θ_i, whereas $\delta_\perp$ increases monotonically with increasing θ_i, so the symmetry center of interference figure corresponds to the light path for which the sample retardance passes through a saddle point.

Upon shear flow, the director will rotate against the vorticity for a shear aligning nematic, but toward the vorticity direction for a tumbling nematic. The rotation of the director results in a shift of the symmetry center of interference figure. The apparent rotation angle θ_{app} for which the light path corresponds to the symmetry center is given by

$$\sin\theta_{app} = \left(\frac{r}{R}\right)\frac{NA}{n_{eff}} \tag{2.4}$$

where r is the displacement of the symmetry center of the hyperbolic fringe pattern, R is the radius of the full field of view of the conoscopic pattern, and NA is the numerical aperture of the objective lens. It must be noted that θ_{app} is not equal to the actual rotation angle of the director θ. The general relationship between θ and θ_{app} has been given in the literature [26] and is quite complex. Nevertheless, at the limit of small birefringence, a rather simple relation can be derived, giving $\theta \simeq \frac{1}{2}\theta_{app}$. We find this approximation is good even at a fairly large Δn; for example, when $\Delta n \simeq 0.2$, the error represented by this approximation is only about 4%.

2.4 Results

2.4.1 Qualitative Determination of Shear Aligning vs. Tumbling Character

Quiescent monodomains exhibit the hyperbolic fringe pattern characteristic of planar, optically uniaxial nematics (Figure 1a). Upon inception of shear flow, the interference figures are observed to shift in the direction that indicates the director rotates against the vorticity of the shear flow (Figure 1b&c). This observation provides unambiguous evidence that DHMS-7,9 is of shear aligning type. The same qualitative behavior was seen at all temperatures within the nematic phase.

2.4.2 Quantitative Determination of the Tumbling Parameter λ

The quantitative values of tumbling parameter λ may be extracted from the strain dependence of director rotation. Owing to the high viscosity of this polymer sample, the shear rates we have chosen (on the order of 10^{-2} s^{-1}) fall in the range of high Ericksen number Er$\gg$ 1, where Er=$\frac{\eta\dot{\gamma}d^2}{K}$ (η and K are characteristic viscous and elastic constants), so distortional elastic effects are weak compared to viscous effects. In addition, the shear rate is small enough so that the effect of conformational elasticity and local changes of molecular orientation can be neglected. In this limit, the director will experience a uniform rotation in response to an applied shear flow, except within two thin orientational boundary layers near the anchoring surfaces. By restricting the response of the director within the shear plane, i.e., flow-velocity gradient plane, the evolution of director orientation during flow can be described by the Leslie-Ericksen theory as follows:

$$\frac{d\theta}{d\gamma} = \frac{\alpha_2 \sin^2\theta - \alpha_3 \cos^2\theta}{\alpha_3 - \alpha_2}. \tag{2.5}$$

Here θ is the angle of the director orientation relative to the flow direction, γ is the applied shear strain, α_2 and α_3 are two of the six Leslie-Ericksen viscosity coefficients.

Thus, when hydrodynamic forces dominate over distortional elasticity, the director rotation is independent of shear rate and solely a function of applied strain. Indeed, no shear rate dependence of director rotation was observed in steady shear of a planar nematic monodomain (Figure 2). We have also imposed incremental shearing on a monodomain by applying strain stepwise in discrete intervals, and found that the director response $\theta(\gamma)$

is essentially identical to that observed upon inception of steady shear (Figure 3). These results confirm that the hydrodynamic terms are dominant, and more importantly the basic analysis of Leslie-Ericksen theory applies to polymeric nematics in the linear limit (i.e., at the shear rate slow relative to molecular relaxation).

For a shear aligning nematic, Eq. 2.5 may be integrated to give:

$$\tan\theta = \sqrt{\frac{\lambda-1}{\lambda+1}}\tanh\left(\frac{\gamma}{2}\sqrt{\lambda^2-1}\right). \tag{2.6}$$

In this expression, $\lambda \equiv (\alpha_2+\alpha_3)/(\alpha_2-\alpha_3)$ is the tumbling parameter. Shear alignment corresponds to values $|\lambda| > 1$, for which a steady orientation is obtained as $\gamma \to \infty$. The Leslie alignment angle increases with increasing the value of λ. Quantitative values of λ can be accurately determined by fitting Eq. 2.6 to the director response curve. For example, our experimental data at 130°C roughly tracks the theoretical trajectory for director evolution with $\lambda = 1.017$ (solid line in Figure 2). Curves for $\lambda = 1.014$ and 1.020 are also shown for comparison, and both show significant deviations from the experimental data. This demonstrates the high precision with which λ may be determined using this technique.

2.4.3 Temperature Dependence of the Tumbling Parameter

During flow startup, no qualitative change of shear aligning behavior is observed at different temperatures within the nematic phase. With increasing temperature, the director systematically rotates faster as a function of applied strain (Figure 4), suggesting a larger value of λ at higher temperature. In addition, a relatively small amount of strain is required for the director to approach the Leslie alignment angle at high temperature, consistent with expectation for a larger λ value. The flow alignment angle becomes progressively farther from the flow direction with increasing temperature.

The tumbling parameter of DHMS-7,9 decreases monotonically with decreasing temperature, but remains above unity throughout the nematic range (Figure 5). The observed temperature dependence of λ is qualitatively similar to that of small molecule liquid crystals, such as MBBA [28]. In the context of small molecule liquid crystals, the trend of λ with T is explained in terms of the increase in the order parameter S with deeper undercooling into the nematic phase.

2.4.4 Temperature Dependence of the Order Parameter

Since a direct comparison with molecular theories requires $\lambda(S)$, we estimate S using the temperature dependence of the optical anisotropy, more specifically, the temperature variation of the two refractive indices n_o and n_e. Like that of small molecule liquid crystal, the ordinary refractive index n_o shows a very weak temperature dependence over the entire nematic range, whereas the extraordinary refractive index n_e decreases monotonically as the nematic-to-isotropic transition is approached. We find the refractive indices can be reasonably well described by the two-parameter equation of the Vuks model [29, 30], given by

$$\log\left[\left(n_e^2 - n_o^2\right) / \left(n^2 - 1\right)\right] = \alpha + \beta \log\left(1 - T/T_{ni}\right). \tag{2.7}$$

Here, $n^2 = (n_e^2 + 2n_o^2)/3$ represents a squared average refractive index of the liquid crystal, and α is related to the anisotropy of its molecular polarizability. The parameter β describes the temperature dependence of the order parameter (S) by a simple relation

$$S = \left(1 - \frac{T}{T_{ni}}\right)^{\beta}. \tag{2.8}$$

The internal consistency of the Vuks model has been proven in small molecule liquid crystals, and the same analysis seems also to be valid for the present polymeric liquid crystal DHMS-7,9 (Figure 6a). As is the case of small molecule LCs [30], a slight deviation from Vuks model is observed as temperatures close to the nematic-to-isotropic transition. This curvature may be attributed to the pre-transitional effect.

With increasing temperature the order parameter and, consequently birefringence, decrease as a function of reduced temperature T/T_{ni} (Figure 6b). This can actually be understood from Eq. 2.7 in the limit of small birefringence. In this limit, Δn is found to be directly proportional to S with some prefactors. From refractive indices measurements, the order parameter of DHMS-7,9 is estimated to lie between 0.7 and 0.8 within the nematic range (Figure 6b). This value of S is larger than that of the small molecule LCs at the same T/T_{ni}, probably due to stronger exclude volume interaction of polymeric LCs. The shapes of $S(T/T_{ni})$ and $\Delta n(T/T_{ni})$ are very much alike, as expected.

2.4.5 Transient Director Response

Relaxation Following Cessation of Shear Flow

The shear-induced director rotation relaxes following cessation of shear flow. The symmetry center of conoscopic fringe pattern is observed to slowly recover to its original position. The director orientation roughly follows an exponential decay with a characteristic decay time $\tau \approx 9$ hrs at 130° (Figure 7). This relaxation is much slower than that of small molecule nematics ($\sim$ 100 s) [21]. Since the decay time scales as the ratio of the rotational viscosity to characteristic elastic constants K_i, $\tau \propto \gamma_1/K_i$, the slow director relaxation of this LCP implies a large value for γ_1/K_i. For DHMS-7,9 of 11000 g/mol molecular weight, γ_1 is estimated to be around 360 Pa·s from the kinetics of magnetic reorientation (assuming the diamagnetic susceptibility $\Delta\chi \simeq 10^{-8}$ c.g.s) [31]. Since the elastic constant is only about one order of magnitude larger for LCPs [32], the account for three orders of magnitude increase in γ_1/K_i for the present LCP compared to small molecule LCs is dominated by the change in γ_1 (360 Pa·s vs. 0.1 Pa·s), dictating slow relaxation of polymeric nematics.

Flow Orthogonal to Director

We also performed transient shear experiments on monodomains with their initial alignment along the neutral direction. In these experiments, we have deliberately introduced a small orientation bias (< 2°) by placing two alignment layers with their rubbling direction anti-parallel to each other. The bias direction is within the first quadrant of velocity-neutral plane (Figure 8). This director orientation breaks the symmetry of rotation upon inception of shear flow.

When the director orients at an angle close to the neutral direction, a "log-rolling" type of motion is predicted to be stable from the Doi model for rod-like lyotropic LCP [33], but for shear aligning DHMS-7,9, a complex director response is observed instead. Upon shear inception, the director immediately rotates counter-clockwisely (the axis of rotation along the velocity gradient direction) toward the positive flow direction (Figure 8), signaling a tendency of molecules to align along the flow direction even though they are 90° out of the shear plane. This out-of-plane director rotation is accompanied by a small horizontal shift of the interference figure in a direction opposite to the applied flow direction (Figure 8). The shift direction is also consistent with expectations for flow alignment. However, the

conoscopic pattern is lost after about 1 strain unit is applied (Figure 8) before the director is able to arrive to the Leslie alignment angle. Following disappearance of the conoscopic pattern, no phase grating associated with roll-cell instability [4, 34, 35, 36, 37] is observed when viewed in orthoscopic optics. Since the roll-cell formation is a signature of tumbling nematics, the absence of roll-cell in DHMS-7,9 also suggests flow alignment.

2.5 Discussion

2.5.1 A Unifying View of Aligning Properties for Mesogen-spacer LCP

The quantitative determination of λ in combination with mechanical and *in situ* shear orientation studies [14] in one model system provides a firm foundation for interpreting rheological and orientational behavior of thermotropic LCPs. In steady shear, DHMS-7,9 exhibits high shear-induced orientation in the nematic phase that is nearly independent of shear rate, a signature of shear aligning behavior. Similar shear orientation behavior has been observed in a different mesogen-spacer type thermotropic LCP (PSHQ-6,12) [13], suggesting that it too is of shear aligning type. The flow aligning character of DHMS-7,9 and PSHQ-6,12 is also in accord with their similarities in transient shear rheology: neither DHMS-7,9 nor PSHQ-6,12 shows sign of multiple stress oscillations that is characteristic of tumbling nematics. Finally, the prior qualitative conoscopy study on yet another mesogen-spacer type LCP ($OQ_{OE}O$-10) showed that it is also shear aligning in the nematic phase away from its nematic-to-smectic phase transition [15]. We thus infer that the flexibility of mesogen-spacer type LCPs produces shear aligning behavior in general. Taken together with the known tumbling character of rodlike lyotropic LCPs, these results highlight the crucial role of chain flexibility in controlling the dynamics of polymeric nematics.

2.5.2 Comparison of $\lambda(S)$ with Small Molecule LCs

Like shear aligning small molecule LCs, the tumbling parameter of DHMS-7,9 decreases with increasing order parameter (Figure 9); however, in contrast to small molecule LCs that are predicted to be tumbling type when S is above 0.6 [38], DHMS-7,9 remains shear aligning to $S = 0.8$. This discrepancy may be attributed to the effect of chain flexibility in mesogen-spacer type LCPs.

2.5.3 Comparisons with Molecular Models

Two different theoretical approaches have been taken in the literature to account for the effect of chain flexibility on main chain LCP dynamics, and both predict shear aligning behavior at high flexibility [8, 9, 10], in agreement with the data presented here for DHMS-7,9. The first approach explicitly incorporates molecular flexibility into model formulations, including the nematic dumbbell model [9] and nematic Rouse model [10]. These two models are essentially anisotropic generalizations of the ordinary dumbbell model and Rouse model, assuming LCP chain consists of nematic rods linked by elastic springs. According to the nematic dumbbell model, flow alignment occurs at all values of the molecular order parameter, and λ depends on S according to:

$$\lambda = \frac{2+S}{3S}. \tag{2.9}$$

The prediction of the nematic dumbbell model captures the qualitative trend of λ decreasing as a function of S, but this theory substantially overpredicts the value of λ (Figure 9). Quantitative comparisons between the nematic Rouse model and experimental data are not given, since λ is not explicitly expressed as a function of the order parameter. Nevertheless, the shear aligning character of flexible LCPs is also captured by the nematic Rouse model.

The second approach has extended the Doi model to semiflexible chains. Although a general theory for the effect of molecular flexibility on λ is still lacking, a couple of limits have been examined. For the limit of slightly flexible rods, i.e., small but finite ratio of chain length L to persistence length q ($0 < L/q \ll 1$), Subbotin found that λ is less than predicted for perfectly rigid rods ($L/q = 0$) except at high order parameters ($S > 0.82$) [39], suggesting that slightly flexible rods are more prone to be tumbling. While in the limit of flexible chains $L/q \rightarrow \infty$, Semenov found λ is always above unity [8]; therefore, flexible polymeric nematics are predicted to be flow aligning for all values of the order parameter. This prediction reinforces the qualitative character predicted by the nematic dumbbell model, and quantitatively shows much better accord with $\lambda(S)$ observed for DHMS-7,9 (Figure 9). Further, Semenov asserts that for finite L/q, the values of $\lambda(S)$ fall below the upper bound established for $L/q \rightarrow \infty$ [8]. This would further improve the agreement with the present results, since DHMS-7,9 of 11000 g/mol molecular weight only has a modest L/q value (based on independent measurement of the molecular weight dependence of viscous

coefficients, a DHMS-7,9 chain of this length only forms $O(1)$ hairpins [31]). Thus, combining our results with Subbotin and Semenov's theoretical predictions, it seems that a critical L/q value might exist, below which a transition from flow alignment to tumbling occurs at high order parameter, but above which flow alignment occurs for all values of S in the nematic phase.

2.5.4 Physical Insights for the Effect of Flexibility

We find that Semenov's semiflexible nematic chain model has best described the dynamical behavior of flexible LCPs; however, the physical basis for the prediction of shear aligning behavior in Semenov's model is not stated. For mesogen-spacer type thermotropes, the chain flexibility is so high that mesogens along a given chain can have different orientations, as illustrated in Figure 10. These mesogens will experience different hydrodynamic torques; however, connectivity through the chain limits their ability to rotate at different rates. The resulting frustration tends to suppress the occurrence of tumbling motion.

This physical picture may not generalize to the situation where the nematic chain has little flexibility, such as commercial thermotropes Vectra and Xydar. For these materials, the nematic chain has no flexible spacers, only units that introduce chain kinks. Since its persistence length can be fairly long, the orientation of mesogens only meander slightly along the chain contour. During shear, hydrodynamic torques might just rotate the entire chain as a slightly bending rod (Figure 10), so tumbling may still exist in these type of LCPs, as predicted by Subbotin [39]. Indeed, thermotropic hydroxypropylcellulose (HPC) has been inferred to exhibit tumbling behavior from an extrapolation of a series of mechanical experiments on tumbling lyotropic HPC solutions to a concentration of 100% [40]. The tumbling character of thermotropic HPC is also consistent with recent orientation studies showing that shear is only able to induce a low degree of orientation at small shear rate [41].

2.6 Conclusion

Our results represent the first direct, quantitative measurements of the shear aligning properties of a main chain thermotropic LCP. We find that incorporation of chain flexibility profoundly alters the dynamics of LCPs, suppressing director tumbling. For mesogen-spacer

type thermotropic LCP, the chain flexibility is so high that shear alignment is dominant. This is in direct contrast to rod-like lyotropic LCP for which director tumbling is the rule.

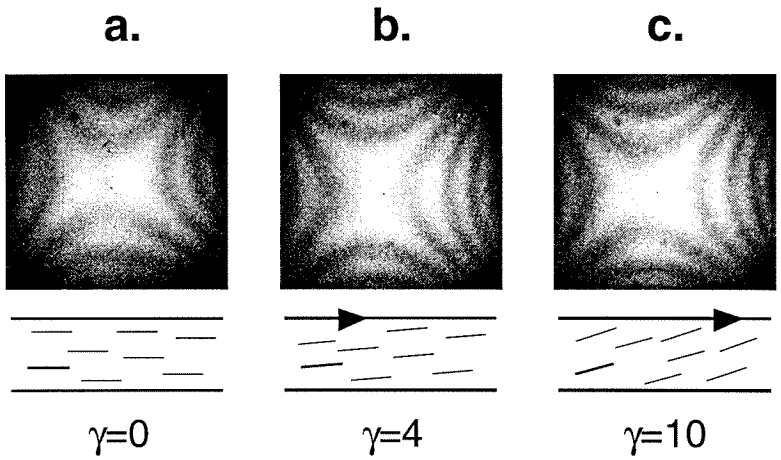

Figure 2.1: Conoscopic patterns observed in a planar DHMS-7,9 monodomain at 130°C for (a) quiescent conditions, and shearing for (b) 4 strain units and (c) 10 strain units at a rate of 0.02 s^{-1}. The schematic diagrams below each conoscopic pattern illustrate the deformation geometry and direction of the director rotation.

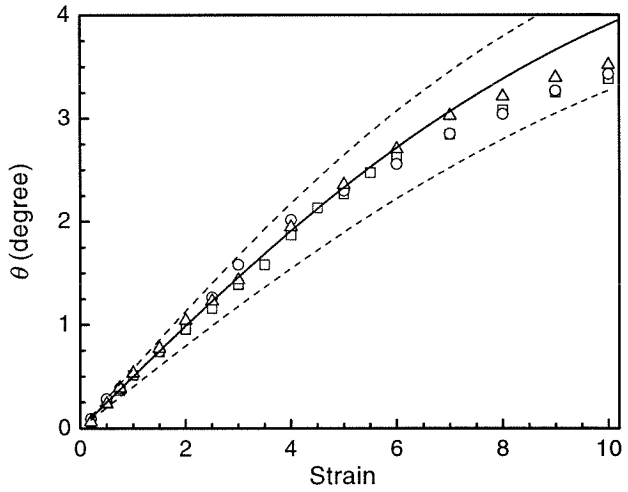

Figure 2.2: Director rotation θ as a function of applied strain at 130°C in DHMS-7,9 momodomain. Data presented here are for continuous shearing at rates of (□) 0.01, (○) 0.02, and (△) 0.05 s^{-1}. The solid curve is fit of Eq. 2.6 to 130°C data using value of $\lambda = 1.017$. The upper and lower dashed curves are computed using $\lambda = 1.020$ and $\lambda = 1.014$, respectively.

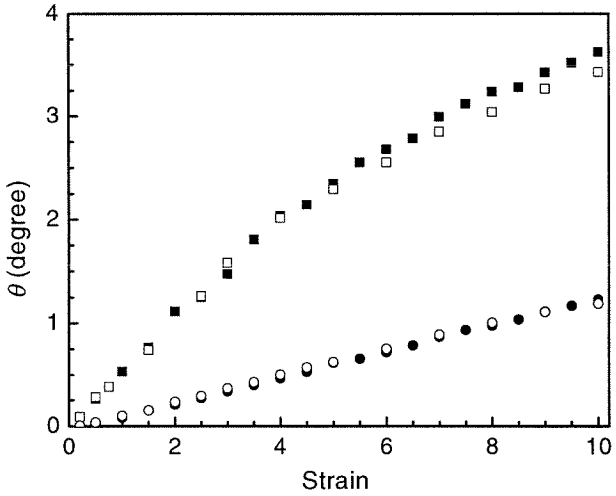

Figure 2.3: Evolution of director rotation θ as a function of applied strain during stepwise application of shear strain at temperatures of 130°C (filled square) and 110°C [●] in DHMS-7,9. Corresponding data obtained from continuous shearing at a shear rate of 0.02 s^{-1} at 130°C [□] and 110°C [○] are also included for comparison.

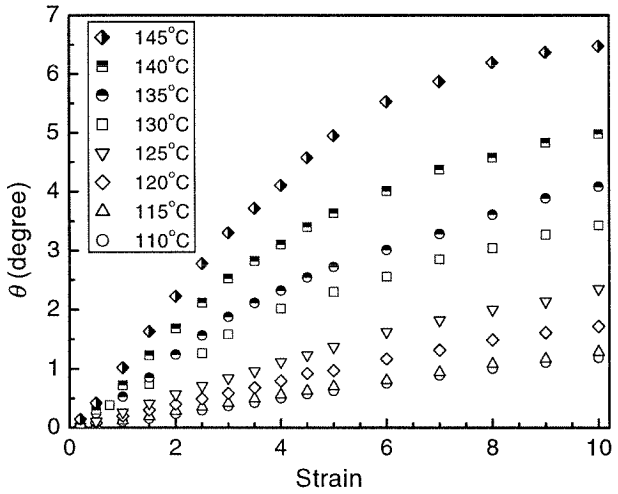

Figure 2.4: Transient director rotation as a function of applied strain during flow startup at various temperatures within the nematic range: 110°C (○), 115°C (△), 120°C (◇), 125°C (▽), 130°C (*Box*), 135°C (half-filled circle), 140°C (half-filled square), and 145°C (half-filled diamond).

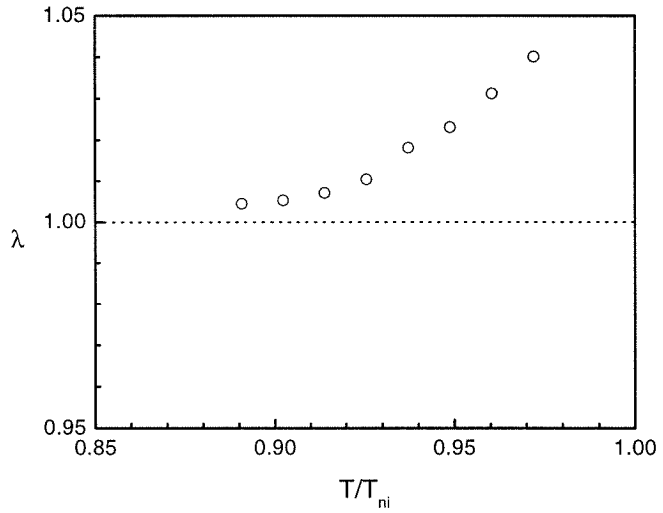

Figure 2.5: Tumbling parameter λ as a function of reduced temperature (T/T_{ni}). The dot line ($\cdots\cdots$) separates shear aligning region ($|\lambda| > 1$) from tumbling region ($|\lambda| < 1$).

a.

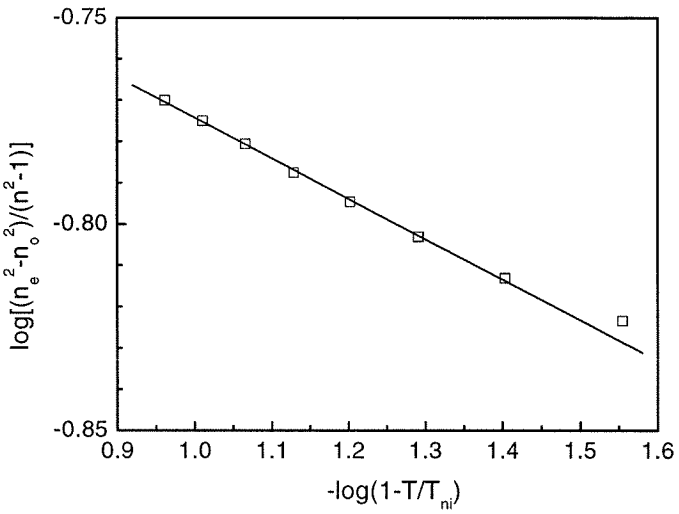

b.

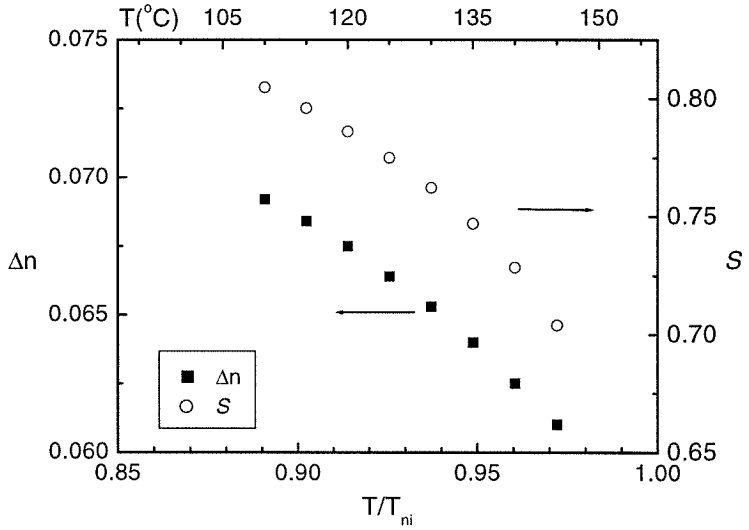

Figure 2.6: (a) Analysis of optical anisotropy using Vuks' model on DHMS-7,9 in extracting the temperature dependence of the order parameter β; (b) Birefringence (Δn) and the order parameter (S) as a function of reduced temperature T/T_{ni}.

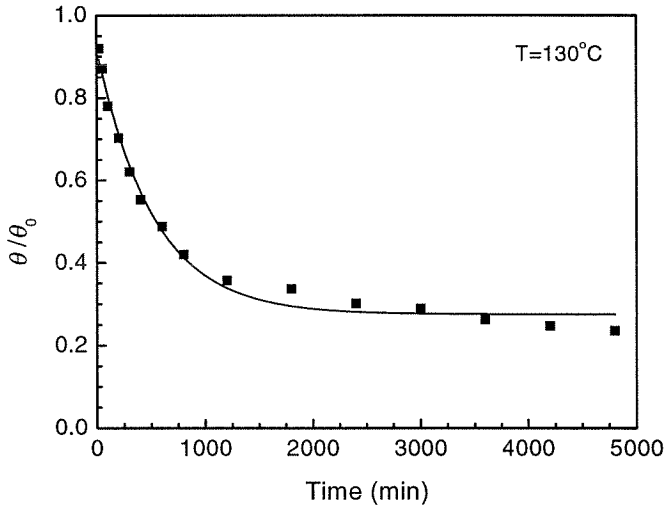

Figure 2.7: The normalized director orientation (θ/θ_0) as a function of relaxation time following cessation of shear flow for 10 strain units at 130°C, and θ_0 is the angle of director orientation after 10 strain units of deformation. The solid curve represents single-exponential decay fitting of director relaxation data.

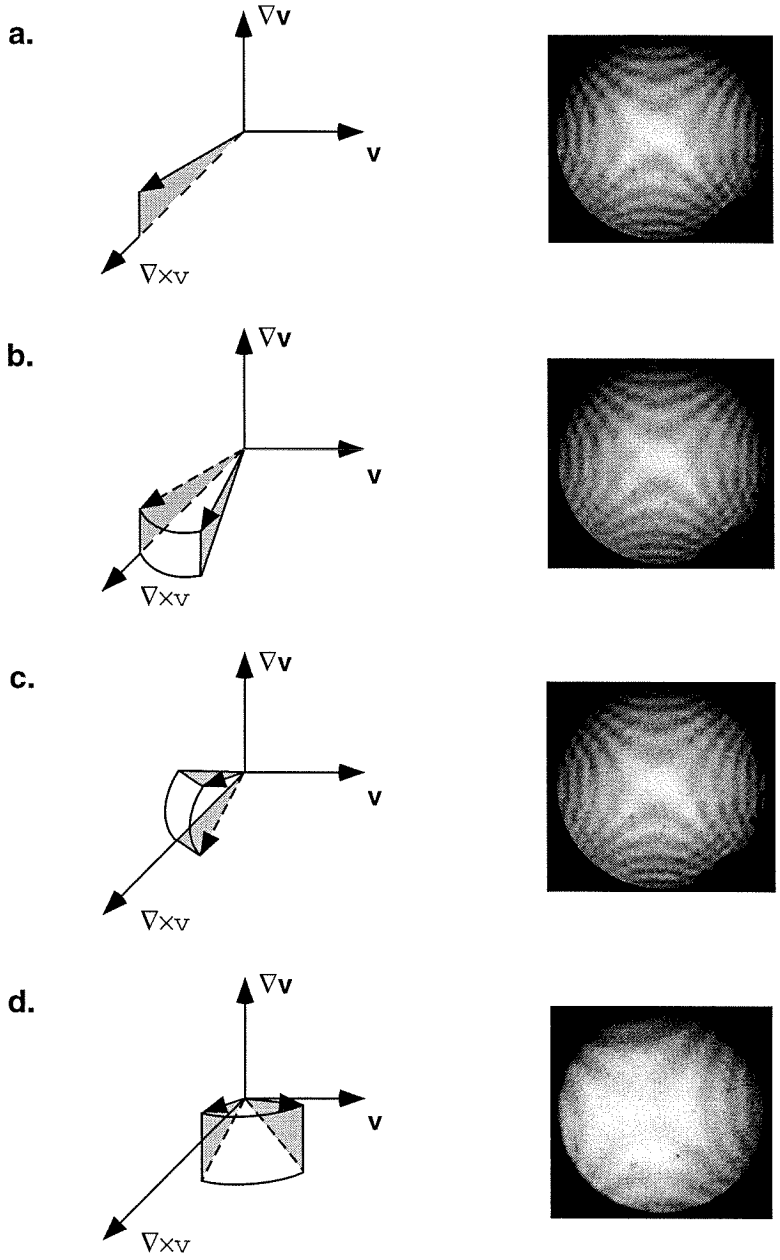

Figure 2.8: The transient director response of a planar DHMS-7,9 monodomain when the flow is applied orthogonal to initial director orientation. The schematic diagrams besides each conoscopic patterns illustrate how director responds to an othogonal flow.

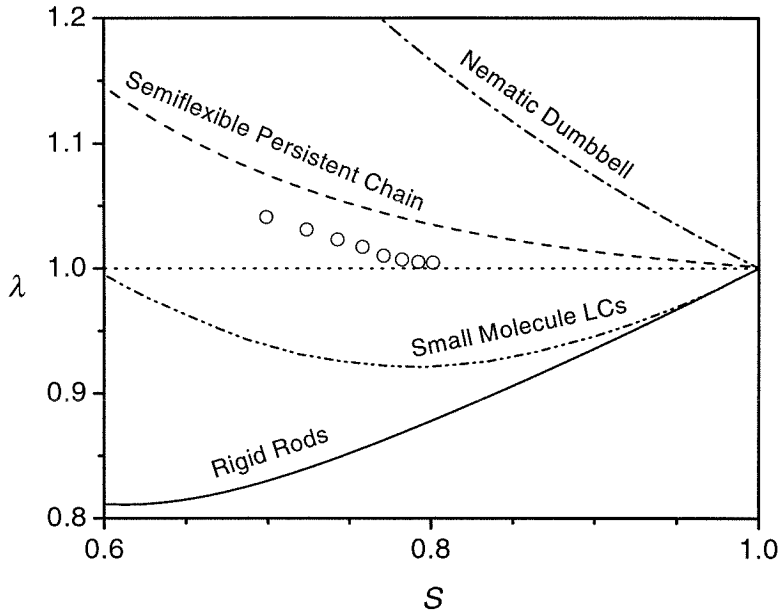

Figure 2.9: Tumbling parameter as a function of order parameter (S) for DHMS-7,9. The dot-dash curve (–·–·–) and dash curve (– – –) represent calculations of λ from the nematic dumbbell model and semiflexible nematic chain model at the limit of $L/q \to \infty$, respectively. The double dots-dash curve (–··–··–) shows the predicted values of λ as a function of S for small molecule liquid crystals using a Maier-Saupe potential, and the solid curve (——) represents the predictions of λ from the Doi model of rigid rods using spherical harmonic expansion.

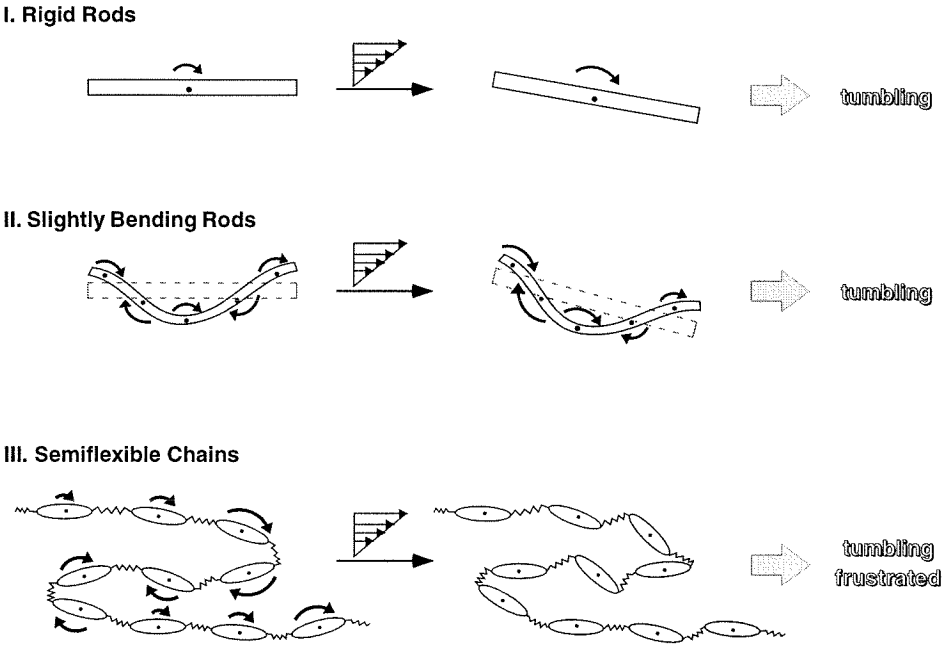

Figure 2.10: Schematic illustration for the non-montonic effect of molecular flexibility on the aligning properies of main chain LCP. Curved arrow represents hydrodynamic torque exerted on the polymer; its length indicates the magnitude of local torque. (I) Rigid rods: net hydrodynamic torques always act to rotate the director, leading to director tumbling; (II) Slightly Bending Rods are subject to even larger hydrodynamic torques than rigid rods, and consequently are even more susceptible to tumbling motion; (III) Semiflexible Chains: mesogens along the same chain have different orientation, so they experience different torques; however, chain connectivity frustrates their ability to rotate at different rates, suppressing tumbling motion.

Bibliography

[1] P. Pieranski and E. Guyon. *Phys. Rev. Letts.*, 32:924, 1974.

[2] P. E. Cladis and S. Torza. *Phys. Rev. Letts.*, 35:1283, 1975.

[3] W. R. Burghardt and G. G. Fuller. *Macromolecules*, 24:2546, 1991.

[4] M. Srinivasarao and G. C. Berry. *J. Rheol.*, 35:379, 1991.

[5] N. Kuzuu and M. Doi. *Jpn. J. Phys. Soc.*, 53:1031, 1984.

[6] G. Marrucci and F. Greco. *Adv. Chem. Phys.*, LXXXVI:331, 1993.

[7] W. R. Burghardt. *Macromol. Chem. Phys.*, 199:471, 1998.

[8] A. N. Semenov. *Sov. Phys. J. E. T. P.*, 66:712, 1987.

[9] P. L. Maffettone and G. Marrucci. *J. Rheol.*, 36:1547, 1992.

[10] D. Long and D. C. Morse. *Europhys. Letts*, 49:255, 2000.

[11] F. Cocchini, M. R. Nobile, and D. Acierno. *J. Rheol.*, 35:1171, 1991.

[12] S. Chang and C. D. Han. *Macromolecules*, 30:1656, 1997.

[13] V. M. Ugaz and W. R. Burghardt. *Macromolecules*, 31:8474, 1998.

[14] W-J. Zhou, J. A. Kornfield, V. M. Ugaz, W. R. Burghardt, D. R. Link, and N. A. Clark. *Macromolecules*, 32:5581, 1999.

[15] M. Srinivasarao, R. O. Garay, H. H. Winter, and R. S. Stein. *Mol. Cryst. Liq. Cryst.*, 223:29, 1992.

[16] E. Hall, C. K. Ober, E. J. Kramer, R. H. Colby, and J. R. Gillmor. *Macromolecules*, 26:3764, 1993.

[17] N. J. Alderman and M. R. Mackley. *Faraday Discuss. Chem. Soc.*, 79:149, 1985.

[18] R. G. Larson and D. W. Mead. *Liq. Cryst.*, 12(751), 1992.

[19] P. T. Mather, D. S. Pearson, and W. R. Burghardt. *J. Rheol.*, 39:627, 1995.

[20] J. Wahl and F. Fischer. *Opt, Comm.*, 5:341, 1972.

[21] J. A. Müller, R. S. Stein, and H. H. Winter. *Rheol. Acta*, 33:473, 1994.

[22] D. J. Ternet, R. G. Larson, and L. G. leal. *Rheol. Acta*, 38:183, 1999.

[23] D. M. Boudreau, H. H. Winter, C. P. Lillya, and R. S. Stein. *Rheol. Acta*, 38:503, 1999.

[24] H. Mattoussi, M. Srinivasarao, P. G. Kaatz, and G. C. Berry. *Macromolecules*, 25:2860, 1992.

[25] F. D. Bloss. *An Introduction to the Methods of Optical Crystallography.* Holt, Rinehart and Winston, New York, 1961.

[26] T. J. Scheffer and J. Nehring. *J. Appl. Phys.*, 48:1783, 1977.

[27] M. Born and E. Wolf. *Principles of Optics.* Cambridge University Press, 7th edition, 1999.

[28] H. Kneppe, F. Schneider, and N. K. Sharma. *J. Chem. Phys.*, 77:3203, 1982.

[29] M. F. Vuks. *Optics. Spectrosc.*, 20:644, 1966.

[30] I. Haller. *Prog. Solid State Chem.*, 10:103, 1975.

[31] W-J. Zhou, J. A. Kornfield, and W. R. Burghardt (manuscript in preparation), 2000.

[32] R. G. Larson. *The Structure and Rheology of Complex Fluids.* Oxford University Press, Oxford, 1999.

[33] R. G. Larson and H. C. Ottinger. *Macromolecules*, 24:6270, 1991.

[34] R. G. Larson. *J. Rheol.*, 37:175, 1993.

[35] E. Guyon, I. Janossy, P. Pieranski, and J. M. Jonathan. *J. Optics (Paris)*, 8:357, 1977.

[36] E. Dubois-Violette, G. Durand, E. Guyon, P. Manneville, and P. Pieranski. Solid state phys. (suppl.), 14(147), 1978.

[37] P. T. Mather, D. S. Pearson, and R. G. Larson. *Liq. Cryst.*, 20:539, 1996.

[38] L. A. Archer and R. G. Larson. *J. Chem. Phys.*, 103:3108, 1995.

[39] A. Subbotin. *Macromolecules*, 26:2562, 1993.

[40] C. M. Huang, J. J. Magda, and R. G. Larson. *J. Rheol.*, 43:31, 1999.

[41] E. M. Andresen and G. R. Mitchell. *Europhys. Letts.*, 43:296, 1998. *Europhys. Letts.*, 43:296, 1998.

Chapter 3 Rheology and Shear Orientation in the Nematic Phase

3.1 Introduction

The mechanical properties of LCPs are strongly dependent on the degree of macroscopic alignment, which is directly coupled to the applied flow field. Thus, it is essential to understand the effect of flow on molecular orientation in order to predict the influence of processing conditions on the mechanical properties in the final products. To date, development of theoretical model, which can eventually lead to rational control and design of thermotropic LCPs processing, has been continuously hampered by the difficulty in incorporating the molecular flexibility. On the experimental side, the lack of data probing the evolution of fluid structure during flow has limited a direct comparison with available molecular models. This situation leads to a rather poor understanding of the flow behavior of thermotropic LCP.

To address the need for structural data on thermotropic LCPs, we have extended studies of director response in monodomain samples to bulk rheology and shear orientation behavior of polydomain samples. Our study has exclusively focused on the model thermotropic LCP system, DHMS-7,9, since the interpretation of rheological data on commercial thermotropes may be complicated by many experimental uncertainties. For DHMS-7,9, the ability to erase prior thermal and flow history by heating the sample to isotropic state provides us an easy way to control initial sample morphology so that reproducible rheological data can be obtained.

In this chapter, our primary objective is to establish the relationship between bulk rheological properties and shear orientation behavior in both steady shear and transient shear flows of model thermotropic LCP. DHMS-7,9 shows a three-region flow curve accompanied by high and nearly constant shear-induced orientation over the entire shear rate range in the nematic phase. No multiple oscillations have been observed in stress and orientation response during transient shear flows. These results are consistent with our expectations for

flow-alignment of DHMS-7,9. Our structural data, together with similar shear rheology [1, 2] and orientation behavior [3] found in another mesogen-spacer type thermotrope PSHQ-6,12 (Figure 1.5), provide a strong foundation to interpret the flow behavior of semiflexible LCPs on the basis of flow alignment.

3.2 Experimental Section

3.2.1 Materials and Characterization

The synthesis of DHMS-7,9 has been described in the previous chapter, and its linear viscoelastic behavior has been studied in detail by Gillmor and coworkers [4]. Although samples of several different molecular weights have been synthesized and studied, data for a single sample are presented here; effects of molecular weight on the viscosity coefficients will be addressed separately in Chapter 4. This sample is characterized by a weight averaged molecular weight of 28 440 g/mol (polystyrene equivalent) and a polydispersity of 2.3.

DHMS-7,9 (M_w=28 440 g/mole) undergoes phase transitions at 92°C, 120°C and 192°C (Figure 3.1). The transition at 92°C on heating has been assigned to the melting of the polymer; this transition shows large thermal hysteresis, with crystallization occurring at approximately 35°C on cooling (10°C/min). The upper transition coincides with the isotropization point (192°C) observed by polarizing light microscopy. Between 120°C and 192°C, a typical Schlieren texture was observed, which indicates that DHMS-7,9 is nematic in this temperature region. Owing to the wide distribution of molecular weight for DHMS-7,9, the nematic-isotropic biphasic region is rather broad.

One interesting feature of DHMS-7,9 is the existence of an intermediate phase between crystalline solid and nematic phase (92°C to 120°C). No clear texture can be identified in this temperature range under polarizing light microscope. Although previous attempts to characterize the structure associated with this phase [5, 6] have failed to yield a definite description and consequently it has been referred to as x-phase, our recent mechanical studies have identified rheological similarities to behavior associated with layered fluids such as lamellar block copolymers. The shear rheology and orientation behavior of Phase X are distinctly different from that of the nematic phase, and will be discussed separately in Chapter 5. In this chapter, we only present data obtained in the nematic phase.

3.2.2 Rheological Measurements

The polymer as synthesized above is in either fibrillar or powder form. Specimens for rheological measurements were prepared by solvent casting. DHMS-7,9 was dissolved in $CHCl_3$ in the presence of 0.75% of antioxidant Irganox 1010 (Ciba-Geigy). The solvent was evaporated slowly from the polymer solution at room temperature for a few days. The cast polymer film was then dried for at least 24 h under vacuum (<1 mm Hg) at 80°C. Samples were subsequently fabricated into 25mm or 50mm disks with 1mm thickness by molding in a heated press at 140°C. Before the sample was loaded into a rheometer, the molded disk was further dried under vacuum overnight at 80°C to remove moisture. This sample preparation avoids possible voids in the sample. These procedures have proven to give reproducible rheological data. We did not see evidence of significant offgasing problems as reported by Kalika and coworkers [7], which is a typical concern for thermotropic polyesters. DHMS-7,9 was thermally stable in the nematic phase for at least 3-4 days without a discernible change of the linear viscoelastic response. This enables prolonged rheological measurements. We are thus able to examine steady shear flow behavior even at rather low shear rates ($\dot{\gamma} \leq 0.01\ s^{-1}$).

The Rheometrics ARES rheometer (equipped with 2000 g-cm transducer) was used for most rheological measurements. The polymer sample is heated using a forced convection heating oven (up to 400°C) with temperature stability to ± 0.2°C. All of our experiments were performed under continuous dry nitrogen purge to prevent oxidative and hydrolytic degradation. We heated the sample to 205°C (isotropic state) and held it for 20 minutes to erase prior mechanical and thermal history. The sample was then cooled to the desired temperature in the nematic phase (or x-phase) with an additional 30 minutes thermal equilibration time before commencing flow experiments. *In situ* flow X-ray studies followed the same experimental protocol.

A parallel-plate geometry (diameter=50 mm, gap=1 mm) was used in studying the temperature dependence of apparent shear viscosity at a fixed rim shear rate. Measurements were performed at temperatures spaced every 5°C over the interval 100-200°C. For each measurement, the samples were presheared for 150 s.u. (strain units) at the sample rim to attain steady state before data collection. The same sample geometry was employed for dynamic temperature sweep experiments because it is easier to compensate for thermal

expansion of the tool fixtures ($\approx$ 3 μm /°C) in the parallel-plate geometry than in the cone-and-plate geometry.

Oscillatory dynamic data were collected as a function of angular frequency (ω). A parallel-plate geometry (diameter=50 mm, gap=1 mm) was used for randomly oriented samples. Strain amplitude (at the rim) varied from 1% to 30% at frequencies between 100 and 0.01 rad/s. It was verified that linear viscoelastic response holds over this range of strain amplitude. Little difference was observed when a cone and plate configuration was used. For dynamic measurements in well-oriented states (obtained by preshearing at selected shear rates), cone-and-plate fixtures (diameter=25 mm, cone angle=0.1 rad) were used in order to achieve uniform shear throughout the whole sample during preshear.

Measurements of steady shear viscosity (η) and first normal stress difference (N_1) in the nematic phase were also conducted in the cone-and-plate configuration (50 mm diameter-0.04 rad cone angle). The ARES rheometer was used to investigate shear rates in the range 0.01 to 10 s^{-1}. Measurements at lower shear rates ($\dot{\gamma}$ <0.01 s^{-1}) were performed on the Rheometrics stress rheometer (SR-5000) equipped with a more sensitive transducer (100 g-cm). Melt fracture was observed at shear rates above 10 s^{-1} in the nematic phase.

3.2.3 Rheo-X-ray Protocol and Data Analysis

The rheo-X-ray flow cell is a modified Linkam CSS-450 high temperature shearing stage; the details have been described elsewhere [3]. This device provides a parallel disk shearing geometry such that orientational anisotropy is probed in the flow-vorticity plane. High speed grid and CCD detectors were used for data acquisition, which enabled 2-D scattering patterns to be collected at intervals as short as 2 seconds, therefore providing sufficient time resolution to study transient flow phenomena. Scattering experiments were conducted on beam lines 5-BM and 5-ID at the Advanced Photon Source located at Argonne National Laboratory. The sample thickness was 1 mm in all experiments, and the energy of incident monochromatic radiation ranged from 15 to 25 keV ($\lambda = 0.80 \sim 0.62$Å) in different experimental runs.

Molecular Orientation is quantified from X-ray scattering patterns following the analysis used by Mitchell and Windle [8], where the degree of anisotropy is characterized in terms of an orientation parameter, S, whose value ranges from zero, corresponding to random alignment of molecules, to unity, corresponding to perfect alignment of all molecules along

the flow direction. In textured LCPs, the value of S reflects a combination of contributions from both the degree of alignment with respect to the director at the local molecular level, and the distribution of *director orientation* throughout the bulk "polydomain" samples (see Figure 3.2). Experimentally, S is determined from an average of the second Legendre polynomial weighted by an azimuthal intensity scan taken from the 2-D scattering pattern at the scattering vector associated with the equatorial nematic intermolecular correlation peak

$$S \equiv \frac{\langle P_{2n}(\cos\alpha)\rangle}{\langle P_{2n}(\cos\alpha)\rangle_0} = -2\left[\frac{\int_0^{2\pi} I(q,\alpha)P_{2n}(\cos\alpha)\sin\alpha d\alpha}{\int_0^{2\pi} I(q,\alpha)\sin\alpha d\alpha}\right]. \tag{3.1}$$

Here, the azimuthal angle α is defined with respect to the flow direction, and q is the magnitude of scattering vector at which the azimuthal scan is obtained. This analysis expresses the degree of alignment relative to the idealized case of perfectly aligned rods.

3.3 Linear Viscoelastic Behavior

In the isotropic phase, the linear viscoelastic response of DHMS-7,9 is different from that of simple flexible polymers. The dynamic moduli do not show characteristic terminal behavior at any of the temperatures studied (Figure 3.3). Both the storage and loss moduli are roughly proportional to $\omega^{0.85}$ at low frequency in the isotropic phase. This agrees with Gillmor and coworkers' studies on the same system with slightly higher M_w [4] but differs with Kim and Han's studies on thermotropic polyester (PSHQ) [1], where no difference from flexible polymers was observed in the isotropic state. It is not clear why terminal regime is absent for DHMS-7,9, but the possibility of a remnant birefringent structure in the isotropic state suggested by Gillmor and coworkers was excluded by direct observation through a polarizing light microscope in the present case.

In the nematic phase, time-temperature superposition nearly holds for DHMS-7,9 with a random polydomain orientation. Departure from time-temperature superposition is most evident at the low frequency in the vicinity of T_{ni} (Figure 3.2). Approximate shift factors are determined by shifting along the frequency axis alone until the storage and loss moduli at high frequency roughly superpose. The change in the shape of the relaxation spectrum with temperature is not monotonic (Figure 3.3). On cooling, the storage modulus at low reduced frequency first drops (starting at $T \approx T_{ni} + 20°\text{C}$). This drop is most significant at the isotropization point ($T = 192°\text{C}$). Then G' rises as temperature drops to $T \approx$

T_{ni} – 10°C. Once the transition is complete ($T \leq 175$°C), G' approximately superposes with that observed in the isotropic phase at 220°C. Like the case of the isotropic phase, no terminal response for G' was observed in the nematic phase. The absence of terminal regime has also been reported for the same DHMS-7,9 system with different M_w [4] and other thermotropic systems [1, 9]. This could be attributed to the effect of large-scale defect structure, as suggested by Gillmor and coworkers [4].

3.4 Steady Shear Rheology and Orientation

3.4.1 Flow Curve

In the nematic phase, the shear stress (σ) reaches steady state at about 40 s.u. after flow inception. The stress curve usually exhibits a large overshoot and then decays away to steady state. Unlike the case for lyotropic systems [10], no multiple oscillations were observed for flow start up. The viscosity curve (η versus $\dot{\gamma}$) is consistent with the typical three-region flow behavior (Figure 3.4), shear thinning at low rates ($\dot{\gamma}$ <0.05 s^{-1}), pseudo-Newtonian at intermediate rates (0.05 s^{-1} < $\dot{\gamma}$ <1 s^{-1}), and shear thinning again at high rates ($\dot{\gamma}$ >1 s^{-1}). No qualitative change in the shape of the flow curve with temperature was observed within the nematic phase.

The first normal stress difference (N_1) required a longer shearing time (about 100 s.u.) to arrive at its steady-state value in the nematic phase. Temperature fluctuations lead to fluctuations in the normal force over the course of measurements. The data reported here are time averages over 100 s.u. after N_1 reaches steady state. At shear rates below 0.1 s^{-1}, the first normal stress difference is below the sensitivity of our instrument. N_1 is positive at shear rates above 0.1 s^{-1}, and grows nearly proportionally with the applied shear rate (Figure 3.4). No reproducible N_1 data could be obtained at shear rates above 10 s^{-1} in the nematic phase due to edge fracture.

3.4.2 Orientation in Steady Shear

Representative X-ray scattering patterns in the isotropic and nematic phase are shown in Figure 3.5. The patterns are characterized by a diffuse ring in the isotropic phase corresponding to a value of $S = 0$ (Figure 3.5a), indicating the absence of any preferred direction of molecular alignment. This pattern is unchanged when the sample is sheared at moderate

rates in the isotropic phase. When a quiescent sample is cooled into the nematic phase, the isotropic ring pattern is retained despite the local ordering, as a consequence of the random distribution of "domain" orientations. When the sample is sheared in the nematic phase, an anisotropic scattering pattern is generated (Figure 3.5b), characterized by two diffuse equatorial peaks whose radial position is related to an average intermolecular correlation length around 5.5 Å, corresponding to the lateral packing of mesogens in the nematic phase. Azimuthal scans to extract orientation parameters are taken at the scattering vector corresponding to this peak.

At temperatures well within the nematic phase (140, 150°C), there is little change in shear-induced orientation with the applied shear rate (Figure 3.6). A slight decrease in orientation is observed at 170°, as the nematic-to-isotropic transition is approached. The temperature dependence of shear orientation is strongly correlated with steady shear viscosity: a significant drop in steady shear viscosity accompanies the development of molecular orientation upon cooling from the isotropic phase into the nematic phase, and both quantities remain nearly constant at intermediate temperatures within the nematic phase. The orientational behavior of DHMS-7,9 is qualitatively similar to that of PSHQ-6,12 previously studied by Ugaz and Burghardt [3].

The observation that the degree of molecular orientation in steady shear flow is not significantly influenced by shear rate is consistent with the behavior expected for a flow-aligning material, where prolonged shear promotes molecular alignment at the Leslie alignment angle with respect to the shearing direction. Provided that the shear rate is small relative to molecular relaxation time, the linear continuum theory of Leslie and Ericksen predicts that this angle is independent of shear rate. Therefore, all the molecules tend to orient at the same direction, giving rise to high and nearly constant shear orientation. In the case of a tumbling material, however, an enhancement in the degree of orientation is expected with increasing shear rate as a consequence of the dynamic transition from tumbling to flow-alignment, and has indeed been observed in lyotropic systems by Hongladarom and coworkers [11, 12, 13].

3.5 Transient Shear Rheology and Orientation

3.5.1 Relaxation Following Cessation of Steady Shear

Aside from a slight decrease over time, there is little change in the degree of molecular orientation observed during relaxation after flow cessation (Figure 3.7a). Indeed, S remains essentially unchanged from the value attained in steady shear flow. This observation agrees well with recent neutron scattering data of Dadmun and coworkers on the same system with different molecular weight [14]. Qualitatively similar relaxation behavior has also been observed in PSHQ-6,12 by Ugaz and Burghardt [3]. In the case of PSHQ-6,12, the lack of significant structural re-arrangement during relaxation provides a direct explanation for mechanical response observed by Chang and Han in interrupted shear flow [2], where the overshoot in shear stress associated with the initial start-up transient was not observed to re-develop over relaxation periods of up to one hour. For DHMS-7,9, a weak stress overshoot starts to appear upon resumption of shear flow after delays on the order of one hour (Figure 3.7b), and the magnitude of which is a function of relaxation time. These observations are qualitatively similar to that of PSHQ-6,12, suggesting that shear stress overshoots observed during flow inception from a random polydomain state are directly related to domain reorientation as shear promotes alignment at the Leslie angle.

In contrast to the orientation response during relaxation, the dynamic modulus G^* exhibits an initial rapid decay over approximately the first 100 seconds, followed by a more gradual decay during the remaining relaxation period (Figure 3.8). In lyotropic systems, changes in the dynamic moduli during relaxation often result from significant structure reorientation [11, 12]. We found that the changes in modulus for DHMS-7,9 during relaxation is also accompanied by some structural re-arrangements. On a time scale that correlates the initial drop in G^*, optical bands are formed under cross polarizers (Figure 3.9). These bands are perpendicular to the previously applied flow direction and can persist for a few minutes. Upon further relaxation, some distortion on those bands starts to occur and eventually bands disappear. It is a little bit surprising that these texture changes do not have significant effect on the average orientation state probed by X-ray scattering.

3.5.2 Rheology and Orientation During Flow Inception

The evolution of shear stress during flow inception is characterized by a single overshoot peak (Figure 3.10a), and no significant oscillations are observed in the shear stress transient. A steady state value of shear stress is attained after approximately 40 strain units is applied to the sample. The development of molecular orientation increased monotonically to a steady value (Figure 3.10b). Three sets of orientation data show excellent strain scaling with no obvious oscillatory behavior. Furthermore, a steady state value of S is reached after approximately 40 strain units have elapsed — the same strain range required for the shear stress to attain a steady state. The absence of significant oscillation in shear stress and orientation parameter are consistent with expectations of flow-aligning LCPs.

The mechanical response of DHMS-7,9 appears to be very sensitive to temperature change (Figure 3.11a). The magnitude of the stress overshoot decreases considerably as temperature is increased toward the isotropic transition. Even at two temperatures (140°C and 160°C) well within the nematic phase, the stress overshoot peak is significantly subdued at higher temperature (at 160°C in Figure 5.11a). The development of molecular orientation, however, shows little temperature dependence. At all temperatures studied, S shows a monotonic increase towards a steady state after applying 40 strain units and the shape of orientation evolution is roughly the same (Figure 3.11b). As before, no significant oscillations are evident in both the orientation or shear stress response during flow startup.

3.5.3 Rheology During Step Up/Down Flow

The shear stress shows a weak overshoot peak following a step up change of the shear rate after steady flow (Figure 3.12), suggesting much less severe domain reorientation from steady state achieved at lower shear rates. In fact, step change of the shear rate from 0.2 s^{-1} to 0.5 s^{-1} resulted in a slightly smaller overshoot peak than that from 0.1 s^{-1} to 0.5 s^{-1}. When the shear rate is reduced, no obvious oscillatory peak can be identified in both cases (Figure 3.12). The absence of oscillatory behavior after stepwise change of the shear rate is different from tumbling lyotropic LCPs, and again signals the flow-aligning behavior of DHMS-7,9. Since shear-induced orientation is nearly constant over the entire range of shear rate (Figure 3.6), a step up or down the shear rate would not perturb the molecular orientation, but merely change the magnitude of the shear stress as we observed.

3.5.4 Rheology and Orientation During Flow Reversal

Upon reversal of shear flow direction, the transient stress response is characterized by a single overshoot peak similar to that observed during flow inception; however, additional strain is necessary in order to attain a steady state (Figure 3.13). The transient data show excellent strain scaling, and do not exhibit any sign of oscillatory behavior. As was the case in flow inception, shear stress transients show a strong temperature effect. Compared to the large overshoot observed after flow reversal at 140°, the stress response is substantially subdued at 180°, suggesting a more modest change in orientation at higher temperatures. Recall, however, that the shear stress overshoot upon flow inception decreased dramatically with increasing temperature even when the orientation response remained qualitatively similar (Figure 3.8b), thus, it is not clear to what extent the weaker stress overshoot at 180° is due to the smaller orientation effects as opposed to the increase in temperature.

The orientation parameter during flow reversal exhibits an initial drop followed by a gradual recovery back to steady state values (Figure 3.13b). Nearly 100 strain units are required to re-establish the steady state level of alignment, indicating that molecular orientation evolves much more slowly during flow reversal than during flow inception from random polydomain state. This is not surprising because the reorientation associated with a flow reversal is expected to be more severe than that associated with flow inception, possibly involving a rotation of the director of nearly 180° in flow reversal as compared to an average director rotation of 90° in flow inception. As the temperatures increases, the magnitude of the orientation drop after flow reversal decreases (data not shown), which is consistent with the close proximity to the nematic-isotropic biphase regime. The transient orientation data evolves over a similar strain range as shear stress and also shows excellent strain scaling with no obvious oscillatory behavior. It is well-established that shear reversal in tumbling lyotropic LCPs leads to pronounced oscillations in stress and microstructures; the absence of such oscillatory behavior here is again consistent with the presumed flow-aligning dynamics.

3.5.5 Rheology and Orientation During Non-Steady-State Reversal

We have also performed a series of flow reversals during the transient portion of a flow inception experiment, starting from a random initial condition. That is, reversals were

conducted after varying amounts of shear strain had been applied, but the sample had not yet reached a steady state level of orientation. Upon flow reversal at low values of pre-shear strain ($\gamma_i < 50$ s.u.), the magnitude of the shear stress overshoot peak reduces as the amount of preshearing is increased (Figure 3.14a). The stress overshoots observed in these non-steady-state reversal experiments roughly fall within the range between independent measurements of the stress transients for flow inception and reversal from steady state, shown in Figure 3.7a and 3.10a, respectively. At higher pre-shear strains, as the sample approaches its steady state, the transient stress response comes to resemble the behavior seen in shear flow reversal. This is particularly evident in the increasing amounts of strain that must be applied in order to reach a steady state value of orientation after the reversal. Thus, the response of the material to non-steady-state reversals seems to involve some combination of the dynamics associated with flow inception and reversal from steady state, the relative contribution of which are modulated by the amount of pre-shearing strain values.

Similar to the mechanical behavior, the corresponding orientation data (Figure 3.14b) show that increasing amounts of strain are required for the orientation parameter to reach a steady state value as the amount of pre-shearing applied prior to the reversal is increased. The orientation data also show a reduction in the magnitude of the undershoot peak as the amount of pre-shearing is increased, suggesting a strong correlation between the evolving orientation states and shear stress response — large changes in S are associated with large transient stresses. Qualitatively similar orientation behavior has also been observed in non-steady-state reversal experiments of PSHQ-6,12 system [15].

3.5.6 Rheology and Orientation During Oscillatory Shear

Under oscillatory shear flow, the complex shear viscosity of polydomain sample ($|\eta^*|$) decreases continuously with time (Figure 15a). This continuous drop in $|\eta^*|$ can be attributed to a gradual development of macroscopic alignment under oscillatory shear. At low frequency ($\omega \leq 1$ rad/s), $|\eta^*|$ is nearly constant except for a slight decrease over time; at intermediate frequency ($\omega = 5$ rad/s), $|\eta^*|$ shows a more significant drop; while at high frequency, $|\eta^*|$ drops roughly to 20% of its initial value over a little bit more than 1000 sec of shearing (Figure 15a). These observations suggest that macroscopic alignment can be achieved in relatively shorter time at higher oscillatory frequency. In fact, when the normalized complex shear viscosity is plotted vs. ωt, which is equivalent to an effective

strain accumulated during oscillation, all data points are collapsed on a single curve (Figure 15b). We therefore infer that the accumulated strain is the critical factor that controls the degree of anisotropic development. This is also supported by a separate series of experiments performed at the same frequency but different oscillatory strain amplitude, showing that larger strain amplitude shear tends to align samples more rapidly than small stain amplitude shear.

Like that of mechanical data, the corresponding WAXS data also show that oscillatory shear induce macroscopic alignment. At low frequency (ω = 0.5, 1 rad/s), there is only a small amount of orientation anisotropy developed after 1000 sec of shear (Figure 16), as expected from a slight decrease in complex shear viscosity at these conditions. A nice correlation is also found between the structural data and mechanical data at high frequency (ω = 20 rad/s), where shear after the same amount of time induces a large degree of molecular anisotropy (Figure 16) that is accompanied by a significant drop in the complex shear viscosity.

3.6 Model Predictions of Rheology and Orientation

Significant progress has been made on modeling of LCP rheology over the past decade [3, 16, 17]. The predictions from several classes of polydomain models have been compared with our experimental data by Ugaz and coworkers [18]. Here, a polydomain simulation based on Ericksen's transversely isotropic fluid (TIF) model will be briefly discussed, and its performance in capturing the qualitative features of thermotropic LCP rheology will be assessed.

The approach of Ericksen polydomain simulation is to account for the polydomain texture by generating a large ensemble of random initial orientation states, and solving the director evolution equation for each member of the ensemble upon shear flow. The response of each individual domain is assumed to follow the description of Ericksen's transversely isotropic fluid model, which is a simplified version of the Leslie-Ericksen formulation by neglecting distortional elastic effects. The response of polydomain sample can then be determined by computing the averaged director response over all the domains within the ensemble.

3.6.1 Prediction of Orientation Development

We define the flow direction, velocity gradient direction, and neutral direction as 1, 2, and 3, respectively, and represent the director in three dimensions by $\mathbf{n}=(n_1, n_2, n_3)$. Recall that the director response of each monodomain depends only on the tumbling parameter λ, and the orientation of the director can be related to experimental X-ray scattering measurements (in 1-3 plane) of orientation parameter (S) as follows:

$$S \equiv \overline{S}_{11} - \overline{S}_{33} = \left\langle n_1^2 \right\rangle - \left\langle n_3^2 \right\rangle, \tag{3.2}$$

where $\overline{S}_{ij}$ are the components of the mesoscopic order parameter tensor: $\overline{\mathbf{S}} = \langle \mathbf{nn} \rangle - \boldsymbol{\delta}/3$, and $\langle \cdots \rangle$ represents an average over the ensemble of domain orientations.

The qualitative trend toward a monotonic increase of anisotropy with applied strain has been successfully captured by Ericksen polydomain model (Figure 3.17). The behavior of DHMS-7,9 is similar to that of PSHQ-6,12 previously studied by Ugaz and Burghardt [3], except that the degree of anisotropy evolves somewhat more slowly for DHMS-7,9. Further, the quality of the fit to experimental data is not as good as in the case of PSHQ-6,12. This is because there is a limit to how slowly anisotropy can evolve toward the steady state value from Ericksen polydomain model. Since we know that λ for DHMS-7,9 of 11 000 g/mol molecular weight lies between 1.005 and 1.041 in the nematic phase, and molecular theories predict a smaller λ for higher flexibility chain [19], the tumbling parameter for DHMS-7,9 of 28 440 g/mol molecular weight is thus expected to be very close to unity. Hence, an attempt to find a "best fit" to the orientation data yields a value of λ which is too close to unity to provide an unambiguous estimate of the tumbling parameter.

3.6.2 Prediction of Shear Stress

The Ericksen polydomain model makes the following predictions of shear stress and first normal stress difference:

$$\sigma_{12} = \left[\mu + 2\mu_1 \left\langle n_1^2 n_2^2 \right\rangle + \frac{\mu_2}{2}\right] \dot{\gamma} \tag{3.3}$$

$$N_1 = 2\mu_1 \left[\left\langle n_1^3 n_2 \right\rangle - \left\langle n_1 n_2^3 \right\rangle\right] \dot{\gamma} \tag{3.4}$$

Here, μ, μ_1 and μ_2 are three viscosity coefficients, which are phenomenological constants in the Leslie-Ericksen formulation. To proceed, we have to appeal to predictions from molecular models for the values of three viscosity coefficients. Since mesogen-spacer type thermotrope such as DHMS-7,9 has very high flexibility, the predictions of μ_i's from nematic dumbbell model and nematic Rouse model are expected to be more appropriate than the Doi model for use to make stress predictions. In the linear limit, the relative magnitudes of μ, μ_1 and μ_2 for a given value of λ are found to be identical for the nematic dumbbell model and nematic Rouse model, given by

$$\frac{\mu_1}{\mu} = \frac{2\lambda}{\lambda - 1} \tag{3.5}$$

$$\frac{\mu_2}{\mu} = -2. \tag{3.6}$$

This set of viscosity values is therefore used to compute the stress curve during shear flow.

Upon flow inception, the shear stress is predicted to exhibit an overshoot before finally arriving at its steady state (Figure 3.18), in qualitative accord with experimental data (Figure 3.10a). The magnitude of stress overshoot as well as the strain required to approach the steady state is a strong function of tumbling parameter λ. At values of λ near unity, the shear stress exhibits a significant overshoot during the transient approach to the flow alignment angle, and this overshoot becomes progressively smaller relative to their steady state values with increasing λ. As was the case of orientation prediction, the shear stress is found to evolve much faster (approximately 10 strain units from simulation, versus 40 strain units from experimental data) to steady state. Although a smaller λ value can explain the slow stress and orientation evolution, the resulting stress overshoot would be significantly larger than experimental observations of only 4-6 times of their steady state value.

3.7 Discussion

3.7.1 Steady Shear Flow

The steady shear flow behavior of nematic DHMS-7,9 shows certain similarities and differences compared to that of rigid-rod-like lyotropic LCPs. The viscosity follows a three-region flow curve, similar to that found in some commercial thermotropes [20, 21] and some nematic lyotropes (such as HPC) [22]. However, the value of the Region II viscosity for DHMS-7,9

is much lower (about an order of magnitude) than those of commercial Vectra-type thermotropic polymers [21]. This relatively low Region II viscosity reflects difference between the materials: the present sample has lower molecular weight and greater chain flexibility compared with those of commercial fully aromatic copolyesters.

While the flow curve (η vs. $\dot{\gamma}$) of DHMS-7,9 shows qualitative similarities to that of lyotropic HPC, the relationship between orientation and steady shear viscosity is quite different. Lyotropic HPC shows very weak orientation in Region I, an increase in orientation at the transition between Region I and Region II, nearly constant orientation in the plateau Region II, further increase in alignment when entering Region III and saturated orientation at high shear rate [23]. Although the lowest shear rate in our WAXS experiments did not extend far into Region I, there is no indication that Region I is accompanied by low orientation. Indeed, the orientation in Region I is strong and there is little change with shear rate from Region I to III (Figure 6a and Figure 8). Therefore, the qualitative understanding of the three-region flow curve in lyotropic HPC in terms of transition from a "piled-polydomain" structure in Region I to tumbling in Region II to wagging and then flow aligning in Region III cannot be invoked to explain the three-region flow curve observed in DHMS-7,9.

The relatively high and nearly constant orientation observed in steady shear is consistent with expectation for flow alignment in DHMS-7,9 of higher flexibility. The results on DHMS-7,9 provide a foundation to interpret rheological and orientational behavior of other mesogen-spacer type thermotropes, such as PSHQ-6,12, which shows similar shear orientation behavior [3] and may also be of flow aligning type. These observations suggest that mesogen-spacer type semiflexible thermotropes may generally be flow-aligning, as predicted by various molecular models. However, for more rod-like thermotropes such as HPC, the Doi model may be more appropriate to describe their rheological behavior; in fact, recent work by Huang and coworkers has provided indirect rheological evidence that thermotropic HPC might be a tumbling nematic [24].

The positive steady state values of N_1 over the entire shear rate range is a direct consequence of flow alignment, since a decrease of the local order parameter, which accounts for the occurrence of negative N_1 for lyotropic LCP in the vicinity of the transition from Region II to III, is not expected for flow aligning nematics. The positive value of N_1 for

semiflexible thermotropes is actually predicted by the nematic dumbbell model as a result of flow-aligning character [25].

A transition in the dependence of N_1 on shear rate occurs between Region II and III: in Region II, N_1 grows almost linearly with $\dot{\gamma}$, but in Region III, it increases more strongly with $\dot{\gamma}$ (Figure 3.3). This behavior is reminiscent of a prediction of the nematic dumbbell model, for which N_1 initially increases linearly with shear rate but then increases quadratically once the shear rate exceeds the inverse of the chain relaxation time [25]. An upper bound on the polymer chain relaxation time in the nematic phase is inferred to be around 15 s for DHMS-7,9 on the basis of the literature value of the self-diffusion coefficient D^* ($D^* \approx 3\times10^{-12}$ cm^2/s for $M_w \approx$ 29 000 g/mol) and an estimate of the completely extended chain contour length l ($l \approx$ D.P.$\times$19.6Å $\approx$650Å for this present sample). It is reported that a semiflexible thermotrope with a very similar chemical architecture to that of DHMS-7,9 has on average one hairpin per chain [26]. This leads to a polymer relaxation time a factor of 4 smaller, around 3-4 s. The inverse of this relaxation time (τ) roughly coincides with the shear rate where N_1 starts to deviate from the linear dependence on shear rate (Figure 3.3). The decrease in steady shear viscosity in Region III might also be interpreted in terms of the shear rate exceeding $1/\tau$ and therefore the change in conformation leads to the shear thinning in Region III.

3.7.2 Transient Shear Flow

Unlike the case of lyotropic LCP, whose transient shear stress and orientation response show multiple oscillations, the shear stress and orientation parameter of DHMS-7,9 only shows one single overshoot during various transient shear flows. Since multiple oscillations are signature of continuous director rotation in the shear flow, the absence of such oscillations in shear stress and orientation parameter provides another indirect evidence that DHMS-7,9 is flow-aligning. The observed behavior is quite similar to other thermotropes with high flexibility, such as PSHQ-6.12 [27], suggesting that PSHQ-6,12 is probably also a flow-aligning nematic.

3.7.3 Success and Limitation of Ericksen Polydomain Model

One attribute of Ericksen polydomain model is its ability to extract tumbling parameter from stress measurements. Using the viscosity predictions from nematic dumbbell model,

the steady state ratio of N_1/σ_{12} is predicted to depend only on λ, given by

$$\frac{N_1}{\sigma_{12}} = \frac{2}{\sqrt{\lambda^2 - 1}}. \tag{3.7}$$

This provides an alternative way to estimate the tumbling parameter, solely from steady shear rheological data.

As mentioned previously, the steady state rheological data of DHMS-7,9 roughly obey the predicted linear dependence of the shear stress and first normal stress differences on shear rate within region II (from 0.1 to 1 s^{-1} at 140°C). Thus, at steady state within this range, the ratio of N_1/σ_{12} is approximately constant, ranging from 2.4 to 2.8. This however corresponds to values of tumbling parameter between 1.23 and 1.30, which disagrees considerably with experimental data. First, such values of λ perform poorly in tracking orientation development (Figure 3.17). In addition, when this range of λ is used, the predicted ratio of overshoot peak to steady state stress lies between 1 and 2, much less than experimentally observed value of 4 to 6 (Figure 3.10a).

We conclude this whole section by pointing out some successes and limitations of Ericksen polydomain model. It is noteworthy that the same analysis did a much better job in describing rheology and shear orientation behavior of a PSHQ-6,12 [3]. Thus, it appears that Ericksen polydomain model, at least, captures the qualitative rheological features of flow-aligning thermotropes. The neglect of distortional elasticity, however, may be an important factor from which the discrepancy of stress predictions arise. Furthermore, difficulties are encountered in an attempt to determine the tumbling parameter solely from mechanical data, and the quantitative uncertainties of λ can be quite large.

3.8 Conclusions

The main chain thermotropic LCP (DHMS-7,9) shows a nice correlation between bulk rheological properties and shear orientation behavior. In steady shear, a three-region flow curve was observed, but no negative values of N_1 were measured. WAXS studies showed that molecules tend to orient only in the flow direction under steady shear. The orientation is strong in all three regions of the flow curve; in particular, orientation is not low in Region I (as would be expected in the "piled-polydomain" structure). Furthermore, there is almost

no enhancement of orientation when entering Region III. In transient shear flows, there is no multiple oscillations for shear stress and orientation parameter. All of these results are consistent with expectation of flow alignment for DHMS-7,9, which is in direct contrast with those of tumbling lyotropic LCPs.

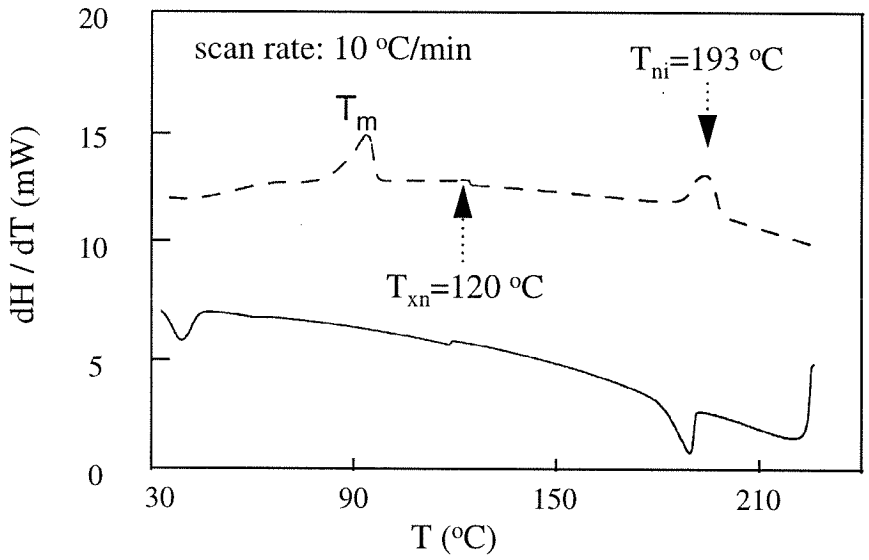

Figure 3.1: Differential scanning calorimetry traces for DHMS-7,9 (M_w= 28 440 g/mole). The temperature scanning rate was 10°C/min for both heating and cooling, and the amount of sample used was 10 mg.

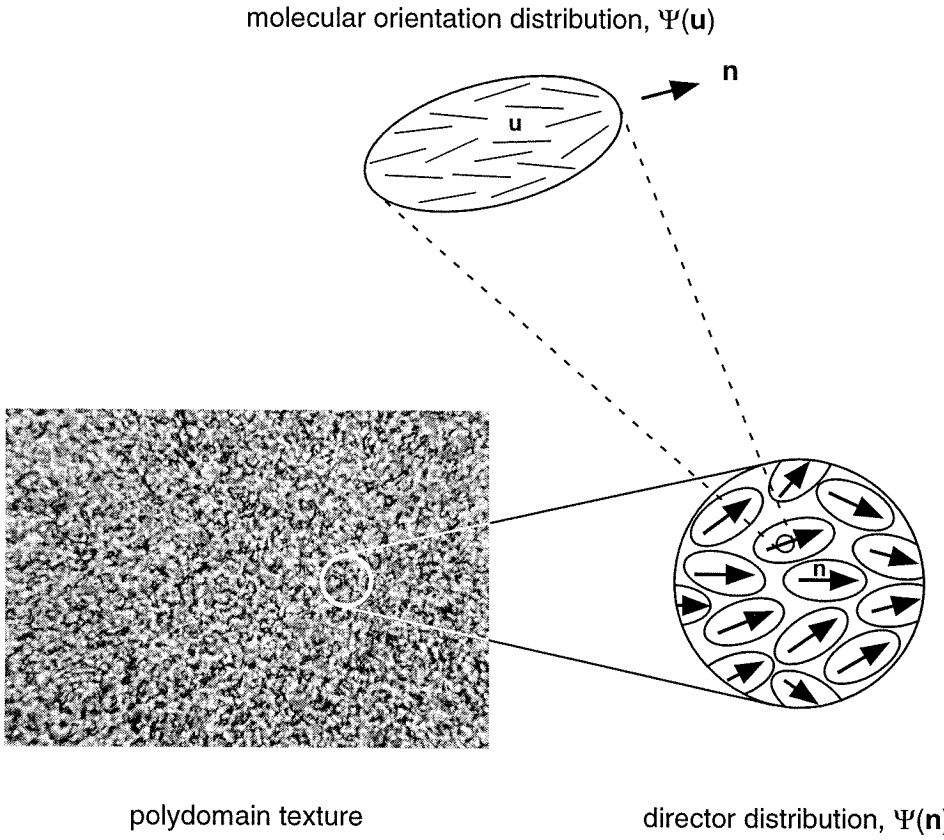

Figure 3.2: Illustration of molecular orientation distribution $\Psi(\mathbf{u})$ at the local molecular level and director orientation distribution at the macroscopic level.

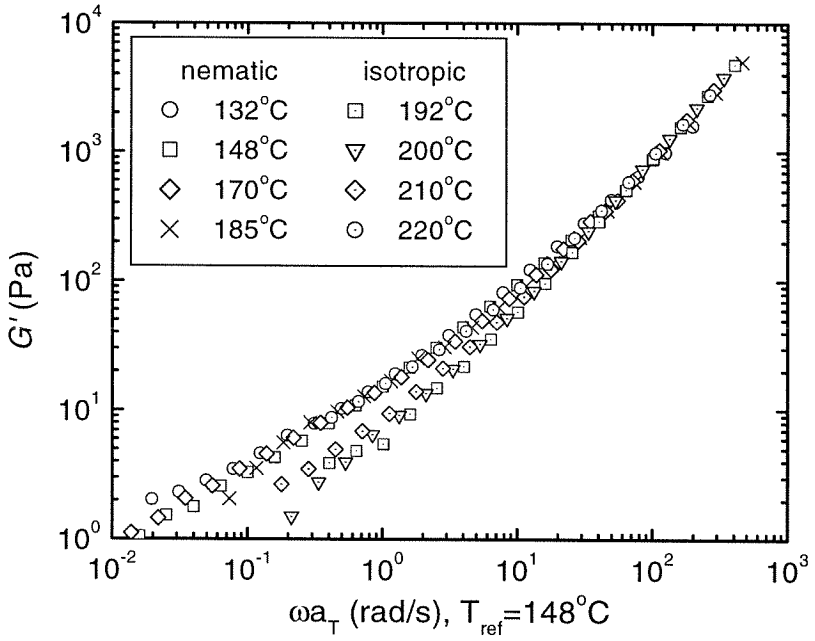

Figure 3.3: Dynamic storage modulus as a function of frequency in the isotropic and nematic phases. Measurements at different temperatures have been shifted along the frequency axis alone to achieve approximate superposition at high frequency (with nematic phase data at T=148°C for comparison).

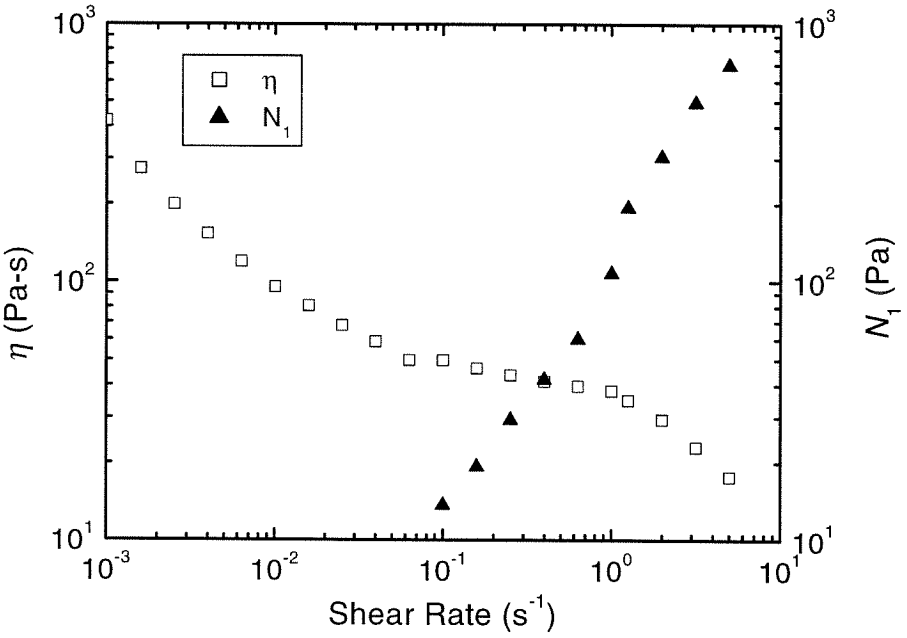

Figure 3.4: Steady shear viscosity (η) and first normal stress difference (N_1) as a function of shear rate at 140°C in the nematic phase.

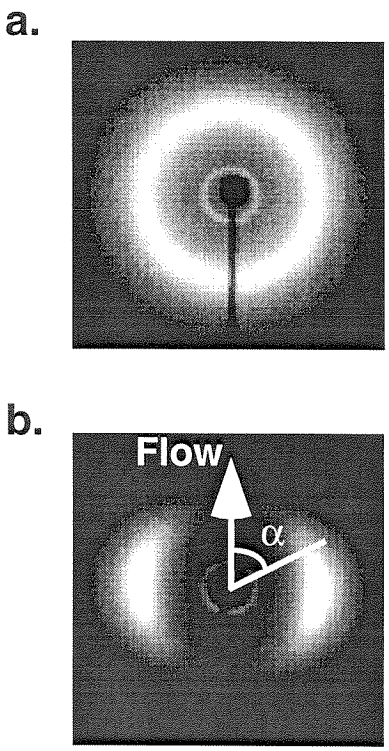

Figure 3.5: Typical scattering patterns from DHMS-7,9 (a) in the isotropic phase at 210° during shear at 0.1 s^{-1}, and (b) in the nematic phase at 150°C during shear at 3 s^{-1}. The flow direction is vertical and the azimuthal angle α is defined relative to the flow direction (scattering patterns from Ugaz and Burghardt).

a.

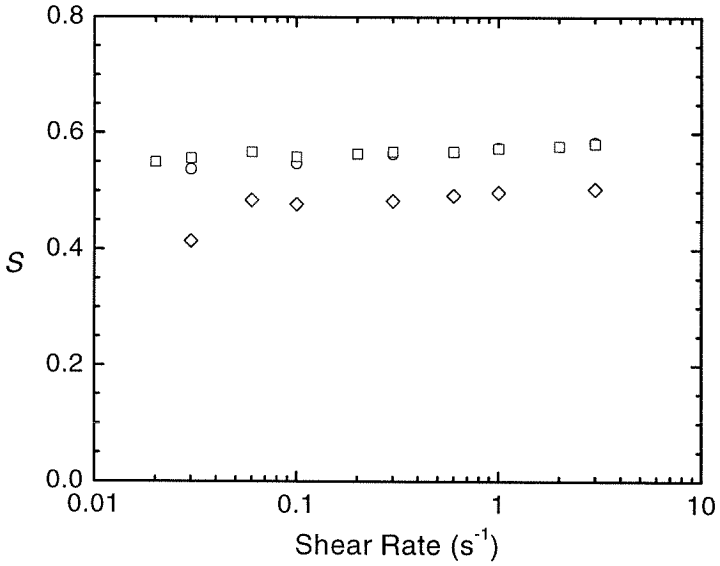

b.

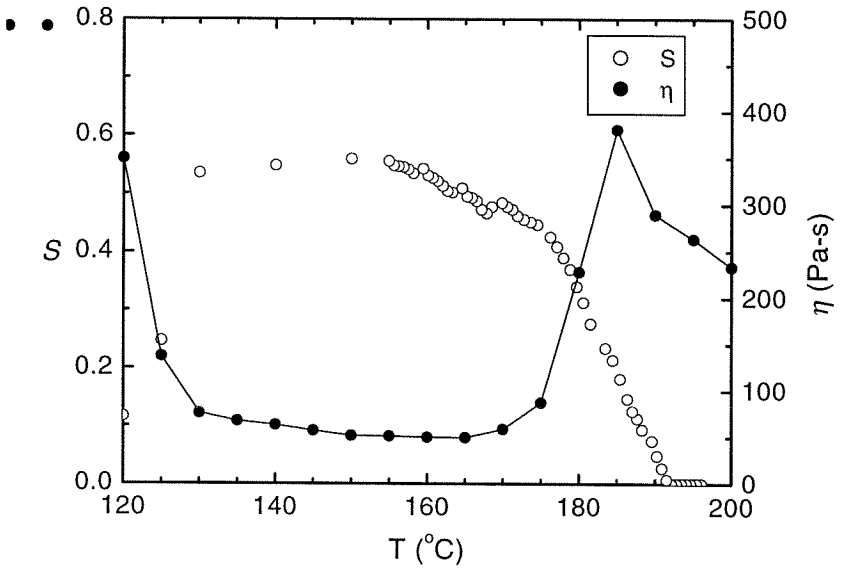

Figure 3.6: (a) Orientation parameter (S) as a function of shear rate in steady shear at 140°C [○], 150°C [□], and 170°C [◇]. (b) Orientation parameter [○] and viscosity [●] in steady shear flow at 0.1 s^{-1} as a function of temperature (data from Ugaz and Burghardt).

a.

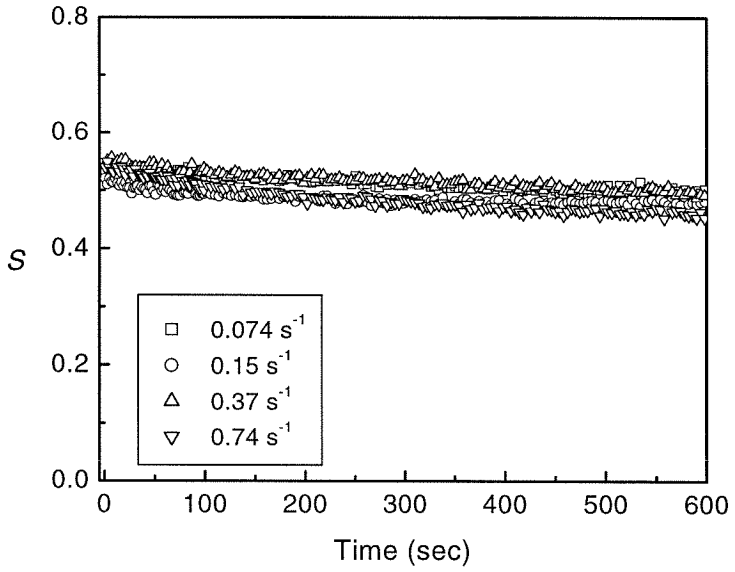

b.

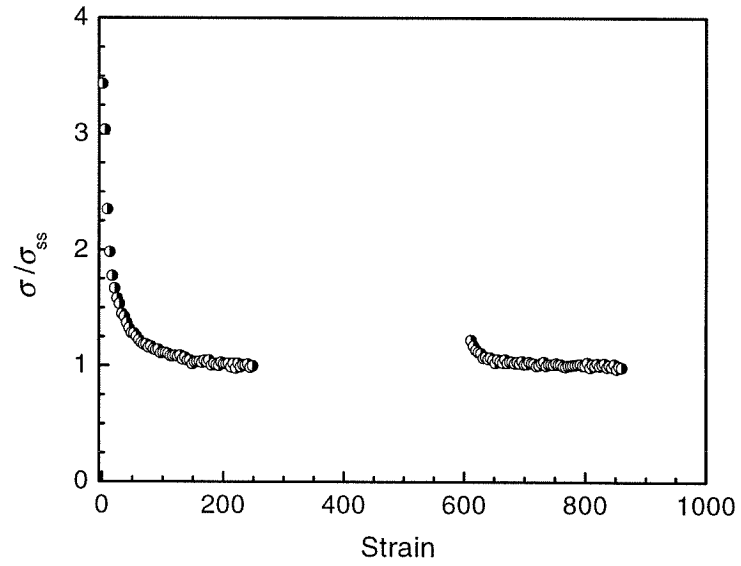

Figure 3.7: (a) Evolution of the orientation parameter as a function of time during relaxation from steady shear at 140°C at various shear rates (data from Ugaz and Burghardt). (b) Evolution of the normalized shear stress during interrupted flow at a shear rate of 0.1 s^{-1} in the nematic phase (140°C). The flow (at a shear rate of 0.1 s^{-1}) was interrupted for an hour ($\dot{\gamma} = 0$) after 250 strain units of shear deformation before flow resumption.

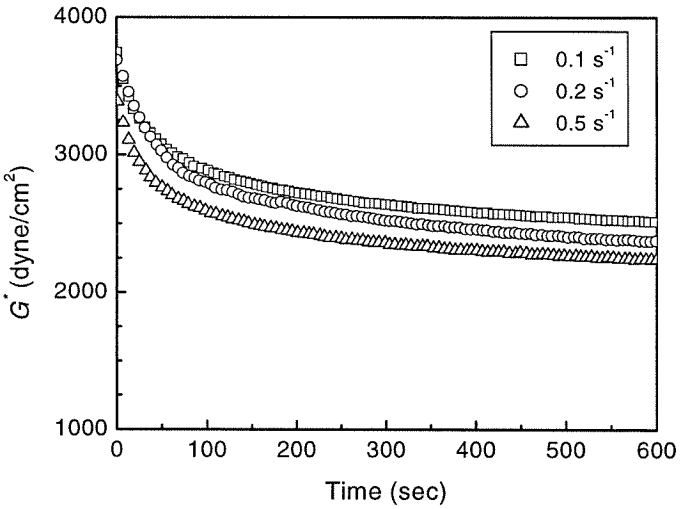

Figure 3.8: Evolution of the magnitude of dynamic modulus G^* as a function of time during relaxation from steady shear at three different shear rates in the nematic phase (140°C).

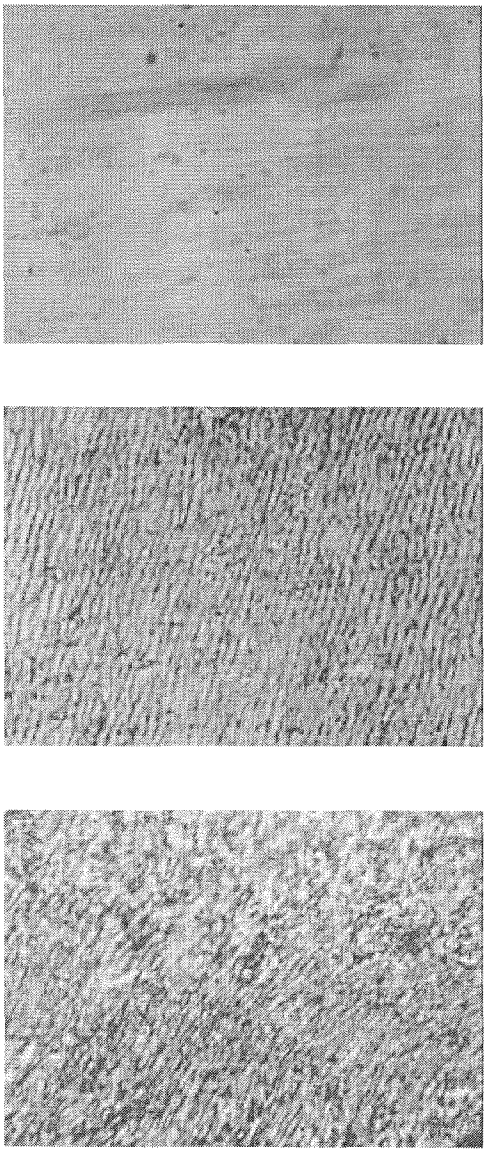

Figure 3.9: Evolution of the optical texture under cross polarizers during relaxation after steady shearing at the shear rate of 0.1 s^{-1} in the nematic phase (140°C). (a) Steady shear-induced texture; (b) After shear cessation for about 30 sec, alternate bright and dark bands appeared with bands perpendicular to the previous flow direction (horizontal); (c) After shear cessation for about 200 sec. The width of micrograph corresponds to 350 μm, and the two crossed polarizers are aligned at 0° and 90° to the flow direction, respectively.

a.

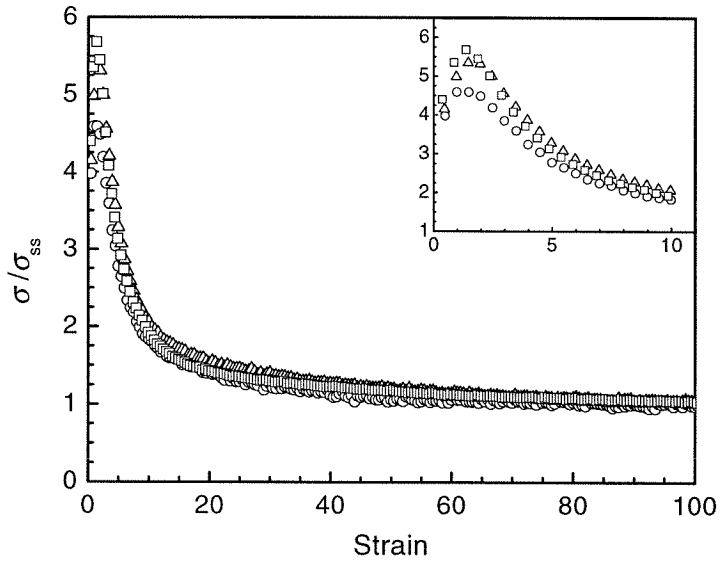

b.

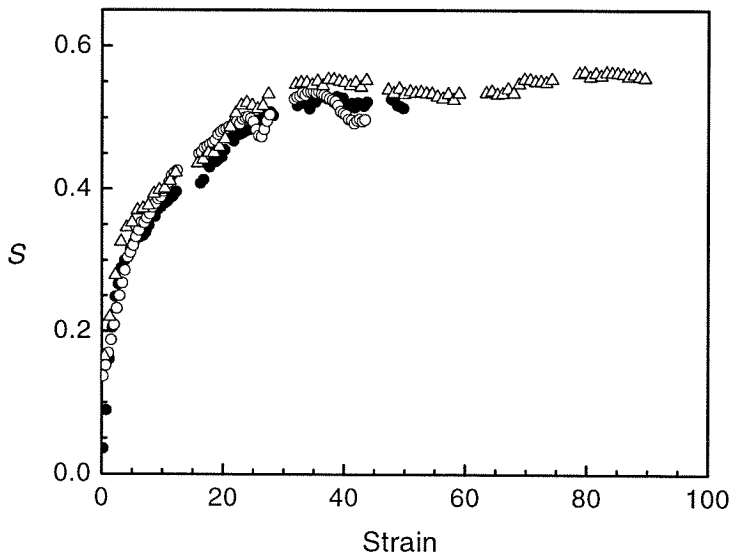

Figure 3.10: Stress and orientation response during flow inception in the nematic phase at 140°C. (a) Evolution of the normalized shear stress as a function of applied strain at three different shear rates: 0.1 s^{-1} [○], 0.3 s^{-1} [△] and 1.0 s^{-1} [□]. (b) Transient development of the orientation parameter as a function of applied strain at three different shear rates: 0.03 s^{-1} [●], 0.1 s^{-1} [○] and 0.3 s^{-1} [△] (data from Ugaz and Burghardt).

a.

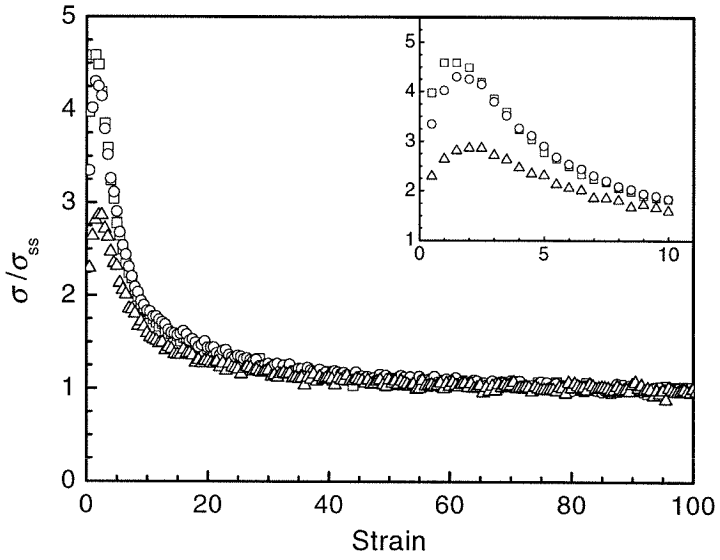

b.

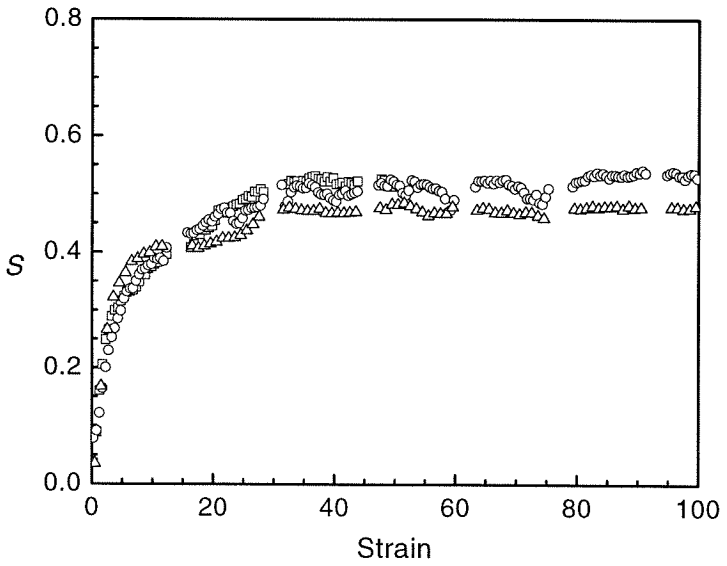

Figure 3.11: (a) Evolution of the normalized shear stress as a function of applied strain during flow start up at 0.1 s^{-1} at temperatures of 140°C [□], 150°C [○], and 170°C [△]. (b) The corresponding evolution of the orientation parameter as a function of applied strain during shear flow start up at 0.1 s^{-1} at temperatures of 140°C [□], 150°C [○], and 170°C [△] (data from Ugaz and Burghardt).

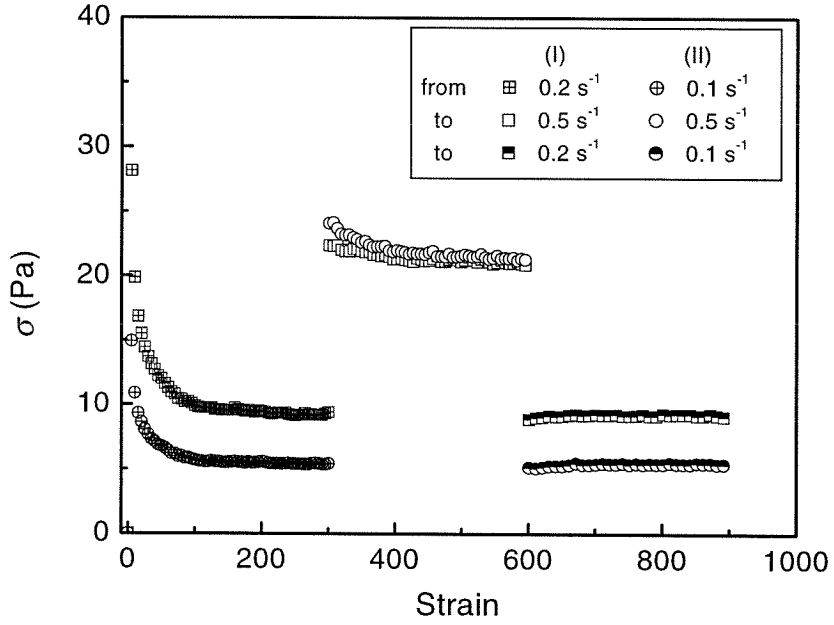

Figure 3.12: Evolution of the shear stress as a function of accumulative strain following a step change of shear rate from steady state in the nematic phase at 140°. Experiments for two series of step up-then-down in the shear rate, from $0.2 \rightarrow 0.5 \rightarrow 0.2$ s^{-1} and $0.1 \rightarrow 0.5 \rightarrow 0.1$ s^{-1} at 140°C, are shown here.

a.

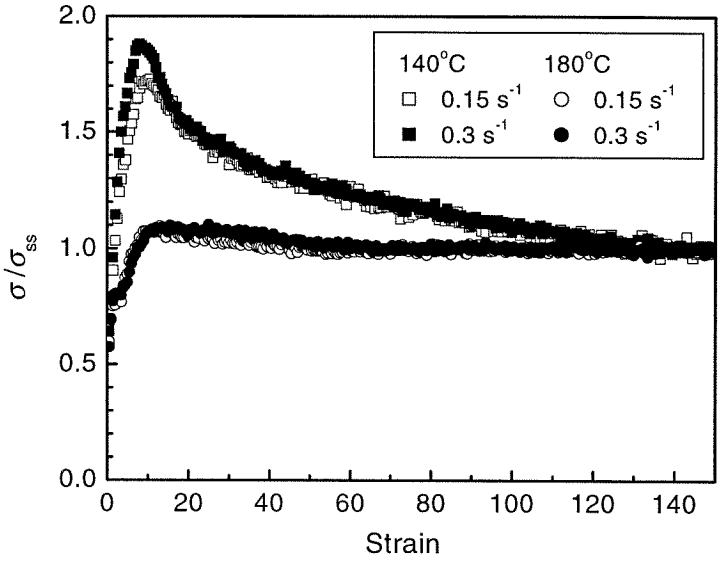

b.

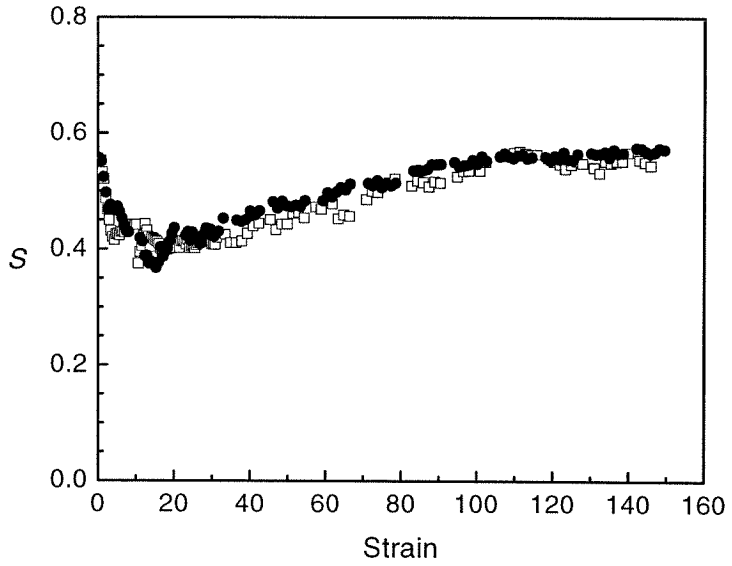

Figure 3.13: Transient response of the shear stress and orientation parameter S after flow reversal in the nematic phase. (a) Evolution of the normalized shear stress as a function of applied strain after flow reversal at 140°C and 180°C at shear rate of 0.15 s^{-1} and 0.3 s^{-1}; (b) Evolution of the corresponding orientation parameter as a function of applied strain after flow reversal at 140°C at shear rate of 0.15 s^{-1} [□] and 0.3 s^{-1} [•] (data from Ugaz and Burghardt).

a.

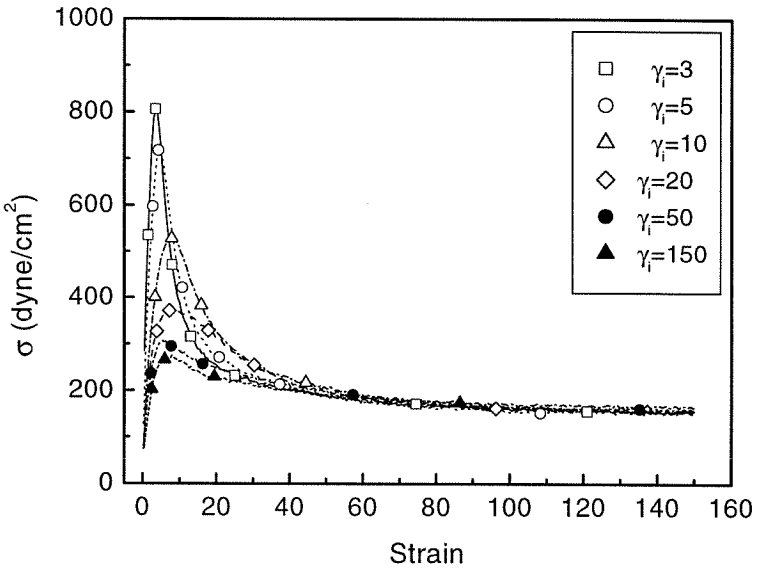

b.

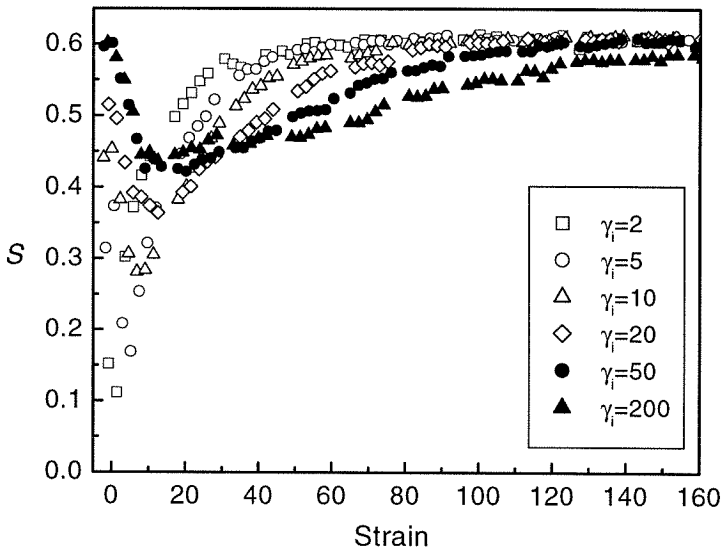

Figure 3.14: (a) Evolution of the normalized shear stress as a function of applied strain during interrupted shear flow reversal at 140°C and a shear rate of 0.3 s^{-1}, where the reversal is applied after preshearing for γ_i (=3, 5, 10, 20, 50, 150 s.u.). (b) Evolution of the corresponding orientation parameter as a function of applied strain during interrupted shear flow reversal at 140°C and a shear rate of 0.3 s^{-1} (data from Ugaz and Burghardt).

a.

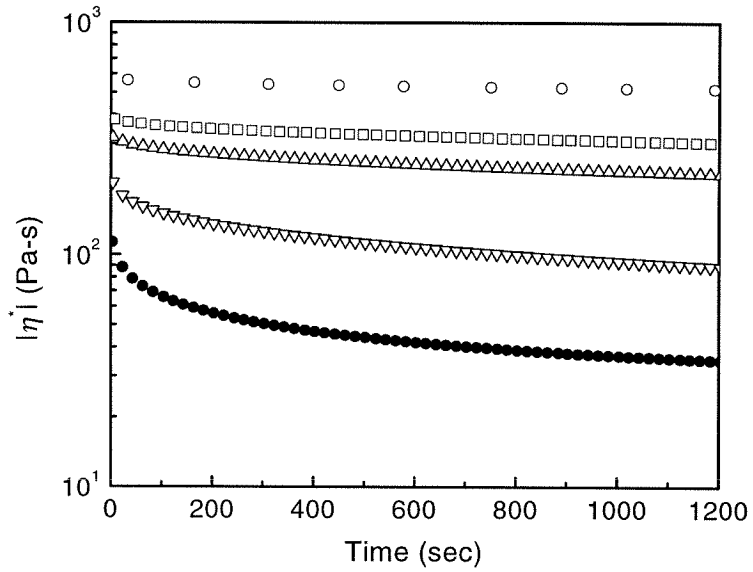

b.

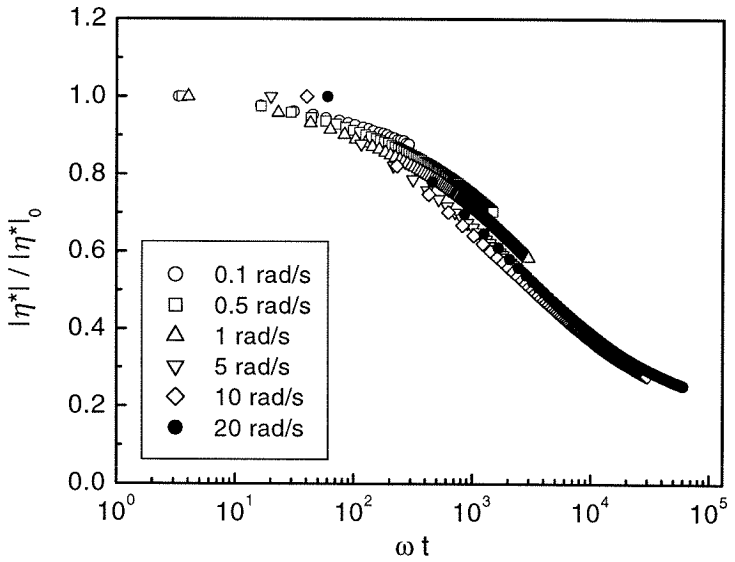

Figure 3.15: (a) Complex shear viscosity as a function of time during oscillatory shear alignment in the nematic phase at a strain of 100% and frequency of 0.1 rad/s [○], 0.5 rad/s [□], 1 rad/s [△], 5 rad/s [▽], and 20 rad/s [●]. (b)Evolution of the normalized complex shear viscosity as a function of effective strain ωt during oscillatory shear alignment at a strain of 100% and various frequencies, where $|\eta^*|_0$ represents the initial $|\eta^*|$ value of polydomain state at respective frequency.

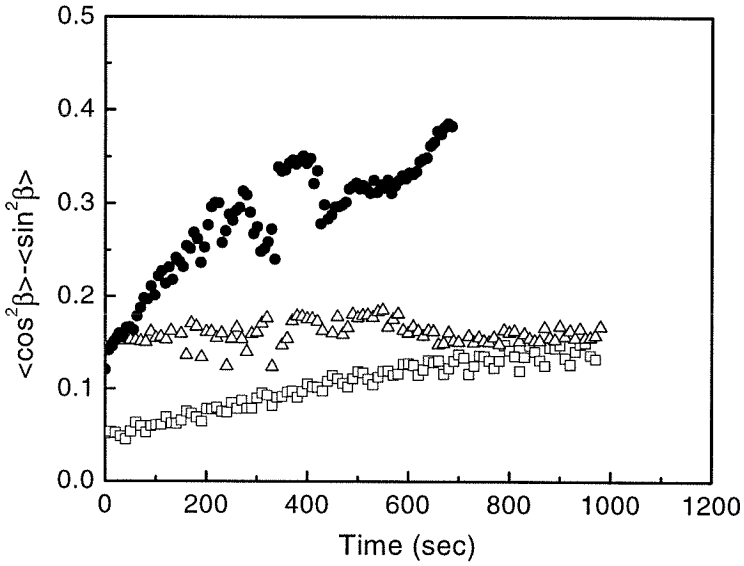

Figure 3.16: The evolution of orientation anisotropy as a function of time during oscillatory shear alignment at a strain of 50% and frequency of 0.5 rad/s [□], 1 rad/s [△], and 20 rad/s [●], where orientation anisotropy is defined by an average of $\langle \cos^2\beta \rangle - \langle \sin^2\beta \rangle$ weighted by an azimuthal intensity scan from the 2-D scattering pattern. Here, β is defined with respect to the flow direction (data from Vaish and Burghardt).

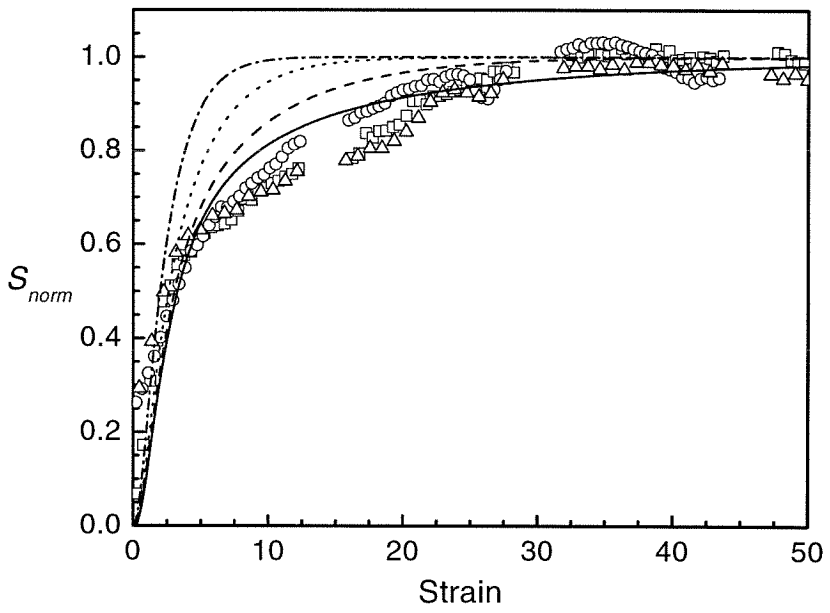

Figure 3.17: Predictions of the Ericksen polydomain model for the evolution of anisotropy in the 1-3 plane normalized by the steady state value during shear flow inception computed using λ values of 1.006 [——]. 1.035 [– – –], 1.167 [· · · ·], and 1.444 [–·–·–]. These predictions are compared with normalized X-ray orientation data for DHMS-7,9 in the nematic phase at 140°C at shear rates of 0.03 s^{-1} [□], 0.1 s^{-1} [○], and 0.3 s^{-1} [△] (data from Ugaz and Burghardt).

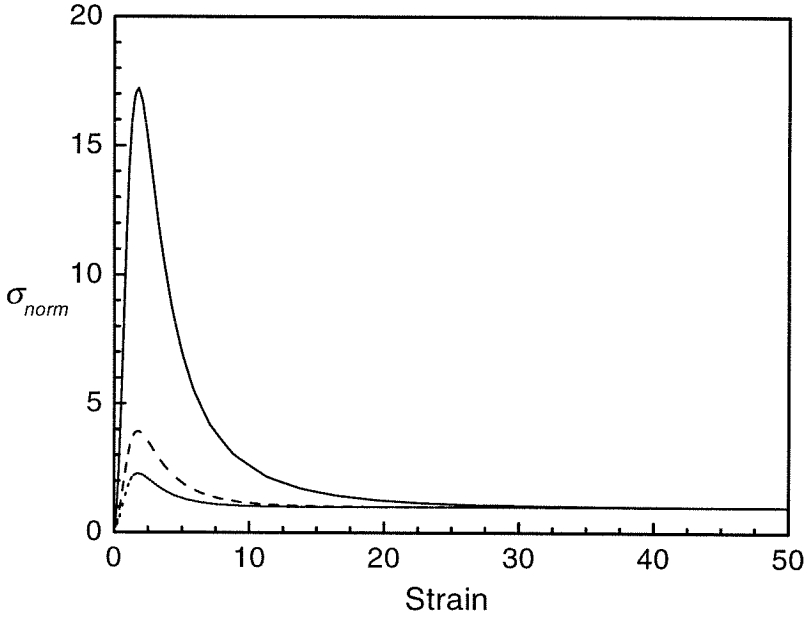

Figure 3.18: Predictions of the Ericksen polydomain model for the evolution of shear stress normalized by its steady state value as a function of applied strain during shear flow inception using λ values of 1.01 [——], 1.05 [– – –], and 1.10 [· · · · ·] (data from Ugaz and Burghardt).

Bibliography

[1] S. S. Kim and C. D. Han. *Macromolecules*, 26:6633, 1993.

[2] S. Chang and C. D. Han. *Macromolecules*, 30:1656, 1997.

[3] V. M. Ugaz and W. R. Burghardt. *Macromolecules,*, 31:8474, 1998.

[4] J. R. Gillmor, R. H. Colby, E. Hall, and C. K. Ober. *J. Rheol.*, 38:1623, 1994.

[5] E. Hall, C. K. Ober, E. J. Kramer, R. H. Colby, and J. R. Gillmor. *Macromolecules*, 26:3764, 1993.

[6] E.E. Hall, A. A. Robinson, S. G. McNames, C. K. Ober, and Y. S. Freidzon. *J. Mater. Sci.*, 30:2023, 1995.

[7] D. S. Kalika, David W. Giles, and M. M. Denn. *J. Rheol.*, 34:139, 1990.

[8] G. R. Mitchell and A. H. Windle. In D. C. Bassett, editor, *Developments in Crystalline Polymers*, volume 2. Elsevier, London, 1988.

[9] P. Driscoll, T. Masuda, and K. Fujiwara. *Macromolecules*, 24:1567, 1991.

[10] W. R. Burghardt and G. G. Fuller. *Macromolecules*, 24:2546, 1991.

[11] K. Hongladarom and W. R. Burghardt. *Macromolecules*, 26:785, 1993.

[12] K. Hongladarom, V. Secakusuma, and W. R. Burghardt. *J. Rheol.*, 38:1505, 1994.

[13] K. Hongladarom, V. M. Ugaz, D. K. Cinader, W. R. Burghardt, J. P. Quintana, B. S. Hsiao, M. D. Dadmun, W. A. Hamilton, and P. D. Butler. *Macromolecules*, 29:5346, 1996.

[14] M. D. Dadmun, S. C. Clingman, C. K. Ober, and A. I. Nakatani. *J. Polym. Sci., Part B: Polym. Phys.*, 36:3017, 1998.

[15] V. M. Ugaz. PhD thesis, Northwestern University, 1999.

[16] R. G. Larson and M. Doi. *J. Rheol.*, 35:539, 1991.

[17] D. K. Cinader and W. R. Burghardt. *Rheol. Acta*, page in press, 2000.

[18] V. M. Ugaz, W. R. Burghardt, and W. J. Zhou, and J. A. Kornfield. *J. Rheology*, page (submitted), 2000.

[19] A. N. Semenov. *Sov. Phys. J. E. T. P.*, 66:712, 1987.

[20] D. W. Giles and M. M. Denn. *J. Rheol.*, 38:617, 1994.

[21] H. C. Langelaan and A. D. Gotsis. *J. Rheol.*, 40:107, 1996.

[22] D. Acierno and A. A. Collyer. *Rheology and processing of Liquid Crystal Polymers.* Chapman & Hall, New York, 1996.

[23] W. R. Burghardt. *Macromol. Chem. Phys.*, 199:471, 1998.

[24] C. M. Huang, J. J. Magda, and R. G. Larson. *J. Rheol.*, 43:31, 1999.

[25] P. L. Maffettone and G. Marrucci. *J. Rheol.*, 36:1547, 1992.

[26] F. Hardouin, G. Sigaud, M. F. Achard, A. Brulet, J. P. Cotton, D. Y. Yoon, V. Percec, and M. Kawasumi. *Macromolecules*, 28:5427, 1995.

[27] S. S. Kim and C. D. Han. *J. Rheol.*, 37:847, 1993.

Chapter 4 Effect of Molecular Weight on Viscous Properties of a Main Chain LCP

4.1 Introduction

With increasing chain flexibility, the dynamics of LCPs will deviate from theoretical descriptions of the Doi model which assumes the molecules are rigid rods [1]. In rod-like lyotropes, such as poly-γ-benzyl glutamate (PBG), a crossover from rod-like to semiflexible character occurs at a characteristic length-to-diameter ratio $L/d \approx 50$ [2]. We anticipate that a similar kind of crossover transition may also occur in thermotropic LCPs. In particular, semiflexible mesogen-spacer type thermotropes may behave effectively like rigid rods in the low molecular weight limit, but show effects of chain flexibility as molecular weight increases.

Unfortunately, even basic trends of viscosity with molecular weight and chain stiffness have rarely been measured for thermotropic LCPs. The existing data show system-specific dependence on molecular weight. A large variation in the molecular weight dependence of the shear viscosity has been reported for different thermotropic LCPs, with power-law exponents ranging from 3.5 to 6 [3, 4, 5]. Similar difficulties are encountered in the molecular weight dependence of the rotational viscosity (γ_1) with power-law exponents reported to lie between 2 to 7 [6, 7, 8, 9]. One thermotropic system AZA9 (Figure 1.5g) indeed was inferred to exhibit a rigid-to-semiflexible transition based on the observation that the rotational viscosity has a much weaker molecular weight dependence above a characteristic molecular weight than below it [6]. However, in thermotropes consisting of the same mesogen and spacer, a simple change in the length of the alkyl spacer from 10 -CH_2 in DDA9 [7] to 7 -CH_2 in AZA9 [6] causes a qualitatively different molecular weight dependence of γ_1. The rotational viscosity of DDA9 was found to vary as M_n^6 over the molecular weight range 2250-11300 g/mol [7], while for AZA9, the increase of γ_1 with the molecular weight became progressively weaker with increasing M_n from $\gamma_1 \propto M^7$ for $M_n < 5000$ g/mol to $\gamma_1 \propto M^{4.7}$ for $M_n > 5000$ g/mol [6].

Several reasons may account for the significant disparity in molecular weight dependence of the viscosity coefficients between different thermotropic systems. Some of the explanation may lie in the differences in molecular rigidity among various systems: some thermotropic LCPs have only rigid units in their main chain [5], others have alternating mesogens and flexible spacers [3, 4]. One would not expect rigid rod-like behavior to extend to mesogen-spacer type polymers. Nevertheless, some studies have found extremely nonlinear molecular weight dependence of viscosities—one of the hallmarks of rod-like LCPs—in mesogen-spacer systems [3, 4, 7]. However, the remarkably strong molecular weight dependence observed in some mesogen-spacer systems may be due to the presence of an additional phase or higher order structure (e.g., cybotactic clusters [10]). Additional complications may also contribute to the disparate results in the literature: the molecular weight dependence of the glass transition temperature [11], molecular weight dependence of the order parameter, potential effects of polydispersity (e.g., nematic-nematic phase separation between short and long polymer chains [12]), and the many experimental difficulties in working with the commercial rod-like thermotropes as we mentioned in the previous chapters. Finally, different viscous coefficients might have different molecular weight dependencies, accounting for some of the disparities in findings between studies that focus on different viscosities in examining the effects of chain length. Resolving these issues requires further work on model thermotropic LCPs, employing comprehensive characterization of their phase behavior, liquid crystalline structure and rheology.

This has motivated us to study a number of viscosity coefficients on a thoroughly characterized model thermotropic LCP (DHMS-7,9) to establish the effect of molecular weight on dynamic behavior. Four different measures of the viscosity are used: 1) The characteristic director reorientation time (τ_1) of a pseudo-monodomain was used as a relative measure of the rotational viscosity (γ_1); 2) the steady shear viscosity η was measured for polydomain samples; 3) the complex shear viscosity was measured for polydomain samples ($|\eta^*|_{poly}$); and 4) the complex shear viscosity was measured for shear oriented samples ($|\eta^*|_{oriented}$). The conformational elasticity of polymer chain should have negligible effect on the complex shear viscosity because of the low oscillatory strain used (within the linear viscoelastic region). This is not true for steady shear viscosity at high deformation rates ($De > 1$) due to considerable deviations from the equilibrium chain conformation. To provide insight into

the potential role of chain flexibility in the rheological behavior, we also characterized the intrinsic viscosity of DHMS-7,9 when dissolved in an isotropic solvent.

This approach reveals important effect of chain length on the dynamical behavior of LCPs. As was the case of AZA9, the rotational viscosity of DHMS-7,9 shows weaker molecular weight dependence above a characteristic molecular weight. In addition, three different measures of the shear viscosity (η, $|\eta^*|_{poly}$ and $|\eta^*|_{oriented}$) of DHMS-7,9 show a similar transition in molecular weight dependence, providing a strong case that crossover from rod-like to semiflexible character occurs in DHMS-7,9. The crossover occurs at a contour length $L \approx 20$ nm ($M_w^c \approx 7\ 000$ g/mol). In view of the intrinsic viscosity results, which indicate that the persistence length of DHMS-7,9 in dilute solution in an isotropic solvent is only about 1.8 nm, the much longer chain length associated with the crossover suggests that polymers in the melt are elongated due to the nematic potential.

4.2 Experimental Section

4.2.1 Materials and Characterization

We synthesized DHMS-7,9 with several different molecular weights: polystyrene-equivalent M_w ranging from 5 000 g/mol to 65 000 g/mol (Table 4.1) for this study. The actual M_w determined from light scattering is slightly higher ($\sim$ 12.5%) than their respective polystyrene-equivalent value, as described in the Appendix of this chapter. In the following, the polystyrene-equivalent molecular weight is still used throughout this study to be consistent with previous literature [13, 14].

Differential scanning calorimetry (Perkin-Elmer DSC7) was used to determine phase transitions using a rate of 10°C/min during both heating and cooling under an Argon purge. Thermal transitions and texture behavior were also examined in a polarizing light microscope (Zeiss Universal Pol-Microscope equipped with Mettler FP-80 hot stage). It is noteworthy that the glass transition temperature lies between 12°C and 23°C for all the different molecular weight DHMS-7,9 polymers and is far below the temperature (135°) at which viscosity measurements were made. Thus, the present results are not complicated by the M_w dependence of the glass transition.

The persistence length of DHMS-7,9 in an isotropic solvent (1,2-dichlorobenzene) was inferred from the M_w dependence of the intrinsic viscosity ($[\eta]$). To ensure good solubility,

all the viscosity measurements were performed at 33.5°. A Rheometrics RFS-II rheometer was used with standard Couette geometry at a shear rate of 50 s^{-1}. This shear rate is within the Newtonian range for all the solutions. A series of dilute solution viscosity measurements was extrapolated to a "zero-concentration viscosity" to determine $[\eta]$ for each molecular weight. Analysis of the intrinsic viscosity data is based on the worm-like chain model [15], which requires the value of the partial specific volume ($\overline{v}$) of the polymer. For DHMS-7,9, $\overline{v}$ is determined to be 0.896 ml/g (within ± 5% error) from density measurements.

4.2.2 Magnetic Alignment and Director Reorientation

An *in situ* study of director reorientation kinetics was performed using magnetic alignment and optical determination of the director orientation. A Varian 100-XL electromagnet set to a magnetic field strength of 2 Tesla was used for all experiments. The transmitted light intensity through crossed and parallel polarizers ($I_\perp$ and $I_{||}$, respectively) was recorded during the magnetic alignment and reorientation processes (using polarizers at ±45° to the magnetic field and a He-Ne laser, $\lambda = 632.8$ nm).

The sample is sandwiched between two CaF_2 windows with a gap thickness of 75 μm. This sample cell is placed in an aluminum holder, which acts as a heat bath. The sample is heated using a mica-heater (Minco, Inc.) with temperature controlled to ±0.2°C (Omega CN-76000 process controller). The aluminum holder is affixed at the end of a phenolic tube via a hollow snug-fit Teflon^{TM} spindle providing a clear line of sight through the sample. The phenolic tube could be manually rotated about the axis of light propagation. An electrical trigger was used to mark the time of sample rotation. Reorientation experiments were performed using rotation through an angle of 30° to avoid complications associated with backflow at large reorientation angles (>45°).

The sample was first heated to the isotropic state (T_{ni} + 10°C) for 20 minutes, and then slowly cooled down to the nematic phase at an approximate rate of 1°C/min. The measurement temperature was chosen to be 135°C, well within the nematic phase (and far away from the glass transition) for all the samples. Depending on M_w, an annealing time of hours to days at 135°C was needed to prepare a pseudo-monodomain sample for reorientation experiments; the saturation of $I_\perp$ served as a criterion for the formation of a pseudo-monodomain.

4.2.3 Rheological Measurements

Both the steady shear viscosity (η) and complex shear viscosity ($|\eta^*|$) were measured on a Rheometrics ARES rheometer (equipped with 2000 g-cm transducer). The sample was heated using a forced convection oven (stability to $\pm$ 0.2°C) under continuous dry nitrogen purge. The cone-and-plate geometry (diameter=25 mm, cone angle=0.1 rad) was used in measuring η and $|\eta^*|$ for high M_w samples ($M_w \geq$ 16 500 g/mol), and a parallel-plate of large size (diameter=50 mm, gap=1 mm) was used for low M_w samples due to their small viscosity.

Our rheological tests were conducted on molded samples from solvent casting film. This is because polymer samples are initially in fibrillar form and very porous, and the direct melt compression molding could trap many air bubbles. The polymer films were cast from solution in dichloromethane (EM Science), and further dried in a vacuum oven before molding into 25 mm and 50 mm diameter disks with 1 mm thickness. Care was taken to ensure the samples contain as few air bubbles as possible.

To obtain η and $|\eta^*|_{poly}$ for a representative polydomain state, the sample was thermally cleared to erase any prior thermal and flow history by heating to the isotropic state ($\approx T_{ni}$+10°C) and then cooling back to the nematic phase. An additional 20 minutes was allowed for thermal equilibration before commencing flow experiments. This time is also necessary for tool fixtures to reach thermal equilibrium to ensure the sample with right gap thickness.

The complex shear viscosity of shear oriented samples ($|\eta^*|_{oriented}$) was obtained using samples that were presheared to their steady state at a shear rate of 0.2 s^{-1} for 1250 s in the nematic phase (135°C), followed by an immediate dynamic frequency sweep descending from 100-1 rad/s. It took approximately 180 s to complete the frequency sweep measurements. For DHMS-7,9 with molecular weight higher than 16 500 g/mol, this time is short compared to their slow relaxation (>30 min for M_w = 28 440 g/mol); however, for low molecular weight samples, slight relaxation may still occur.

4.3 Results

4.3.1 Molecular Flexibility Inferred from Intrinsic Viscosity

Intrinsic viscosity of DHMS-7,9 in 1,2-dichlorobenzene shows a very weak dependence on molecular weight (Figure 4.1). A plot of $[\eta]$ vs. $\log M_w$ shows the following relationship ($[\eta]$ in ml/g, M_w in g/mol):

$$[\eta] = 5.02 \times 10^{-2} M_w^{0.70} \tag{4.1}$$

The Mark-Houwink exponent of 0.70 is much lower than theoretical expectation for a rod-like chain and falls within the range expected for a flexible chain, where the Mark-Houwink exponent is between 0.5 and 0.8, depending on solvent quality. This indicates that DHMS-7,9 has significant flexibility due to the incorporation of long alkyl spacers between mesogens.

We are able to estimate the persistence length of DHMS-7,9 from $[\eta]$ following Bohdanecky's treatment for worm-like chains [16]. The intrinsic viscosity of a worm-like chain approaches the behavior of flexible chains in the limit of high M and the limit of rods for low M. The crossover behavior between these is described by:

$$(M^2/[\eta])^{1/3} = A_\eta + B_\eta M^{1/2}, \tag{4.2}$$

where

$$A_\eta = A_0 M_L \Phi_0^{-1/3}, \tag{4.3}$$

$$B_\eta = B_0 \Phi_0^{-1/3} (\left\langle R_0^2 \right\rangle / M)_\infty^{-1/2}, \tag{4.4}$$

and

$$A_0 = 0.46 - 0.53 \log(d/2q), \tag{4.5}$$

$$B_0 = 1.00 - 0.0367 \log(d/2q), \tag{4.6}$$

$$(\left\langle R_0^2 \right\rangle / M)_\infty = 2q/M. \tag{4.7}$$

Here, M is the relative molar mass (e.g., M_w), M_L is defined as the relative molecular mass per unit contour length ($M_L = M/L$, L is the chain contour length), Φ_0 is Flory's hydrodynamic constant equal to 2.86×10^{23}, $\langle R_0^2 \rangle$ is the mean-square end-to-end distance of

the chain, d is the effective hydrodynamic diameter, and q is the persistence length of the polymer chain.

Following Bohdanecky's suggestion [16], we estimated the value of $d/2q$ close to 0.15 by assuming that the volume occupied by 1 g of the wormlike polymer is equal to the partial specific volume of the polymer molecules (i.e., $\overline{v} = (\pi N_A/4)(d^2/M_L)$, N_A is Avogadro number). Using this value, we can determine A_0 and B_0 from Eqn 4.5 and 4.6, followed by a linear fit of $(M_w^2/[\eta])^{1/3}$ vs. $M_w^{1/2}$ (Figure 4.2) to extract d and q. The persistence length was determined to be $q \approx 17.7 \pm 2.3$ Å and chain diameter $d \approx 5.3 \pm 0.6$ Å. In light of the length of one mesogen-spacer repeating unit (≈19.6 Å) [13], the surprisingly short persistence length can be explained only by assuming that the polymer chain adopts an almost completely random coil conformation in the isotropic solvent. The considerable flexibility of DHMS-7,9 in the solvent is consistent with light scattering determination of absolute molecular weight, showing only 12.5% larger in magnitude for the absolute M_w than corresponding polystyrene-equivalent value.

The random coil conformation in an isotropic solvent cannot be generalized to the situation where the polymer chain is subject to nematic interactions, such as in a nematic solvent or in the melt state. In either case, a larger persistence length is expected due to the influence of nematic potential. We examined the possibility of measuring the intrinsic viscosity of DHMS-7,9 in a nematic solvent; unfortunately, no available small molecule nematic was found to dissolve DHMS-7,9.

4.3.2 Effect of Chain Length on Rotational Viscosity

For a monodomain LCP sample with its director at an angle θ relative to an applied magnetic field ($\vec{H}$), the balance between viscous and magnetic torques leads to the following relation:

$$\gamma_1 \frac{d\theta}{dt} + \frac{1}{2}\Delta\chi_a H^2 \sin 2\theta = 0, \tag{4.8}$$

where $\Delta\chi_a$ is the anisotropy of the diamagnetic susceptibility per unit volume of the polymer. The solution of this equation is

$$\tan\theta(t) = \tan\theta_0 \; e^{-t/\tau_1}, \tag{4.9}$$

where θ_0 is the initial angle between the monodomain director and magnetic field ($\vec{H}$), and

$$\tau_1 = \frac{\gamma_1}{\Delta\chi_a H^2} \tag{4.10}$$

is a characteristic time for director reorientation.

It has been reported that $\Delta\chi_a$ is on the order of 1.0×10^{-8} cgs for mesogen-spacer type thermotropic LCPs [17]. Since $\Delta\chi_a$ varies little with molecular weight for fixed repeat unit structure, we determine the molecular weight dependence of the rotational viscosity of DHMS-7,9 using Eq. 4.10 with this value of $\Delta\chi_a$.

When the optical axis (collinear with the director) of a monodomain sample is at an angle of θ with respect to $\vec{H}$, and the sample is placed between crossed polarizers at $\pm 45°$ to $\vec{H}$, the transmitted light intensity is

$$I_\perp = AI_0 \sin^2(\frac{\pi\Delta nh}{\lambda})\cos^2 2\theta, \tag{4.11}$$

$$I_{||} = AI_0[1 - \sin^2(\frac{\pi\Delta nh}{\lambda})\cos^2 2\theta], \tag{4.12}$$

where A is a factor that takes into account attenuation of light due to absorption and scattering, Δn is the effective birefringence and h is the sample thickness. From Eq. 4.11 and Eq. 4.12, we obtain

$$\sin^2(\frac{\pi\Delta nh}{\lambda})\cos^2 2\theta = \frac{I_\perp}{I_\perp + I_{||}} \equiv \rho(t). \tag{4.13}$$

Taking $t = 0$ as the fully aligned state immediately after rotating the sample to $\theta(t = 0) = \theta_0$,

$$\cos 2\theta = \cos 2\theta_0 \sqrt{\frac{\rho}{\rho(t = 0)}}. \tag{4.14}$$

A typical reorientation curve of $\tan\theta$ vs. t shows a roughly exponential decay (Figure 4.3a), but the fit is certainly not satisfactory in comparison to small molecule LCs, whose reorientation kinetics almost perfectly follow Eq. 4.9 [18]. Similar studies on other polymeric systems also did not find single exponential reorientation kinetics [8, 19]. This discrepancy is probably due to the poor quality of monodomain formation for main-chain thermotropic LCPs. In the case of low molecular weight DHMS-7,9 ($M_w \leq 11\,000$ g/mol), disclination walls of thickness ~ 1.5 μm appear between domains of opposite director orien-

tation after reorientation (Figure 4.3b). These walls are parallel to the magnetic field and may persist even after hours of annealing inside the magnetic field. For higher molecular weight samples ($M_w \geq 16\ 500$ g/mol), we have never been able to achieve high quality monodomains that show a conoscopic interference figure.

A possible decoupling of mesogen orientation and polymer chain conformation can cause further complications to the kinetics of director reorientation, particularly, if the longest relaxation time τ_R of the polymer chain is comparable to the characteristic time τ_{nem} for the mesogen reorientation, a double-exponential reorientation kinetics is expected as initially suggested for side-group LCPs [20]. For DHMS-7,9, an attempt to fit experimental data with double exponential relaxation showed little improvement and is physically meaningless. Nevertheless, values of τ_1 extracted using the best fit of single-exponential showed good reproducibility within 10% relative error. Therefore, the uncertainty in the precise shape of the relaxation function should not change the molecular weight dependence of the inferred τ_1.

The molecular weight dependence of the rotational viscosity cannot be described by a single power-law (Figure 4.4). There exists a characteristic molecular weight, M_w^c ($\sim$ 7 000 g/mol determined from non-linear curve fitting to match asymptotic slopes at both low and high molecular weights), below which γ_1 has a slightly non-linear (> 2) dependence on M_w, and above which $\gamma_1 \propto M_w^{1.2}$. The exponent at low molecular weight (> 2) lies between that of semi-rigid chain and rigid rod, the former predicted to have a quadratic dependence of γ_1 on molecular weight [21, 22], and the latter with power law exponent of 6 on molecular weight [23]. The weaker M_w-dependence at high molecular weights is close to theoretical predictions for flexible chains, suggesting increased chain flexibility of DHMS-7,9 at high molecular weights.

4.3.3 Effect of Chain Length on Shear Viscosity

Shear Rate Dependence

The shape of the flow curve (i.e., η vs. $\dot{\gamma}$) changes with molecular weight (Figure 4.5a). A completely Newtonian behavior was observed at low M_w ($\leq$ 11 000 g/mol). At intermediate M_w (DHMS-16.5K), η showed Newtonian behavior at low shear rate and shear thinning at high shear rate. The flow curve becomes more complicated at high molecular

weight (DHMS-28K) with a very weak Newtonian region at intermediate shear rate, and shear thinning at both low and high shear rate, reminiscent of the three-region flow curves observed in other LCPs [24, 25]. At the highest M_w (DHMS-65K), η showed shear thinning over the entire range of shear rates we studied (Figure 4.5a).

The complex shear viscosity of polydomain samples ($|\eta^*|_{poly}$) showed a qualitatively similar dependence on frequency as η on shear rate (Figure 4.6a), while the complex shear viscosity of shear oriented samples ($|\eta^*|_{oriented}$) is lower in magnitude than that of polydomain samples and the flow curves are relatively featureless (Figure 4.6b). For DHMS-5K, DHMS-7.6K, and DHMS-11K, $|\eta^*|_{oriented}$ displays a roughly Newtonian behavior; whereas for DHMS-16.5K and above, only shear thinning was observed over the entire frequency range 1-100 rad/s (Figure 4.6b).

It is evident that shear viscosity measurements (η, $|\eta^*|_{poly}$ and $|\eta^*|_{oriented}$) depend strongly on the sample's shear history. For short chains ($M_w \leq 11\ 000$ g/mol), only the relative value of the viscosity changes; while at intermediate and high molecular weights, the shape of $|\eta^*|\,(\omega)$ and $\eta(\dot{\gamma})$, as well as their magnitudes, change with flow history (Figure 4.5 and 4.6).

Temperature Dependence

The complex shear viscosity of the polydomain sample exhibits a qualitatively similar temperature dependence for different molecular weights (Figure 4.7a). With increasing temperature, a dramatic drop in viscosity is apparent at the transition from an unidentified low temperature mesophase, Phase X, to the nematic phase T_{xn}; the x-phase shows some rheological similarities to layered fluids [13]. The apparent viscosity in the nematic phase varies weakly with temperature, showing slight decrease until the entrance of the nematic-isotropic biphase region. The apparent viscosity decreases again with temperature when the sample is fully isotropic. The wide nematic-isotropic biphase region is due to polydispersity. The phase transitions as indicated from an abrupt change of the viscosity are in accord with those determined by DSC and hot stage microscopy (Table 4.1).

The complex shear viscosity of the nematic phase can be reasonably well described by Arrhenius relations, i.e., $|\eta^*|_{poly} = A\exp(-E_a/T)$. The apparent flow activation energy is around 34 kJ/mol, and roughly independent of M_w (Figure 4.7b). This justifies use of the viscosity value at a single temperature that lies well within the nematic range for all the

samples (at 135°C in our case) to compare their molecular weight dependence. The wide nematic range of DHMS-7,9 makes it possible to directly measure the viscosity at the same temperature for all samples.

Molecular Weight Dependence

Like the rotational viscosity, all shear viscosity showed a transition in their molecular weight dependence at the nearly same molecular weight ($\sim$ 7 000 g/mol). The viscosity in the pseudo-Newtonian region was used for comparison. When the shear viscosity (at $\dot{\gamma} = 1$ s^{-1} for η and $\omega = 1$ rad/s for $|\eta^*|_{poly}$ and $|\eta^*|_{oriented}$) were plotted versus M_w, a strong molecular weight dependence was observed at low molecular weight limit and a much weaker dependence as molecular weight increases (Figure 4.8). Three trend lines were drawn on Figure 4.7, showing approximate molecular weight dependence of the viscosity coefficients. We find a single line with vertical shifts can roughly describe all viscosity (η, $|\eta^*|_{poly}$ and $|\eta^*|_{oriented}$), giving approximate power law exponents of 2.5 ± 0.3 at high M_w and highly nonlinear dependence at low M_w. Taken together with corresponding rotational viscosity data, the trend of decreasing M_w dependence for both shear viscosity and rotational viscosity may imply a crossover transition from rod to semiflexible chain with increasing chain length.

A large anisotropy was observed between the rotational viscosity and the shear viscosity. The rotational viscosity was almost two orders of magnitude higher than the shear viscosity (Figure 4.8). The ratio of γ_1/η is used to measure the viscous anisotropy. As shown in Figure 4.9, γ_1/η displayed a sharp decrease with increasing M_w starting from low molecular weight limit, followed by a much weaker dependence as $M_w > 7\ 000$ g/mol. The greater anisotropy observed at low-M_w reflects larger conformational anisotropy, probably due to rod-like nature of the chain, while the saturation of γ_1/η again signals significant chain flexibility and may be relevant to the formation of hairpins.

4.4 Discussion

The molecular weight dependence of the viscosity reflects the nature of the polymer chain (rod-like, semi-rigid, flexible) and the topological constraints (with or without hairpins). This has been the subject of several theoretical predictions [21, 22, 26]. In the case of main

chain LCPs, all theories predicts a weaker molecular weight dependence with increasing chain flexibility regardless of specific models. Theoretical models for liquid crystalline polymers predict power-law molecular-weight dependence of viscosity coefficients, i.e., γ_1 (or η) $\propto M_w^\alpha$, with α predicted to be 6 for rigid-rods, 2 for semi-rigid chains and 1 for semiflexible chains that adopt hairpin conformations. Further, all viscosity coefficients are predicted to have the same molecular weight dependence.

In contrast to theoretical model predictions, different measure of viscosity coefficients, for example, rotational viscosity and shear viscosity, have different molecular weight dependence. For rod-like lyotropic LCPs, rotational viscosity only shows a slight non-linear dependence on molecular weight [2], while the shear viscosity has a strong non-linear dependence on molecular weight with $\alpha \approx 6$. This situation is even more ambiguous for mesogen-spacer type thermotropic LCPs. For AZA9 and DDA9, the rotational viscosity has power law exponent α greater than 5 [7], in comparison to their shear viscosity having the α value of 3.95 [3]. In the case of DHMS-7,9, the rotational viscosity shows weaker dependence on molecular weight than the shear viscosity at both low and high molecular weight limits (Figure 4.8). The relative sensitivity of γ_1 and τ to molecular weight for DHMS-7,9 is same as that of lyotropic PBG, but opposite to that of AZA9 and DDA9. In explaining the differences between γ_1 and η, Esnault and coworkers propose a distinction between "large" viscosities and "small" viscosities, and suggest that γ_1 belongs to the category of large viscosities and η belongs to the category of small viscosities [27]. This distinction presents an explanation for the 1-2 orders of magnitude difference between γ_1 and η, but the nature for different sensitivity to molecular weight between these two viscosities remains elusive.

The change in molecular weight dependence with increasing chain length may signal the transition of chain conformation from rod-like to semiflexible. For DHMS-7,9, both rotational and shear viscosities show weaker dependence on M_w at the high molecular weight limit. This behavior is qualitatively similar to the rotational viscosity of AZA9, which also shows less sensitivity to molecular weight with increasing chain length [6]. DHMS-7,9 differs from AZA9 in that the latter system shows a much stronger molecular weight dependence at both low and high M_w limits. This difference may be attributed to much higher viscosity (two orders of magnitude) of AZA9, leading to poor quality of monodomain because of insufficient magnetic annealing (according to our experience, even several days of mag-

netic annealing at a 2 Tesla field is not sufficient to generate good quality monodomains for DHMS-7,9 with high M_w). The less-ordered chain segments could create significant viscous resistance to director reorientation. Therefore, the rotational viscosity based on reorientation of a poor monodomain is expected to be larger than its real value. Indeed, the γ_1 value measured from monodomain samples [28] is more than one order of magnitude smaller than that determined from NMR reorientation measurements [8]. Thus, the determined γ_1 values of both DHMS-7,9 and AZA9 probably only have relative meaning for different molecular weight samples. The overestimation of γ_1 is anticipated to be more significant for samples with high viscosity, which may explain the surprisingly strong non-linear molecular weight dependence observed in AZA9.

In principle, the characteristic molecular weight M_w^c corresponds to a chain length where hairpins start to form. This provides an easy way to estimate the average contour length between consecutive hairpins (h). In the case of DHMS-7,9, the contour length for a fully extended chain at $M_w^c \approx 7\ 000$ g/mol is estimated to be around 200 Å, which corresponds to a length-to-diameter ratio $L/d \approx 36$.

It appears that the choice of alkyl spacer is probably a factor that influences the rodlike-to-semifleixble transition. For DHMS-7,9, the estimate of the contour distance between consecutive hairpins is much lower than in a different mesogen-spacer type thermotrope (TPB-10) with similar mesogen structure to DHMS-7,9. In the latter case, the contour length between consecutive hairpins is determined to be around 320 ± 20 Å from small angle neutron scattering measurements [30], suggesting a crossover, if present in TPB-10, will occur at a higher molecular weight. It is noteworthy that in both systems, DHMS-7,9 (7 and 9 -CH_2 spacer) vs. TPB-10 (10 -CH_2 spacer), and AZA9 (7 -CH_2 spacer) [6] vs. DDA9 (10 -CH_2) [7], crossover transition seems to occur at a lower molecular weight for odd number of spacers than for even number of spacers. Since the alkyl spacers of 7, 9 and 10-carbon present comparable molecular flexibility to the nematic chain, the shift of the crossover transition to higher molecular weight for LCPs with 10-carbon spacer may be attributed to their higher order parameter (S), for example, AZA9 with the degree of polymerization of 8-10 has an order parameter of 0.5, as opposed to the S value of 0.7 for DDA9 with the same degree of polymerization [31]. Since the energy required to build up hairpins is a function of order parameter [21], and intuitively, a larger S value presents a higher energy barrier for polymer chain to make an abrupt U-turn in mesogen orientation,

the crossover may thus shift to a higher molecular weight for LCPs with higher order parameter. This may explain why crossover is relatively easy to detect in DHMS-7,9 and AZA9.

4.5 Conclusion

The overall decreasing sensitivity of rotational and shear viscosities to molecular weight for DHMS-7,9 may signal a crossover transition from rigid rod to semiflexible chain. This transition roughly corresponds to the chain length where hairpin starts to form. An average contour distance between consecutive hairpins for DHMS-7,9 is estimated to be around 200 Å.

Appendix

The actual molecular weights of DHMS-7,9 were obtained using a size exclusion chromatography (SEC) equipped with a multi-angle light scattering (MALS) detector at Wyatt Technology Corporation in Santa Barbara, California. The MALS detector is Wyatt Technology DAWN EOS with a solid state laser operating at 690 nm, and the concentration of elute is measured by Wyatt Technology Optilab DSP differential refractometer operating at the same wavelength. The combination of SEC-MALS provides an accurate determination of molecular weight due to the absence of assumptions regarding molecular conformation of the sample in solution.

DHMS-7,9 of two different molecular weights (DHMS-7.6K and DHMS-28K) were dissolved in tetrahydrofuran (THF) and analyzed 4 hrs after solution preparation by mild heating ($\sim$ 30°C). Typical SEC-MALS chromatograms obtained for a polymer sample are depicted in Figure 4.10, showing that the peaks given by tow detectors are of different size and shape. This is because the intensity of scattered light is proportional to both molar mass and concentration of molecules for any elute, whereas the signal from the refractometer is only proportional to the concentration of the molecules. The determination of absolute molecular weights requires the signal from both light scattering and refractive index detectors.

Molecular weight of the polymer is calculated for each data slice, roughly corresponding to 1/4 second, of the selected chromatographic peak by means of a Debye plot, as shown in Figure 4.11. The signal from each light scattering detector between 15° and 160° at a

particular data slice is plotted vs. $\sin^2(\theta/2)$, and the intercept of a linear extrapolation to the $\theta = 0$ corresponds to the inverse of molecular weight M for that elute. A series of M values are obtained at different time of elution to calculate M_w and M_n. The absolute M_w for DHMS-7.6K and DHMS-28K are equal to 8 550±100 g/mol and 31 600±30 g/mol, respectively. Both values are approximately 12.5% larger than what we determined from polystyrene-equivalent GPC measurements.

Sample	M_w(g/mol)*	M_n(g/mol)*	PDI	T_m(°C)	T_{xn}(°C)	T_{ni}(°C)
DHMS-5K	5000	2400	2.1	70.4	110.2	170.9
DHMS-7.6K	7600	3200	2.0	81.8	100.5	173.0
DHMS-11K	11000	5200	2.1	86.9	103.8	181.0
DHMS-16.5K	16500	6900	2.4	92.0	118.8	190.2
DHMS-28K	28500	11700	2.4	91.8	120.0	192.0
DHMS-65K	65000	29500	2.2	94.6	127.8	202.0

Table 4.1: Materials and phase characterization for DHMS-7,9 samples. *Polystyrene-equivalent values (in CH_2Cl_2) are given here for consistency with prior literature [13, 14]; recent light scattering results indicate the actual molecular weight is $\sim$ 12.5% greater than the polystyrene-equivalent values obtained by GPC.

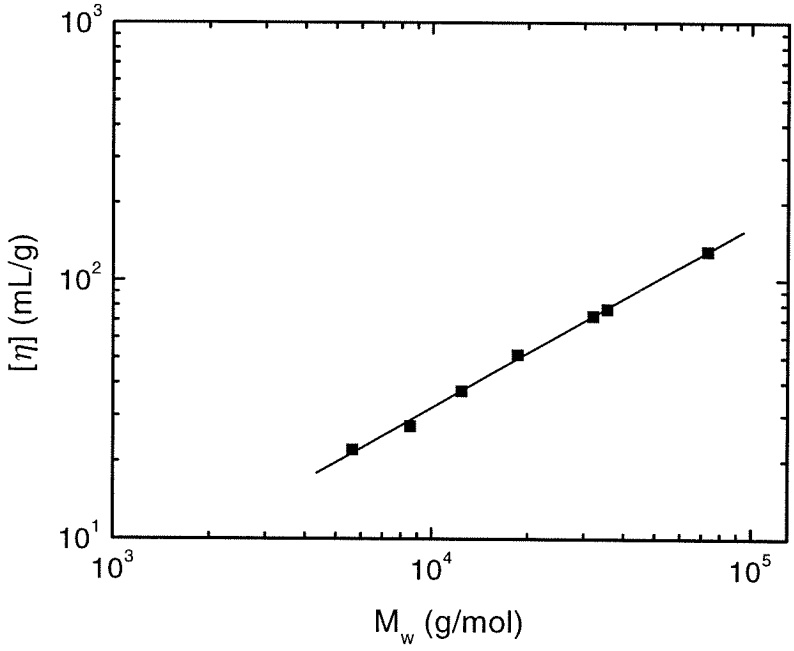

Figure 4.1: Intrinsic viscosity $[\eta]$ of DHMS-7,9 as a function of polystyrene-equivalent molecular weight M_w in the solvent of 1,2-dichlorobenzene at 33.5°C.

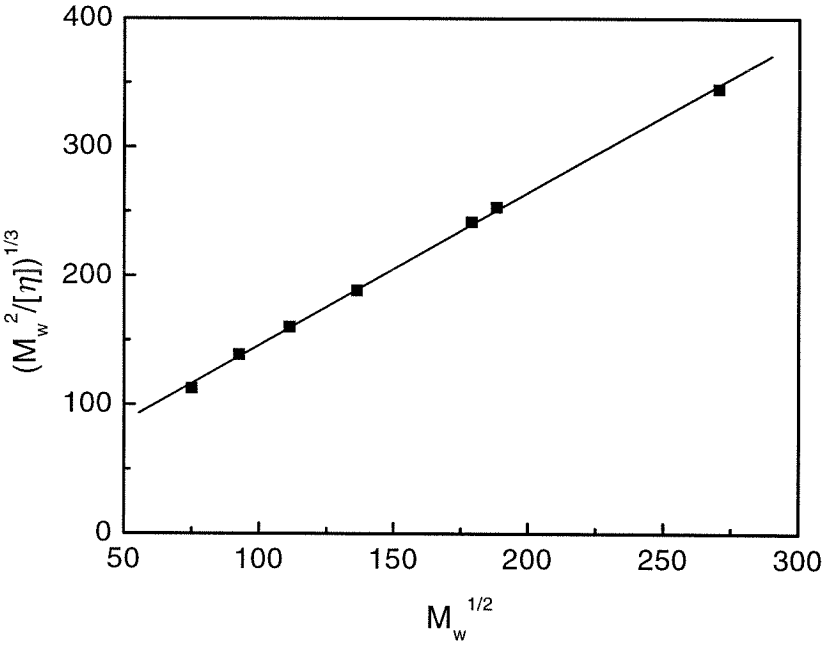

Figure 4.2: A re-plot of intrinsic viscosity following Bohadanecky's treatment.

a.

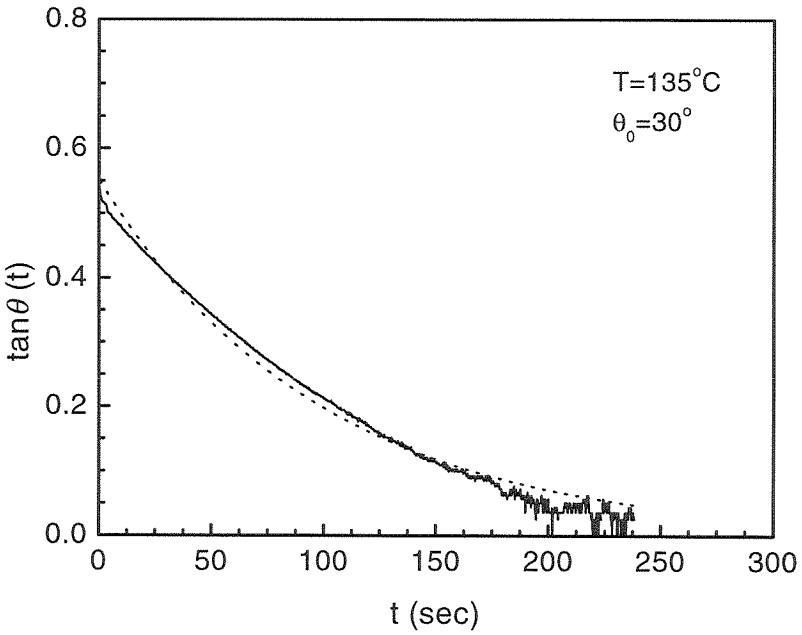

b.

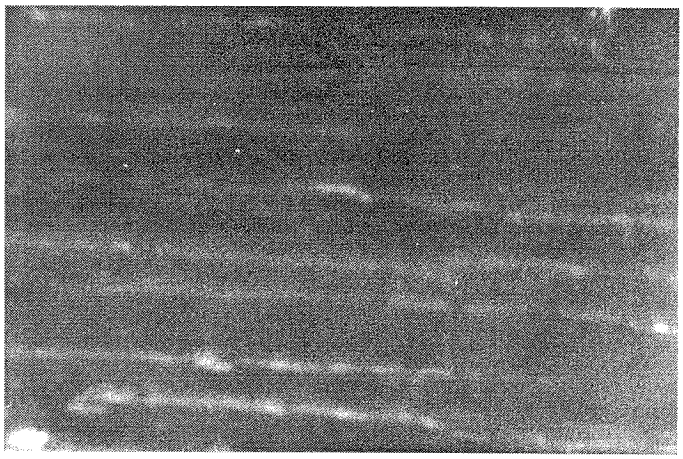

Figure 4.3: (a) The solid line is a typical director reorientation curve for DHMS-7,9 (M_w = 5 000 g/mol) in the magnetic field (H = 2 Tesla) at 135°C, and the dashed line is a single-exponential decay fitting curve. The reorientation angle θ_0 was 30°. (b) Micrograph of disclination walls observed under cross polarizers in DHMS-7,9 (M_w = 7 600 g/mol) during magnetic reorientation. The width of micrograph corresponds to 54.7 μm.

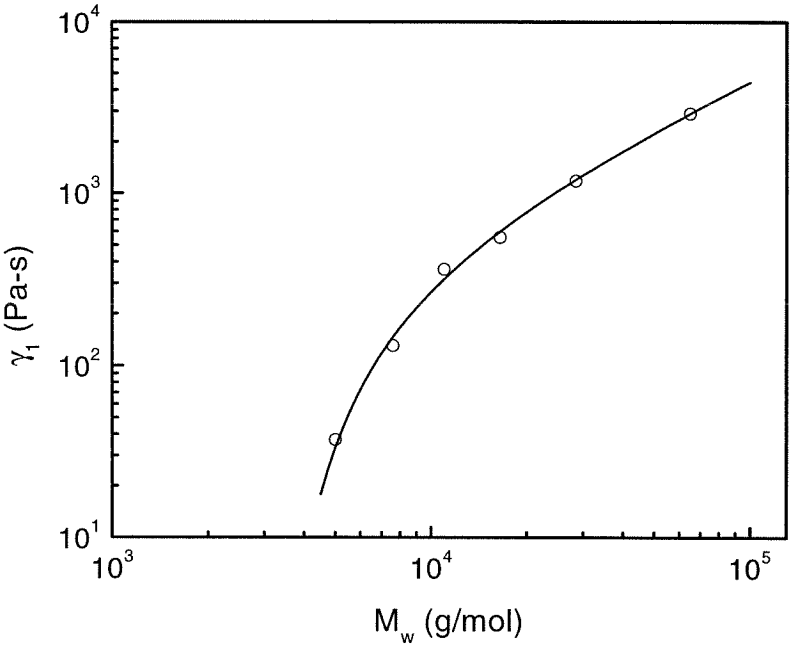

Figure 4.4: The estimated γ_1 as a function of M_w at 135°C for DHMS-7,9, assuming $\Delta\chi_a = 1.0 \times 10^{-8}$, with a solid line showing the trend of γ_1's molecular weight dependence.

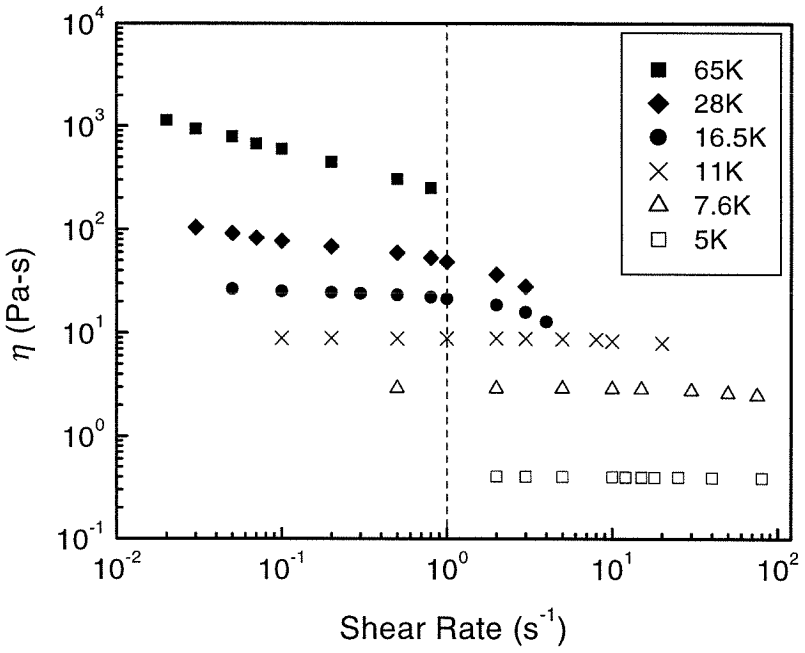

Figure 4.5: The steady shear viscosity as a function of shear rate ($\dot{\gamma}$) in the nematic phase (at 135°C) for different molecular weight samples.

a.

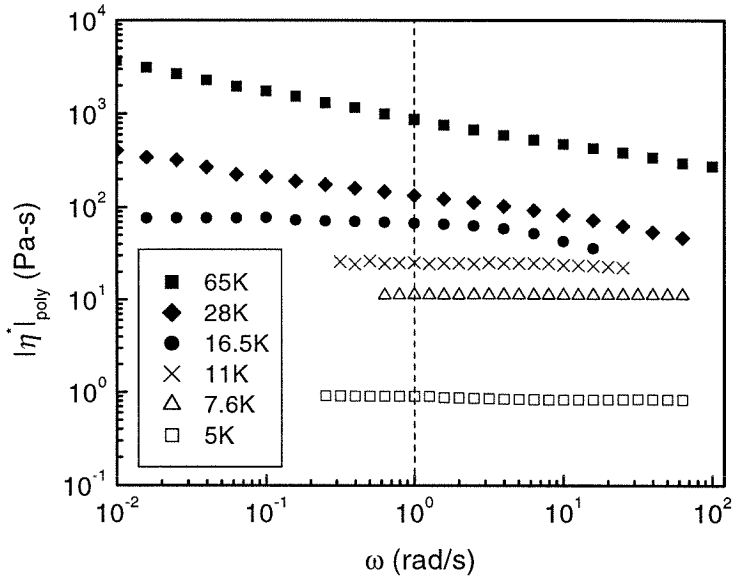

b.

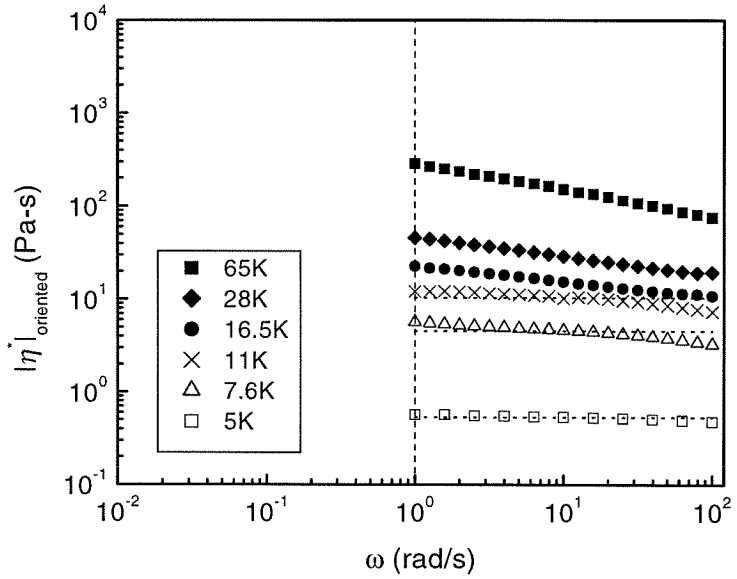

Figure 4.6: (a)The complex shear viscosity of polydomain samples, $|\eta^*|_{poly}$ vs. ω; (b) The complex shear viscosity of shear-oriented samples, $|\eta^*|_{oriented}$ vs. ω. Three horizontal dotted lines ($\cdots\cdots$) in Figure 5c (5K, 7.6K and 11K) represent the viscosity values averaged from $\omega = 100$ to 1 rad/s. In part (b), the complex viscosities have only been reported in two decades (100-1 rad/s) because viscosity measurements at low oscillatory frequency are complicated by considerable relaxation of shear-induced orientation.

a.

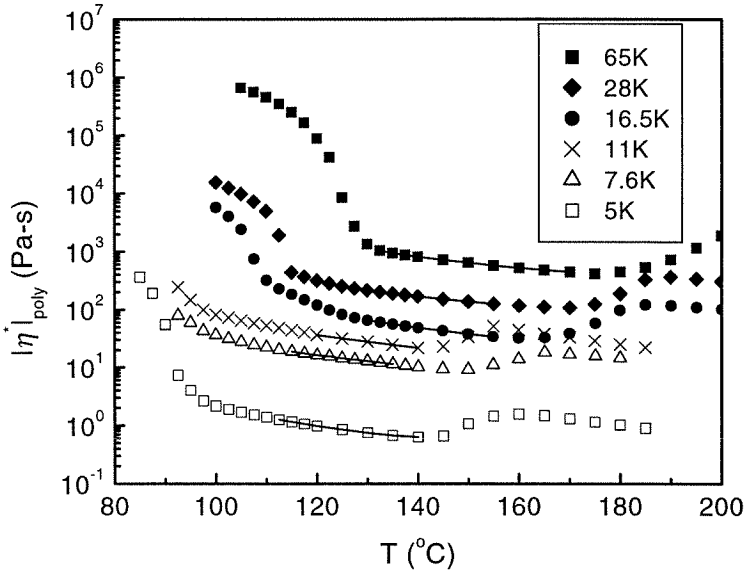

b.

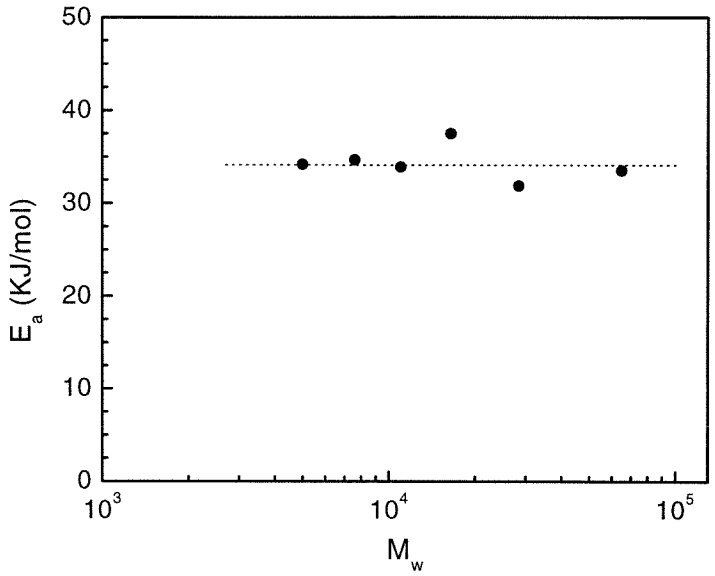

Figure 4.7: (a) Temperature dependence of ($|\eta^*|_{poly}$) at a single frequency $\omega = 5$ rad/s and strain of 5%; (b) The flow activation energy of the nematic phase as a function of M_w. The calculation of flow activation energy is based on viscosity data which have line connected to.

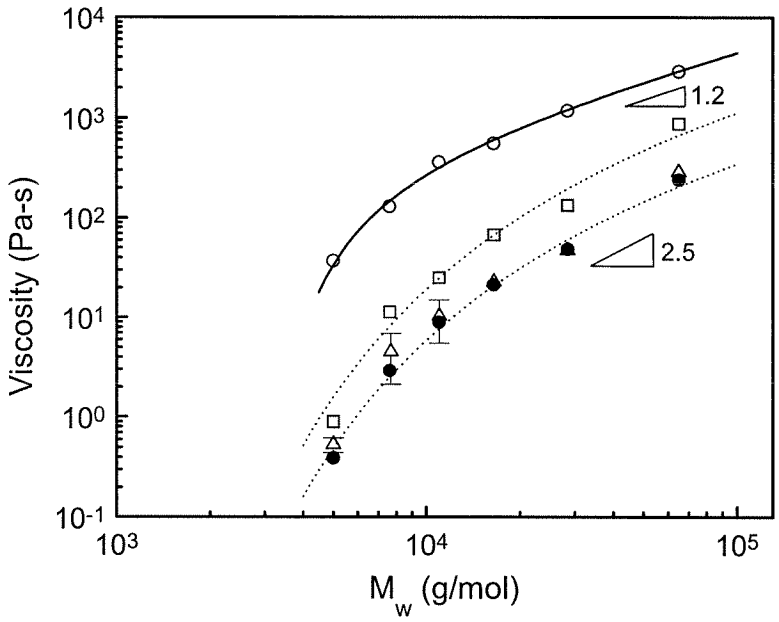

Figure 4.8: The shear viscosity in the pseudo-Newtonian region (at $\dot{\gamma} = 1$ s^{-1} or $\omega = 1$ rad/s) as a function of molecular weight at 135°C: the steady shear viscosity η (●), the complex shear viscosity of polydomain state $|\eta^*|_{poly}$ (□), and the complex shear viscosity of shear oriented state $|\eta^*|_{oriented}$ (△). The error bars on the $|\eta^*|_{oriented}$ data for $M_w \leq 11000$ g/mol indicates the range of maximum and minimum viscosity measured from $\omega = 100$ to 1 rad/s, owing to unavoidable orientation relaxation in these samples. The corresponding data for rotational viscosity (○) are also included for comparison.

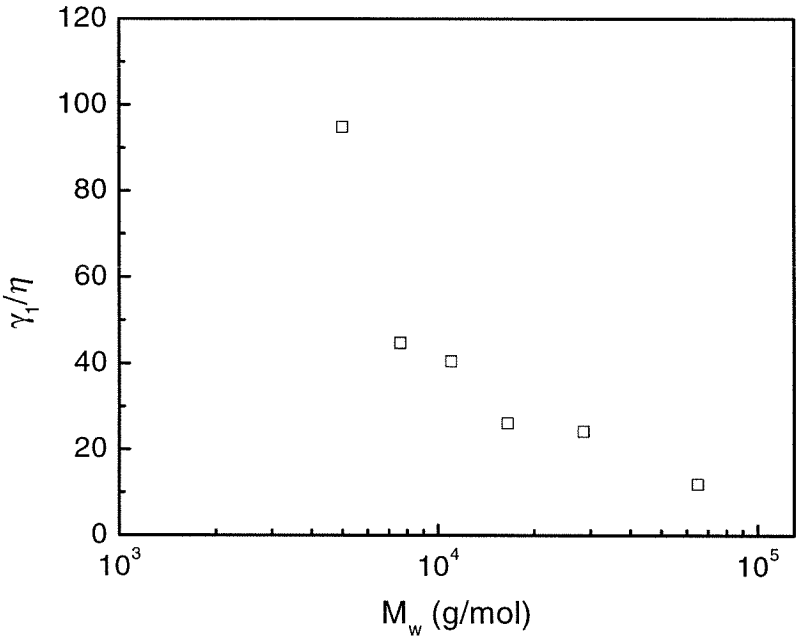

Figure 4.9: Viscosity ratio, γ_1/η, as a function of molecular weight at 135°C.

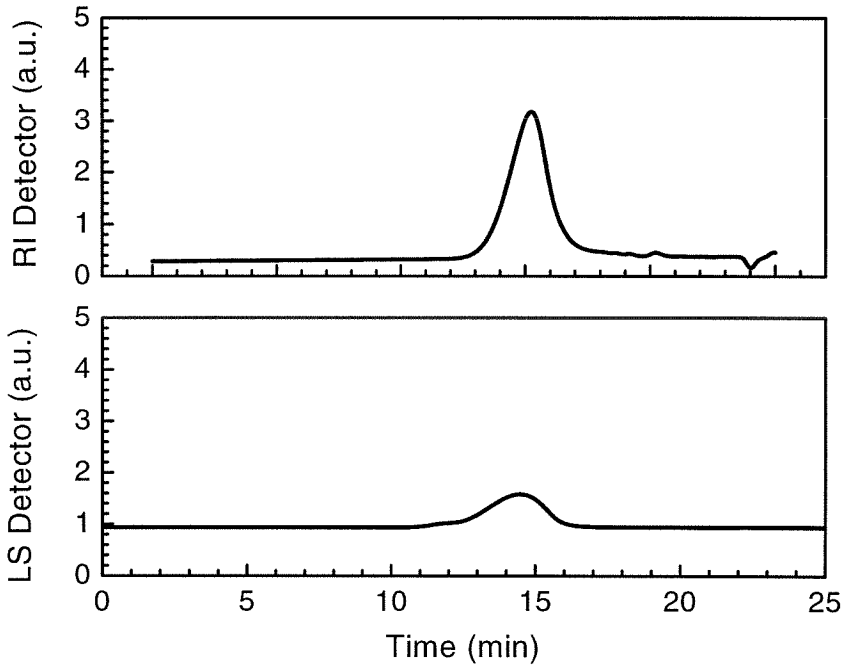

Figure 4.10: SEC chromatograms of DHMS-7.6K with signals from the refractive index detector (top) and the light scattering detector at 90° (bottom).

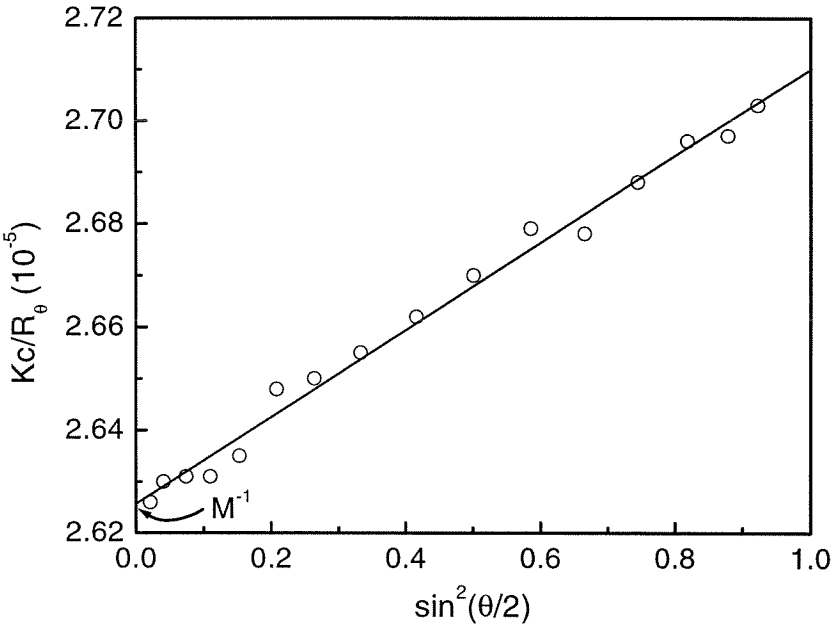

Figure 4.11: Debye plot of one data slice from the SEC chromatogram of DHMS-28K sample. This plot shows the fit of the light scattering intensity from 16 different detectors from 15° to 160° of the DAWN EOS MALS system to extract the molecular weight M of individual slice.

Bibliography

[1] M. Doi. *J. Polym. Sci.: Polym. Phys.*, 19:229, 1981.

[2] S.-D. Lee and R. B. Meyer. *Liq. Cryst.*, 7:15, 1990.

[3] A. Blumstein, O. Thomas, and S. Kumar. *J. Polym. Sci. Part B: Polym. Phys.*, 24:27, 1986.

[4] S. S. Kim and C. D. Han. *Macromolecules*, 26:6633, 1993.

[5] A. Romo-Uribe and A.H. Windle. *Macromolecules*, 28:7085, 1995.

[6] P. Esnault, F. Volino, A. F. Martins, S. Kumar, and A. Blumstein. *Mol. Cryst. Liq. Cryst.*, 153:143, 1987.

[7] T. Klein, H. X. Jun, P. Esnault, A. Blumstein, and F. Volino. *Macromolecules*, 22:3731, 1989.

[8] J. S. Moore and S. I. Stupp. *Macromolecules*, 20:282, 1987.

[9] N. Heaton, D. Reimer, and G. Kothe. *Ber. Bunsenges. Phys. Chem.*, 97:1320, 1993.

[10] A. Blumstein. *Polym. J (Jpn.)*, 17:277, 1985.

[11] S. D. Hudson, A. J. Lovinger, R. G. Larson, D. D. Davis, R. O. Garay, and K. Fujishiro. *Macromolecules*, 26:5643, 1993.

[12] F. Elias, S. M. Clarke, R. Peck, and E. M. Terentjev. *Macromolecules*, 33:2060, 2000.

[13] W-J. Zhou, J. A. Kornfield, V. M. Ugaz, W. R. Burghardt, D. R. Link, and N. A. Clark. *Macromolecules*, 32:5581, 1999.

[14] V. M. Ugaz, W. R. Burghardt, and W. J. J. A. Kornfield. *J. Rheology*, page (submitted), 2000.

[15] H. Yamakawa and M. Fujii. *Macromolecules*, 7:128, 1974.

[16] M. Bohdanecky. *Macromolecules*, 16:1483, 1983.

[17] F. Hardouin, M. F. Achard, and H. Gasparoux. *J. Polym. Sci. Polym. Phys.*, 20:975, 1982.

[18] R. A. Wise, A. Olah, and J. W. Doane. *J. Phys. (Les Ulis, Fr.)*, 36:117, 1975.

[19] C. G. Sridhar, W. A. Hines, and E. T. Samulski. *J. Chem. Phys.*, 61:947, 1974.

[20] S. Götz, W. Stille, G. Strobl, and H. Scheuermann. *Macromolecules*, 26:1520, 1993.

[21] P. G. de Gennes. In A. Ciferri, W. R. Krigbaum, and R. B. Meyer, editors, *Polymer Liquid Crystal*, chapter 5. Academic Press, New York, 1982.

[22] R. B. Meyer. In A. Ciferri, W. R. Krigbaum, and R. B. Meyer, editors, *Liquid Crystal Polymer*, chapter 6. Academic Press, New York, 1982.

[23] M. Doi and S. F. Edwards. *The Theory of Polymer Dynamics.* Oxford University Press, New York, 1986.

[24] S. Onogi and T. Asada. In G. Astarita, G. Marrucci, and L. Nicolais, editors, *Rheology*, volume 1. Plenum Press, New York, 1980.

[25] K. F. Wissbrun. *British Polymer Journal*, 12:163, 1980.

[26] N. Kuzuu and M. Doi. *Jpn. J. Phys. Soc.*, 53:1031, 1984.

[27] P. Esnault, J. P. Casquilho, F. Volino, A. F. Martins, and A. Blumstein. *Liq. Cryst.*, 7:607, 1990.

[28] S. Zheng-Min and M. Kleman. *Mol. Cryst. Liq. Cryst.*, 111:321, 1984.

[29] S-D Lee and R. B. Meyer. *Phys. Rev. Letts.*, 61:2217, 1988.

[30] F. Hardouin, G. Sigaud, M. F. Achard, A. Brulet, J. P. Cotton, D. Y. Yoon, V. Percec, and M. Kawasumi. *Macromolecules*, 28:5427, 1995.

[31] A. Blumstein, M. G. Gauthier, O. Thomas, and R. B. Blumstein. *Faraday Discuss. Chem. Soc.*, 79:33, 1985.

Chapter 5 Flow Behavior of A Distinct Liquid Crystalline Phase

5.1 Introduction

Liquid crystals possess unique and interesting inter-relationships between molecular order and applied flow. For nematics, structure and rheology are largely determined by the response of the director orientation to applied flow, while the flow behavior of smectics is governed by a complex interplay between layer order and applied flow. The understanding of the flow properties of ordered fluids, therefore, helps to provide important physical insight into the underlying structure of mesophase. This can be particularly helpful when usual techniques for characterizing the structure of a mesophase yield ambiguous results. In the case of DHMS-7,9, recall from Chapter 3 that an intermediate liquid crystalline phase (Phase X) exists between crystalline solid and nematic phase. Although previous attempts to characterize the structure of Phase X have failed to yield a definite description [1, 2], our recent studies have identified some rheological signature of layered ordering in Phase X. The purpose of this chapter is to address the distinct structure of this mysterious mesophase, and its associated rheological and orientational behavior.

We find that shear rheology and orientation of Phase X are completely different from that of the nematic phase. Shear thinning dominates over the entire range of shear rates we studied, accompanied by an anomalous normal stress behavior. In contrast to the nematic phase where shear alignment is along the flow direction (Chapter 3), a striking flip of the orientation from the flow direction to the vorticity direction occurs below a critical shear rate in Phase X. This orientational flipping is reversible in response to step changes of temperature and/or shear rate. This type of orientational flipping, reminiscent to the flip of orientation observed in small molecule smectics, such as 8CB [3], can also be induced using large amplitude oscillatory shear by varying applied frequency.

5.2 Experimental

5.2.1 Materials

DHMS-7,9 with polystyrene-equivalent M_w of 28 440 g/mol is used for this study. Recall that Phase X exists within a temperature range of approximately 92 to 120°C for this molecular weight (Figure 3.1). This sample offers a fairly wide Phase X range compared to lower M_w samples, and allows rheology and orientation measurements at relatively large shear rates due to its lower viscosity compared to higher M_w sample. All data presented in this chapter are therefore exclusively for 28K molecular weight DHMS-7,9. For samples of other molecular weights, their shear rheology and orientation behavior in Phase X are qualitatively similar to that of 28K sample.

5.2.2 Powder X-ray Diffractometry

Powder X-ray diffraction was carried out on NSLS beamline X10A by our collaborator Prof. Noel Clark of the University of Colorado, Boulder. A germanium mono-chromator was chosen for its high resolution of 0.0007 Å^{-1}. Samples were contained in 1 mm diameter thin wall quartz capillaries inside an aluminum oven with temperature control. Data are presented as X-ray counts (intensity) normalized by the incident monitor count rate.

To examine the mesophase behavior of DHMS-7,9, the sample was first heated to the isotropic state (205°C) for 20 min, then slowly cooled into the nematic phase (or x-phase), and allowed to equilibrate for at least 30 min before measurements. We also investigated thermal hysteresis of the phase behavior by heating the sample from room temperature directly to each desired temperature in the x-phase (or nematic phase) without going to the isotropic state. Diffraction measurements were obtained on these samples after 30 min of thermal equilibration.

5.2.3 Rheology and Orientation Measurements

Sample preparation for rheological study and shear orientation measurements were identical to those described in Chapter 3. Mechanical experiments were conducted on a Rheometrics ARES rheometer with a force-rebalance transducer (2000 g·cm torque) using a cone-and-plate geometry (25 mm diameter, 0.1 rad cone angle). Wide angle X-ray scattering mea-

surements were performed using a modified Linkam CSS-450 high temperature shearing cell.

A sample-loading procedure was developed specifically for rheological measurements in the x-phase. The molded sample disk was first placed on the 25 mm plate and then heated to 140°C. We reduced the center gap thickness to about 250 μm at 140°C after thermal equilibration. Then we heated the sample to the isotropic state while simultaneously adjusting the gap to keep normal force small ($\leq$10 grams). After the sample was thermally cleared, we cooled it slowly to the x-phase while constantly adjusting the gap thickness. After about 5 minutes of thermal equilibration in the x-phase, we adjust the final center gap gradually to about 50 μm. It usually takes several hours to relax the normal force caused by the squeezing flow during the final gap setting in the cone-and-plate configuration.

5.3 Phase Behavior

5.3.1 Subtle Structure of Phase X from Powder X-ray Diffraction

To examine the nature of the intermediate x-phase, high resolution powder X-ray diffraction has been performed. Upon cooling from the isotropic state, the isotropic-nematic transition is manifested by the growth of a broad diffraction peak in $I(q)$ at $q \approx 1.25$ Å^{-1} (Figure 5.1a, 166°C, 150°C, 135°C). This liquid-like diffuse peak is characteristic of interchain packing correlations in the nematic phase. The peak position shifts out with decreasing temperature, varying from $q \approx 1.2$ to 1.4 Å^{-1}, corresponding to effective interchain spacings ranging from 5.5 to 4.5 Å. On moving from 135°C into the temperature range associated with Phase X (119°C, 106°C and 96°C), the interchain correlation peak simply shows the usual increase of intensity and slight shift to larger q that is typical for the nematic phase with decreasing temperature. Thus, there is no evidence of a more ordered structure (compared to nematic order) forming when cooling through the x-phase (120-92°C). Higher order structure first appears at much lower temperature. A sharp diffraction peak at $q \approx 1.65$ Å^{-1} is evident at 78°C and below (Figure 5.1a), attributed to crystallization at low temperatures. In addition, a small angle peak characteristic of crystal-like layer ordering appears at $q \approx 0.32$ Å^{-1} upon crystallization during cooling (at T = 78°C, 72°C and 45°C, Figure 5.1b). This peak corresponds to a layer spacing of 19.6 Å and has no observable harmonics [4], as is common for either the layer ordering of smectic LCs or the lamellar superstructure of semicrystalline

polymers. The finite peak width of about 30 times the diffractometer resolution suggests such layering is short ranged. The correlation length obtained from fitting the peak to a Lorentzian lineshape is about 58 Å.

In principle, such layer ordering could be crystalline or smectic. Our observation rules out the possibility that the x-phase is *purely* smectic for at least two reasons. First, this layering peak is about a factor of 10 smaller in integrated intensity than that observed for a typical smectic LC in the same sample geometry, suggesting that only a small part of the sample adopts layer ordering. Second, the sample showed a rather large structural hysteresis in the x-phase: upon heating from room temperature, the small q scattering peak ($q \approx 0.32$ Å^{-1}) persists with increasing temperature (Figure 5.1c). Smectics do not show such hysteresis. It must be emphasized that by X-ray diffraction the x-phase is not distinguishable from the nematic when sample is cooled from the isotropic state. Even when the sample was annealed at 99°C for 24 hrs after cooling from the isotropic state, no small q scattering peak other than that associated with nematic ordering was observed, as shown in Figure 5.1c. Therefore, we will refer the above mentioned layer ordering as *residual order*, since it occurs only when the sample is heated from room temperature into the x-phase but *not* for the case when the sample is cooled from the isotropic state to the x-phase.

There is a smooth background scattering, monotonically increasing with decreasing q in the scattering profile for $q < 0.25$ Å^{-1} (Figure 5.1b). This is definitely due to the DHMS-7,9 sample, since the empty cell or a typical smectic LC produces only a flat background at the intensity of 2×10^{-4}. The monotonic background is characteristic of random spatial variations in density. A curve fit of the background to a constant plus a power law component works well, giving a variation with q as q^{-v}, with $v \approx 2$. This fall-off with q is indicative of density fluctuations having Ornstein-Zernike type spatial correlations. We suspect that the origin of this background is due to some kind of non-homogeneous spatial organization of the polymer. In particular, it may arise from heterogeneity associated with the statistics of incorporation of 7- and 9-methylene spacers in the polymer chain.

5.3.2 Rheological Signatures of Phase X

Further insight into the phase transitions is gained by examining the rheological properties of DHMS-7,9. The temperature dependence of the apparent steady shear viscosity at a fixed rim shear rate (0.1 s^{-1}) shows pronounced changes associated with the x-nematic and

nematic-isotropic transitions (Figure 5.2). With an increase of temperature from 100°C, a dramatic drop in viscosity is apparent at $T \approx$120°C (Figure 5.2), which coincides with the x-nematic transition, as evident by DSC. The apparent shear viscosity in the nematic phase is more or less constant, decreasing slightly with an increase of temperature for 120°C< T < 170°C. An increase in the apparent viscosity at 170°C< T <185°C suggests entrance of the nematic-isotropic biphase region. The apparent viscosity decreases again with temperature when the sample is fully isotropic. The nematic-isotropic biphase region is very wide with an onset temperature around 175°C. For comparison, the complex viscosity as a function of temperature was also measured (at ω=5 rad/s, rim strain amplitude=5%). It showed the same broad nematic-isotropic transition and narrow x-nematic transition. The x-nematic transition determined from the complex viscosity shifted slightly to lower temperature and was very sharp. The phase transitions as indicated by rheology agree with the DSC data (Figure 3.1).

The linear viscoelastic behavior also reflects microstructure difference between Phase X and the nematic phase. When undercooling from the nematic phase is about 5-10°C (from T_{xn} = 120°C to 115°C and 110°), the storage modulus increases by about two orders of magnitude (Figure 5.3a). This is contrast to the observation of powder X-ray diffraction which shows no structural difference from nematic ordering at this undercooling (Figure 5.1), suggesting higher sensitivity of rheological methods in detecting mesophase transitions. The enhancement in G' can be also viewed as a dramatic slowing down of dynamics in Phase X. Power law behavior is not exhibited in the x-phase, instead a plateau-like modulus occurred at low frequencies ($\omega \approx$0.1 rad/s at 115°C). The storage modulus also follows an approximate $t-T$ superposition for all the temperatures in the x-phase (Figure 5.3b), with a small overlap in G' between the nematic (148°C) and the x-phase.

A Cole-Cole plot (log G' vs. log G'') can reveal departure from $t-T$ superposition without the uncertainty associated with arbitrary shift factors. At high modulus values, plots of log $G' \sim$ log G'' in the isotropic, nematic and x-phases fall almost on the same curve with small deviations, but at low modulus the curves for different phases are distinct (Figure 5.4a). This is not unexpected since linear viscoelasticity at high frequency is mainly governed by local chain dynamics. The Cole-Cole plots at different temperatures within the same phase nearly follow the same curve, which justifies the approximate time-temperature superposition used above. The log G' vs. log G'' curves for the x-phase lie above those of

the isotropic and nematic phases, with the occurrence of a small plateau at low G''. The Cole-Cole plots for the nematic phase also lie above those of isotropic phase. This could be attributed to the distortional elasticity related to the defect structure in the nematic phase, which leads to an enhancement of the storage modulus and therefore a long relaxation tail at low oscillatory frequency. The curve for the nematic-isotropic biphase at 185°C follows those of the isotropic state at high G'' values (in accord with the isotropic phase being the continuum matrix), but has slightly higher G' at low frequency (or low G'') values, which may be due to the distortion of the dispersed nematic droplets.

The shift factors exhibited Arrhenius dependence in the isotropic and nematic phases (Figure 5.4b). The approximate shift factors (a_T) that provide the best superposition at high modulus show abrupt changes in the vicinity of isotropic-nematic and nematic-x-phase transitions. The large increase of a_T in the x-phase again indicates much slower dynamics. The flow activation energy for the isotropic phase is roughly equal to that of the nematic phase, but much lower than that of the x-phase.

5.4 Shear Rheology and Orientation

5.4.1 Flow Curve

The steady shear viscosity and first normal stress difference of the x-phase behave very differently from that of the nematic phase. Shear thinning dominates over the entire range of shear rates studied (Figure 5.5), and no plateau region was observed. The viscosity is roughly two orders of magnitude higher in the x-phase than in the nematic, as expected on the basis of the linear viscoelastic properties.

The steady state N_1 is positive for all the shear rates in the x-phase. There is an appreciable first normal stress difference even at shear rates as low as 0.02 s^{-1} (Figure 5.5). The change of N_1 with shear rate is not monotonic. It first increases with shear rate and reaches a local maximum at $\dot{\gamma} \approx 2.5$ s^{-1}, and then decreases with further increase of the shear rate and reaches a local minimum at $\dot{\gamma} \approx 20$ s^{-1}. N_1 increases again at higher shear rates ($\dot{\gamma} > 20$ s^{-1}). Slight edge fracture occurs at a shear rate around 20 s^{-1}. This can be suppressed by shearing samples at low shear rates (0.02 s^{-1}) before commencing high shear rate flow. According to the results of Baek et al. on highly concentrated hydroxypropylcel-

lulose (HPC) solutions, mild edge fracture does not change the qualitative trend (increase or decrease) of N_1 measurements [5].

5.4.2 Observation of Parallel and Perpendicular Orientations

During steady shear two qualitatively different types of oriented WAXS patterns were observed. One is indicative of mesogens predominantly oriented along the flow direction ("parallel"), and the other is for mesogens with their preferential orientation along the vorticity direction ("perpendicular"). The magnitude of the "orientation parameter" (Section 3.2.3) S was computed with different reference axes for parallel and perpendicular orientations, along the flow direction and the vorticity direction, respectively. In this way, computed S values are always positive, reflecting the degree of alignment relative to the prevailing orientation direction. In presenting results here, positive values of S are used to denote molecular orientation in the parallel orientation state, while negative values of S denote orientation in the perpendicular orientation state. The degree and direction of molecular orientation depend on temperature and shear rate (T,$\dot{\gamma}$). Thermal history also appears to affect shear orientation behavior, as described below.

5.4.2.a. Effect of Temperature and Shear Rate

Comparison of the 2-D orientation parameter (S) and the corresponding shear viscosity (η) as a function of temperature during steady shear at a low rate shows the correlation between the change in the molecular orientation and the macroscopic flow properties (Figure 5.6). An orientation transition from perpendicular to parallel occurs as temperature increases through the x-nematic phase transition. This transition coincides with a dramatic decrease in viscosity with temperature. The degree of the molecular orientation is more or less constant throughout the whole nematic range. As the temperature approaches the nematic-isotropic transition, the orientation parameter decreases to zero over the same temperature range where the increase in shear viscosity is observed.

The shear-rate dependence of S is qualitatively different in the nematic and x-phases. At temperatures well within the nematic phase, there is little change in orientation with shear rate (Figure 3.5). This simple orientation behavior changed dramatically at temperatures near and below the transition to the x-phase. At 120°C (T_{xn}), a monotonic increase of orientation with the applied shear rate was observed and the final orientation is relatively

lower compared to that for the nematic phase. Below T_{xn} (at 100°C and 110°, Figure 5.7), there exists a critical shear rate $\dot{\gamma}_c$, below which perpendicular orientation (S <0, along the vorticity direction) was observed and above which the orientation flipped back to the flow direction ($S > 0$). A progressive change from the perpendicular to the parallel orientation is evident with the increase of the shear rate through $\dot{\gamma}_c$ in the x-phase (Figure 5.7).

5.4.2.b. Effect of Thermal History

As Phase X shows significant thermal hysteresis according to powder X-ray diffraction (Section 5.3.1), it is instructive to examine how this hysteresis influences the development of perpendicular orientation in Phase X. Two *in situ* WAXS experiments were performed at a shear rate of 0.1 s^{-1} ($\dot{\gamma} < \dot{\gamma}_c$) and a temperature of 110°C in the x-phase, but with different thermal histories: (a) directly heating the sample from room temperature into the x-phase followed by 30 minutes of thermal equilibration; (b) heating the sample to the isotropic state and then cooling it into the x-phase and holding it there for 30 minutes. In both cases, the initial condition shows some anisotropy ($S \neq 0$). This appears to be specific to the x-phase; a quiescent sample cooled from the isotropic state into the nematic phase shows no measurable anisotropy in WAXS.

The above two experimental protocols led to quite different orientation responses in the x-phase, as shown in Figure 5.8. For case (a), upon flow start up, the net orientation oscillates between -0.15 and -0.05, and it stays at a low value ($S = -0.05$) up to 200 s.u. of steady shear. The diffraction pattern actually seemed to approach an isotropic ring. This does not apply to case (b), where perpendicular orientation developed gradually toward the steady state. The final orientational parameter reaches a value close to -0.2, a much stronger perpendicular orientation compared to that for case (a). As shown in the previous section, powder diffraction data showed that the sample may contain some residual order in the x-phase when directly heated from room temperature into the x-phase. We believe that this residual order may explain the significant structural hysteresis phenomena on orientation development during steady shear.

5.4.2.c. Regimes of Parallel and Perpendicular Orientations

To establish the conditions that lead to the parallel and the perpendicular orientations, extensive *in situ* flow-X-ray experiments were conducted in both the nematic and x-phase to map out the steady-state orientation as a function of temperature and shear rate. In

the nematic phase, only the parallel orientation was observed (Figure 5.6). The degree of orientational order depends very weakly on the applied shear rate and the temperature except in the vicinity of T_{xn} and T_{ni}. In the x-phase, there are two orientation states competing with each other, as described above. The critical shear rate $\dot{\gamma}_c$ decreases with temperature and approaches zero at 120°C. By plotting data from our entire matrix of experiments, a mapping diagram was constructed, showing the locations of the parallel and perpendicular alignment regimes in $T - \dot{\gamma}$ space (Figure 5.9). Three typical WAXD patterns are also included in Figure 5.9, representative of the isotropic phase, the parallel-oriented nematic and the perpendicular-oriented x-phase.

5.4.3 Orientation Flipping by Steady Shear

We have examined the evolution of molecular orientation after a jump in either temperature or shear rate from one alignment regime to the other. Three transients designed to flip the orientation were investigated; (1) fast cooling into the x-phase (130 $\rightarrow$ 110°C, at 0.1 s^{-1}); (2) fast heating out of the x-phase (110 $\rightarrow$ 130°C, at 0.1 s^{-1}); (3) stepping shear rate down from $\dot{\gamma} > \dot{\gamma}_c$ to $\dot{\gamma} < \dot{\gamma}_c$ in the x-phase (from 3 s^{-1} to 0.1 s^{-1}, at 110°C), as shown in Figure 5.10. A temperature jump from the x-phase to the nematic phase produces a sudden change of orientation from perpendicular to parallel in less than 2 strain units, followed by a more gradual perfection of parallel alignment during prolonged shear. Both a rapid cooling into the x-phase and a step down in shear rate in the x-phase induced an almost identical response in the material as the orientation changed from parallel to perpendicular.

The flip of orientation by step change of the shear rate leads to a different trajectory of the stress evolution from the case of no orientational flipping. When stepping up the shear rate within perpendicular alignment regime (0.1 $\rightarrow$ 0.2 s^{-1}, Figure 5.11a), the shear stress shows a tiny overshoot peak, and then quickly settles to a new steady state. This is not surprising since the increase of shear rate only slightly alters the degree of perpendicular alignment. In a different situation, when the shear rate is stepped up from perpendicular alignment regime to parallel alignment regime, a much larger stress overshoot is observed, corresponding to flipping of the director orientation from the vorticity direction to flow direction (Figure 5.9).

Upon stepping down the shear rate, the transient stress response with orientational flipping also differs from the case of no orientational flipping. The step down of the shear

rate within the perpendicular alignment regime induces a small undershoot before reaching to a new steady state (Figure 5.11b). This is similar to the case of step up. However, when stepping down the shear rate from parallel alignment regime to perpendicular alignment regime, the shear stress shows significant multiple oscillations before arriving to its steady state (Figure 5.11b). It is worth pointing out that these multiple stress oscillations are not a result of tumbling nematic dynamics; instead they are probably due to some orientation fluctuations when domains attempt to flip from the flow direction to the vorticity direction.

5.5 Oscillatory Shear Alignment

Macroscopic alignment can also be induced by large amplitude oscillatory shear in Phase X. The oscillatory frequency determines whether parallel alignment or perpendicular alignment is dominant, while the oscillatory strain amplitude governs the details of the progress towards the aligned state.

The type and the quality of oscillatory shear alignment were measured by *in situ* wide angle X-ray scattering using the Linkam shear cell. Since WAXS orientation patterns are quite complex and sometimes even slightly skewed (e.g., Figure 5.15), the use of orientation parameter S (Eq. 3.1) is no longer appropriate to describe shear-induced molecular anisotropy. Following the same approach adopted by Cinader and Burghardt in quantifying bimodal orientational anisotropy [6], an anisotropy factor (AF) may be defined to quantify the degree of anisotropy by computing the difference in the eigenvalues of the second moment tensor $\langle \mathbf{kk} \rangle$, where

$$\langle \mathbf{kk} \rangle = \begin{bmatrix} \langle k_1 k_1 \rangle & \langle k_1 k_2 \rangle \\ \langle k_1 k_2 \rangle & \langle k_2 k_2 \rangle \end{bmatrix} \equiv \begin{bmatrix} \langle \cos^2\beta \rangle & \langle \sin\beta\cos\beta \rangle \\ \langle \sin\beta\cos\beta \rangle & \langle \sin^2\beta \rangle \end{bmatrix}. \tag{5.1}$$

In this expression, $\mathbf{k} = (k_1, k_2) = (\cos\beta, \sin\beta)$ is a unit vector representing a point on the azimuthal scan of X-ray pattern (β is the azimuthal angle measured with respect to the flow direction), and $\langle \cdots \rangle$ represents an average weighted by the azimuthal intensity scan. It is important to recognize that large positive value of anisotropy factor means preferential alignment along the flow direction ($AF = 1$ is perfect alignment along the flow direction), whereas large negative values of anisotropy factor means predominant alignment the vorticity direction ($AF = -1$ is perfect alignment along the vorticity direction).

5.5.1 Selection of Alignment Trajectory by Varying Frequency

The evolution of molecular orientation depends on the applied oscillatory frequency: high frequency leads to preferentially parallel alignment (along the flow direction), while low frequency results in predominantly perpendicular alignment (along the vorticity direction). Regimes of parallel and perpendicular alignment under oscillatory shear have been mapped in Figure 5.9. At low frequency ($\omega = 0.5$ rad/s) where perpendicular orientation is dominant, the anisotropy factor, albeit slightly positive before shear due to thermal history, drops immediately below zero after a few cycles of oscillation (Figure 5.12a). Prolonged oscillatory shearing leads to a further drop in the magnitude of anisotropy factor in the direction towards better perpendicular orientation. The orientation response is very different at high frequency ($\omega = 50$ rad/s) where parallel orientation is dominant. The value of anisotropy factor is always positive, showing a continuous increase towards a high degree of parallel alignment during shear (Figure 5.12a). The anisotropy factor (at $\omega = 50$ rad/s) saturates after about 500 sec oscillation, roughly corresponding to 4000 cycles of oscillation.

The oscillatory shear-induced alignment is also manifested in bulk rheological properties. A decrease in the complex viscosity $|\eta^*|$ is observed during oscillatory shear at both low and high frequency (Figure 5.12b), suggesting some macroscopic alignment. The drop in $|\eta^*|$ is more significant for high frequency shear. This is not surprising since 8000 cycles (i.e., 1000 sec) of oscillation at $\omega = 50$ rad/s has induced a higher degree of alignment, as opposed to a lower degree of alignment obtained at $\omega = 0.5$ rad/s after the same shearing time (only 80 cycles).

5.5.2 Role of Oscillatory Strain in Alignment Process

The oscillatory strain amplitude γ_0 determines how fast molecular alignment may develop under oscillatory shear. Here we only present data obtained at the frequency that induces perpendicular alignment (i.e., $AF < 0$). As shown in Figure 5.13, the anisotropy factor drops much quicker with increasing γ_0 (Figure 5.13), corresponding to a faster alignment process at larger γ_0. It appears that the final degree of molecular alignment is also higher for larger γ_0. These results suggest that oscillatory shear alignment is a strong function of both oscillatory frequency and strain amplitude.

5.5.3 Orientation Flipping by Oscillatory Shear

Recall from Section 5.4.3 that perpendicular and parallel orientation can be flipped reversible by step change of temperature or shear rate, it is interesting to examine whether or not oscillatory shear can flip the orientation from parallel to perpendicular or vice versa. As a result, we have performed a series of orientational flipping attempts in the x-phase under oscillatory shear. The first transient designed to flip the orientation involves a temperature jump from the nematic phase (140°C) to x-phase (110°C) while continuously shearing at a frequency of 0.5 rad/s and strain of 150%. Upon this temperature jump, the anisotropy factor starts from a positive value, corresponding to the initial state of parallel alignment, then shows an immediate overshoot after temperature jump, followed by a gradual decrease over the remaining oscillatory shear (Figure 5.14). It takes about 500 sec, that is approximately 40 cycles, to complete the flipping from parallel alignment to perpendicular alignment. Further oscillation leads to an enhanced degree of perpendicular alignment, but the final quality of alignment is not as good as that aligned from random polydomain state (Figure 5.14). The overshoot during the evolution of anisotropy factor is a little bit strange and probably arises from a slow temperature response during temperature jump; consequently, the sample at that time (100 sec) is still within the nematic phase, but with a higher order parameter due to larger undercooling.

The second transient designed to flip the orientation involves the change of shear mode. The sample was presheared to a steady state parallel alignment at a shear rate of 2 s^{-1} at 110°C, followed by oscillatory shear at a frequency of 0.5 rad/s and strain of 150%. As shown in Figure 5.15, the anisotropic factor drops immediately after switching steady shear to oscillatory shear, signaling a tendency of flipping orientation from parallel to perpendicular. However, the flipping of orientation from parallel to perpendicular is frustrated after about 700 sec of oscillation, and the anisotropic factor ceases to drop and remains at a value slightly above zero. In fact, the attempt of flipping molecules from parallel to perpendicular orientation is very obvious from the X-ray scattering patterns, yet somehow molecular orientation is "locked-in" at some intermediate states between parallel and perpendicular alignment (Figure 5.15). These results are very different from the orientational flipping under steady shear which is reversible in response to step change of shear rate and/or temperature.

5.6 Effect of Orientation on Linear Viscoelasticity

To examine the effect of alignment on linear viscoelastic properties, we prepared preferentially parallel, preferentially perpendicular and unaligned samples. Orientation was achieved by preshearing the sample at selected shear rates in the nematic or x-phase. Details of the shear and thermal histories for different orientation states are summarized in the caption of Figure 5.16. In the nematic phase, parallel-oriented samples were prepared in two different ways ("Parallel I," directly shearing in the nematic phase; "Parallel II," shearing at a high rate in the x-phase and then heating into the nematic phase) and perpendicular oriented samples were prepared by shearing at low rate in the x-phase, then heating into the nematic phase [7]. Analogously, measurements in the x-phase were performed right after steady preshearing for Parallel II and Perpendicular, and after rapidly cooling into the x-phase for Parallel I. Five minutes was allowed for thermal equilibration after a temperature jump.

The dynamic moduli in the nematic phase showed a characteristic frequency (at $\omega_c \approx$ 60 rad/s), above which G' (and G'', not shown here) is insensitive to the state of alignment; and below which the dynamic moduli for both parallel- and perpendicular-aligned samples are low relative to those for the unaligned state (Figure 5.16a). The dynamic moduli of two parallel aligned states induced in different ways (presheared at 140°C and at 110°C) are nearly the same throughout the whole frequency range, whereas the dynamic modulus of the perpendicular-aligned state falls between those of the unaligned and parallel-aligned states. We conclude that the microstructure of two parallel-aligned samples in the nematic phase are very similar regardless of their exact thermal history.

The x-phase showed qualitatively different behavior from that of the nematic phase (Figure 5.16b). Most notably, the storage modulus of the parallel-aligned sample was the highest of the three states (Parallel I≈Parallel II>Unaligned>Perpendicular) for the x-phase, while this orientation state had the lowest modulus of the three for the nematic phase. The storage modulus of the unaligned sample lies between parallel and perpendicular-aligned states, in contrast to having the highest G' in the nematic phase. The implications of this change in relative order of G' with orientation will be discussed in Section 5.7.

5.7 Discussion

5.7.1 Elusive Nature of Phase X

Main chain LCPs with alternating mesogen and spacer structure can exhibit a variety of distinct liquid crystalline phases. The two different types of sequence (i.e., flexible spacer vs. rigid mesogen) may segregate from each other to form layers normal to the chains, giving rise to smecticity. The exact nature of layer ordering in main-chain LCPs, however, depends on the details of molecular architecture. For example, the reported smectic ordering includes smectic C in $OQ_{OE}O$-10 (Figure 1.5) [8], cybotactic (poorly ordered smectic) in DDA-9 (Figure 1.5) [9], smectic C_2 (i.e., biaxial smectic C) in yet another mesogen-spacer type LCP [10].

Difficulties are encountered to assign the x-phase of DHMS-7,9 to smectic. The transition from the nematic to the x-phase appears to involve a very local change in fluid structure, but one that must be very subtle. This phase transition is evident calorimetrically with a very small change in enthalpy (or perhaps heat capacity only; see Figure 3.1). The small hysteresis associated with the nematic-x transition on heating vs. cooling also indicates that this transition is very local and does not involve any significant chain rearrangement. The nature of the higher-order structure remains elusive, since no change in structure was detected by powder X-ray diffraction on cooling through T_{xn}. The small amount of higher order (weak peak at $q \approx 0.32$ Å^{-1}) observed on heating into the x-phase appears not to be crystalline, as the wide angle peak ($q \approx 1.65$ Å^{-1}) is gone even though the small angle peak persists (Figure 5.1c). The persistence of this small angle peak with increasing temperature suggests some kind of chain reorganization mechanism produced by crystallization, probably arising from a crystal-like repeat in the form of mesogen-spacer unit. Such a hypothetical chain reorganization is similar to the observed non-periodic sequence segregation in liquid crystalline random copolymers [11]. It must be emphasized again that the observed residual order on heating into the x-phase does not exist when the sample is cooled from the isotropic to the x-phase (Figure 5.1c).

The subtle structure in the x-phase has a profound effect on dynamics and shear orientation behavior. Prior diffusion measurements showed a dramatic decrease in diffusivity on moving from the nematic to the x-phase [1]. Our rheological results indicate a hundred-fold slowing down of the longest relaxation time (Figure 5.3a) and a corresponding jump

in the viscosity (Figure 5.2) at this phase transition. Texture coarsening also reflects this dramatic increase in viscosity: while the texture in the nematic phase ($T = 160°C$) coarsens significantly in two days, there is no visible coarsening in the x-phase even after 1 week. The rheo-X-ray results show a striking reversible change in the orientation in steady shear at low rates, flipping from parallel to perpendicular on cooling through T_{xn} and vice versa on heating through T_{xn}, described below. This type of orientational flipping can also be induced using large amplitude oscillatory shear by step changes of temperature or frequency.

In the x-phase, the viscosity curve shows predominantly shear thinning over the entire range of shear rate. The data display an approximate power-law relationship between η and $\dot{\gamma}$ with $\eta \sim \dot{\gamma}^{-0.56}$. This qualitative change in the shape of the flow curve with temperature across T_{xn} is reminiscent of changes reported in other thermotropic LCPs. For example, Wissbrun has studied a commercial thermotrope, where shear thinning was observed at low temperatures, a three-region flow curve was observed at intermediate temperatures, and more intriguingly flow curves with apparent shear-thickening were observed at even higher temperatures [12]. In the present system, the change in the shape of the flow curve is a consequence of the presence of an additional phase besides the nematic one; such complications may also occur in other thermotropes, leading to system-specific behavior due to the appearance of higher order structure (e.g., layered ordering, residual crystallinity, etc.).

The dependence of the first normal stress difference on shear rate is complicated in the x-phase: N_1 shows a local minimum with increasing shear rate. An explanation for this *shape* of $N_1(\dot{\gamma})$ has been offered for highly concentrated nematic solutions of rod-like polymers (HPC) [5]. However, it should be noted that DHMS-7,9 does *not* show this behavior in its nematic phase – only in the poorly defined mesophase at lower temperature. The change in liquid crystalline order appears to be a prerequisite for the development of the local minimum in $N_1(\dot{\gamma})$ in this system. The precise structural origin of this behavior is not yet known, but it almost certainly relates to the distinctive orientational behavior observed during steady shear in the x-phase.

The most striking feature in the x-phase is the observation that two distinctive orientation states can be achieved during steady shear, depending on the applied shear rate. The transition between the parallel and perpendicular orientations observed by *in situ* WAXS agrees with neutron scattering observations of chain anisotropy in DHMS-7,9 by Dadmun

and coworkers [13]. This type of orientational flipping has been reported in two other liquid crystalline polymers: a concentrated solution of PBG and an HBA-HNA thermotropic copolyester (Vectra A900) [14, 15]. In both of these systems, like DHMS-7,9, this phenomenon occurred at the lower limit of the nematic temperature range. In PBG, flipping was observed just above its gelation point. In HBA-HNA, it occurred in conjunction with flow-induced crystallization; after the onset of crystallization, the orientation was almost no longer reversible from parallel to perpendicular (but not vice versa) in that system. In DHMS-7,9, residual order also has some impact on the subsequent development of orientation: samples cooled into the x-phase from T_{ni} flip reversibly, whereas samples heated into the x-phase from room temperature (containing some residual order) oriented weakly under shear; thus, the residual order seems to inhibit the process of orientation development (Figure 5.8).

The theoretical background for understanding orientational flipping in LCPs is based on models of rod-like nematics [16]. However, the experimental systems which provide the closest realization of the rod-like model (e.g., PBG in *m*-cresol) do not exhibit flipping in the nematic phase. On the other hand, all the systems that do show flipping are complicated by higher-than-nematic order structure. Indeed, in the case of PBG solutions and the x-phase of DHMS-7,9, the nature of the higher order structure is not yet known. Further understanding of these more complex structures and their role on the flow-induced orientation is needed.

5.7.2 A Working Hypothesis for Orientational Flipping

Some of the rheological characteristics of the x-phase are reminiscent of those of lamellar block copolymers or smectic LCPs. The dynamic modulus is strongly enhanced at low frequency for the x-phase relative to the the nematic phase (Figure 5.3b). Other systems show such a qualitative change when they self-assemble into a nanostructure which contributes slow relaxation modes [17, 8]. The relative magnitudes of the storage moduli of the parallel, perpendicular and unaligned orientation states in the x-phase are like those of layered fluids [17], and their relative magnitudes changed to those expected for a nematic at $T > T_{xn}$. If we consider the possibility that there were some subtle smectic-like order in the x-phase, then we would expect parallel alignment to show a relatively high modulus and perpendicular alignment to give a relatively low modulus (see Figure 5.17b and the caption; note that the definition of "parallel" here differs from the convention in lamellar block

copolymers). For layered fluids, unaligned state is expected to have a modulus intermediate between these two aligned states. This ordering of the storage moduli is observed when the respective aligned samples are characterized within the x-phase (Figure 5.16b). The relative ordering for the dynamic modulus expected for the nematic phase is different, since it is minimized when the director is along the flow direction (Figure 5.17a). For a nematic, the unaligned state is expected to have a higher modulus than either parallel or perpendicular aligned states. Indeed when samples of each type of orientation are characterized in the nematic phase, the relative values of the moduli are in accord with expectations (Figure 5.16a).

The phase behavior and oscillatory shear alignment of DHMS-7,9 in the x-phase is very similar to smectic layered LCPs. Like the nematic-to-X transition in DHMS-7,9, a smectic LCP called $OQ_{OE}O$-10 shows a similar slowing down in relaxation and enhancement in the storage modulus at low frequency on cooling through the nematic-smectic transition [8, 18]. In relation to orientation flipping, $OQ_{OE}O$-10 shows strong perpendicular alignment in oscillatory shear at high frequency and/or high strain amplitude, and very weak parallel alignment at low to moderate frequency and low strain amplitude. These observations are also qualitatively similar to that of DHMS-7,9 in Phase X. The stability of the perpendicular alignment in smectic liquid crystal (e.g., 8CB) is believed to result from minimizing the distortion of both the molecular director and the layered structures [3]. Taken the known smectic character of OQ $_{rmOE}$O-10 and some circumstantial evidence of layered ordering in DHMS-7,9, the same mechanism may apply to the observed perpendicular alignment in polymeric smectics as well. However, since mesogens along the same chain can reside in different layers, the chain connectivity might frustrate the stability of perpendicular alignment, resulting in a much narrower stability alignment regime for polymeric layered fluids.

Orientation flipping under steady shear in Phase X of DHMS-7,9 could be explained by a similar mechanism if we hypothesize that the higher order structure of the x-phase is not only subtle, but also delicate. When the shear rate is below a critical value, the integrity of this order is maintained. If this higher order structure is lamellar, Safinya's explanation for the tendency toward perpendicular orientation would apply. When the shear rate is large enough to disrupt the higher order structure, the behavior reverts to that of the nematic, in which only parallel orientation was induced under shear. This hypothesis is consistent with

the observed temperature dependence of critical shear rate in the x-phase: as temperature increases, the correlation between higher order structures presumably weakens, and as a consequence, the critical shear rate to disrupt such structures decreases.

Rather than an abrupt loss of x-phase order at the critical shear rate $\dot{\gamma}_c$, the continuous variation of η and N_1 across $\dot{\gamma}_c$ (Figure 5.5) suggests a progressive erosion of the higher order structure. It appears that the x-phase structure gives rise to the high values of η and N_1 at $\dot{\gamma} < \dot{\gamma}_c$, and the gradual destruction of the higher order structure causes η and N_1 to drop. In particular, N_1 falls to a level consistent with the nematic phase as $\dot{\gamma}$ reaches 20 s^{-1} at 110°C. With further increase in $\dot{\gamma}$, N_1 rises in a manner similar to the nematic phase (Figure 3.3), consistent with steady state values of S approaching those of the nematic phase (at 110°, Figure 5.7).

5.8 Conclusion

DHMS-7,9 shows a distinct liquid crystalline phase between crystalline solid and nematic phase. Although viscoelastic behavior suggests certain rheological similarity to behavior of layered fluids, there is no direct evidence from X-ray diffraction for the exact mesophase ordering. The striking orientational flipping is certainly related to the higher order present in the x-phase, yet residual order associated with crystallinity appears not to be the cause of this orientational flipping; indeed, residual structure inhibits the perpendicular alignment process in materials heated into the x-phase.

a.

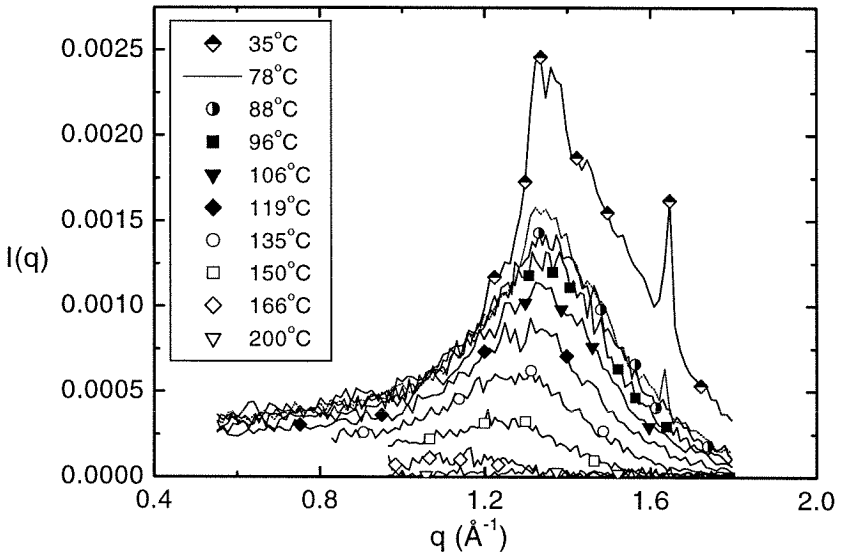

b.

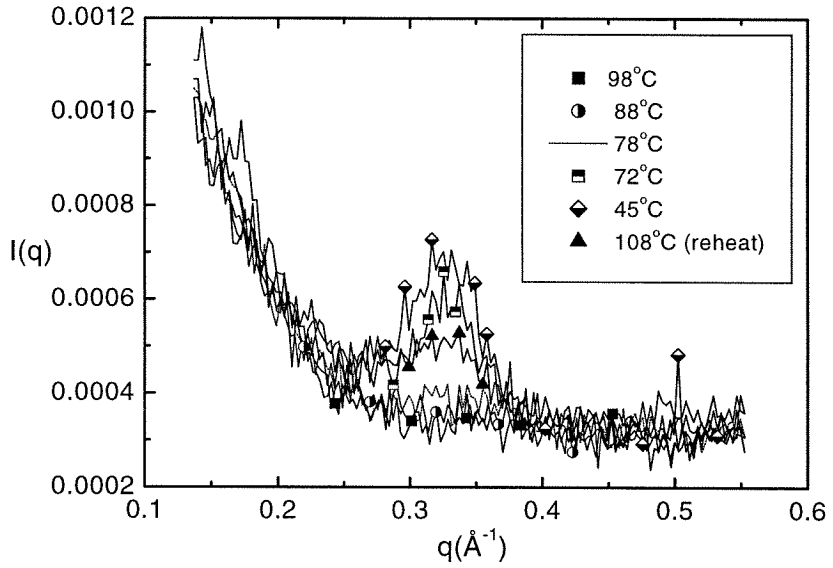

Figure 5.1: Powder X-ray diffraction intensity $I(q)$ vs. q of DHMS-7,9 ($M_w = 28440$ g/mol) at different temperatures. (a) cooling runs at large q; (b) cooling runs at small q, including a reheat run from room temperature at 108°C.

c.

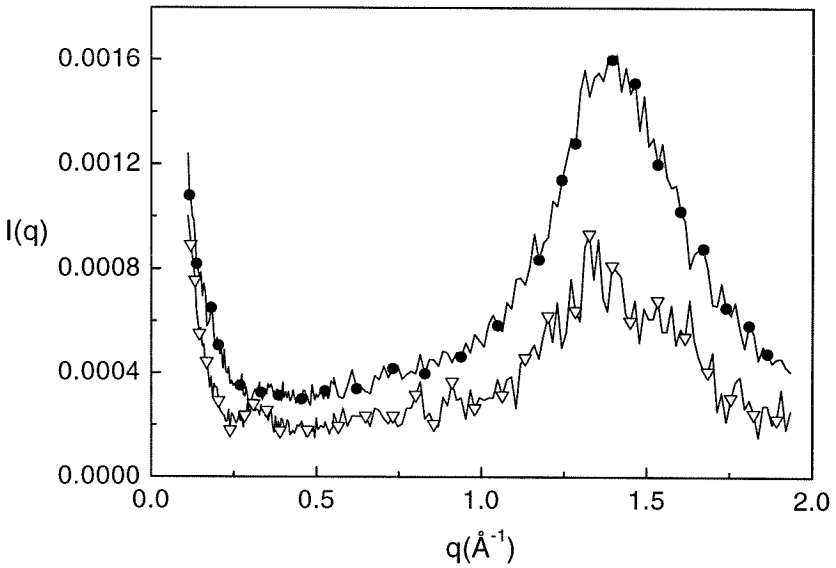

Figure 5.1 (continued): (c) a heating run [▽] from room temperature at 111°C, and a cooling run [•] at 99°C with annealing for 24 h.

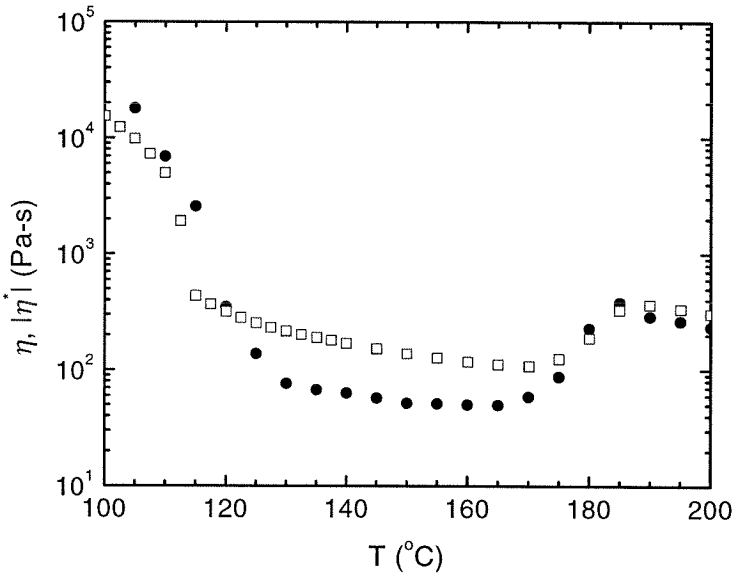

Figure 5.2: Apparent shear viscosity versus temperature: steady shear viscosity η [•] was obtained at a rim shear rate of 0.1 s^{-1}; while complex viscosity $|\eta^*|$ [□] data was measured at a frequency of 5 rad/s and a rim strain amplitude of 5%. Both measurements were conducted on 50 mm parallel plates with a 1 mm gap thickness.

a.

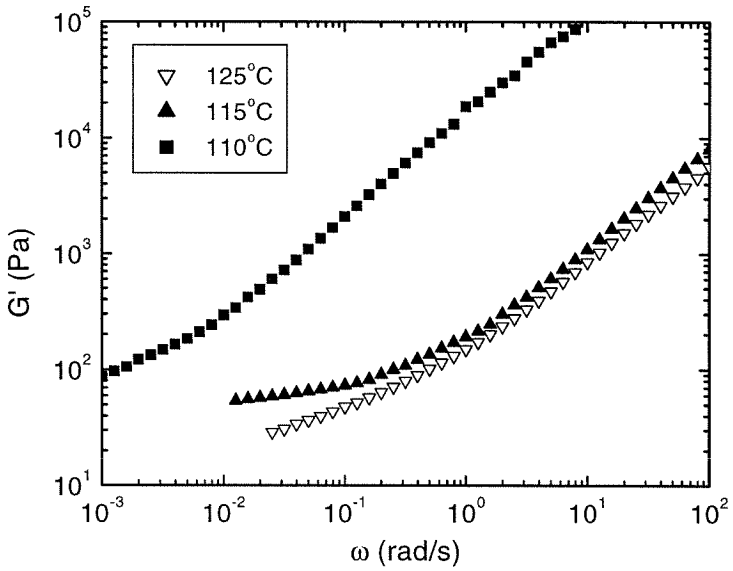

b.

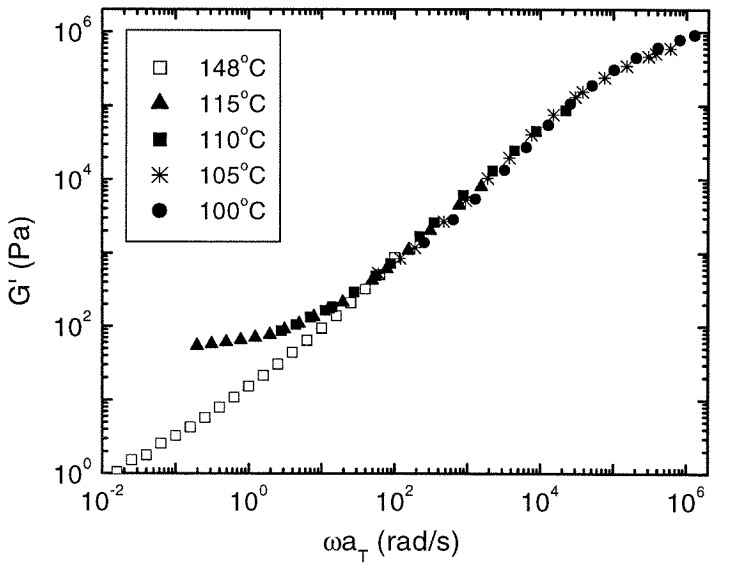

Figure 5.3: Storage modulus as a function of frequency in Phase X of 28K DHMS-7,9. (a) in the vicinity of nematic-x phase transition; (b) in the x-phase (with nematic phase data at $T = 148°C$ for comparison). In part (b), measurements at different temperatures have been shifted along the frequency axis alone to achieve approximate superposition at high frequency.

a.

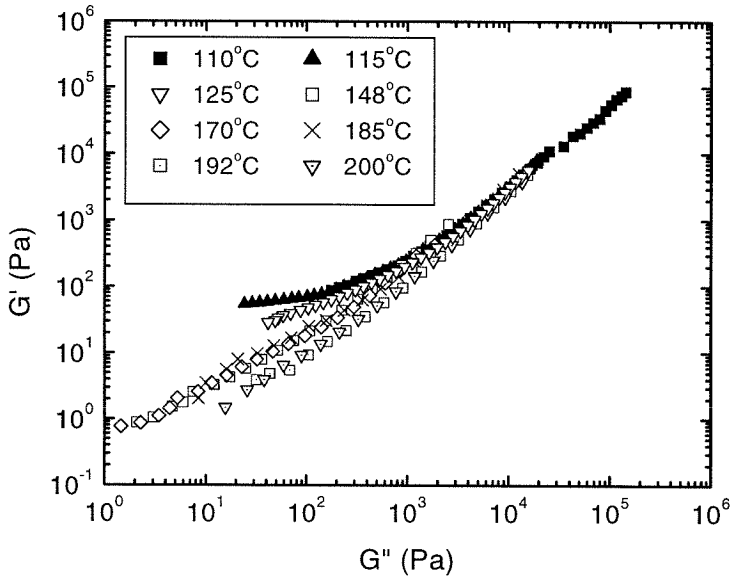

b.

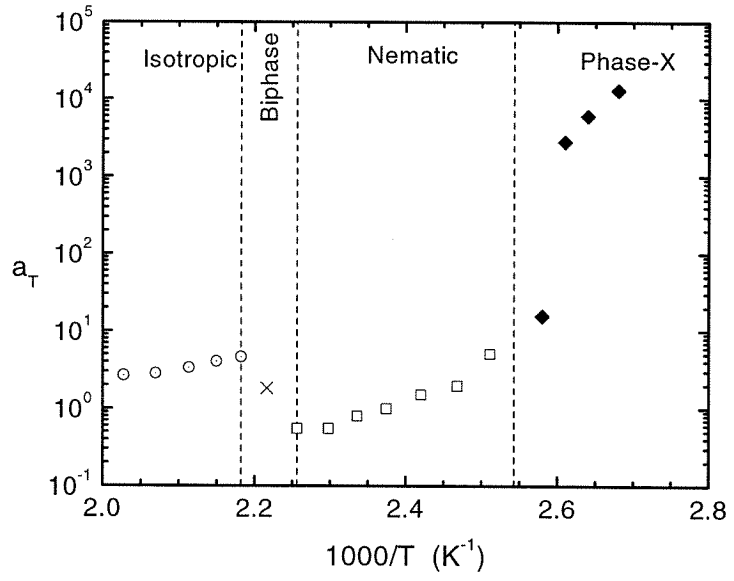

Figure 5.4: (a) Cole-Cole plots (logG' vs. logG'') at different temperatures; (b) Shift factors vs. $1000/T$ in the isotropic, nematic and x-phase (reference temperature $T_{ref} = 148°C$).

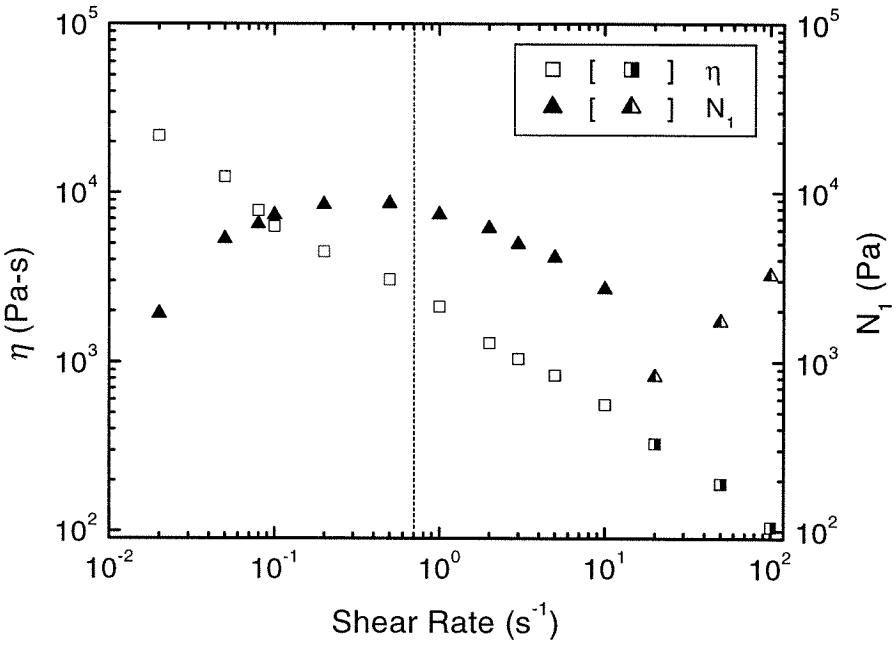

Figure 5.5: Steady shear viscosity and first normal stress difference as a function of shear rate at 110°C. The half-filled square and triangle ($\dot{\gamma} > 10\ s^{-1}$) indicate apparent η and N_1 under conditions of mild edge fracture. Vertical lines indicates $\dot{\gamma}_c$ at 110°C (see text and Figure 5.7).

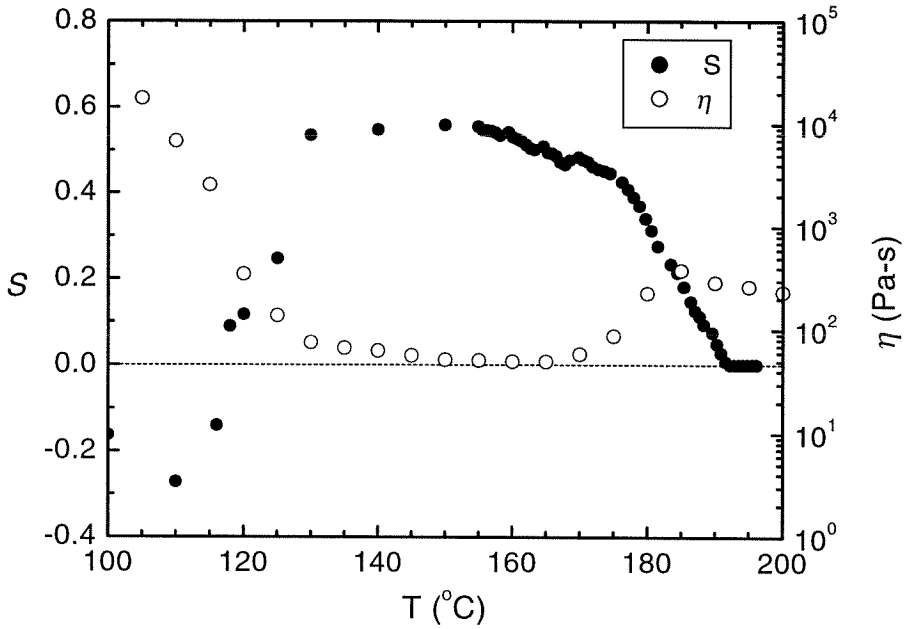

Figure 5.6: 2-D orientation parameter S [•] (data from Ugaz and Burghardt) and apparent shear viscosity [○] as a function of temperature at a single shear rate (0.1 s^{-1}). Negative values of S are used to represent data with the vorticity direction as the azimuthal coordinate. At least 150 s.u. preshear was applied to the sample to achieve steady state before data collection.

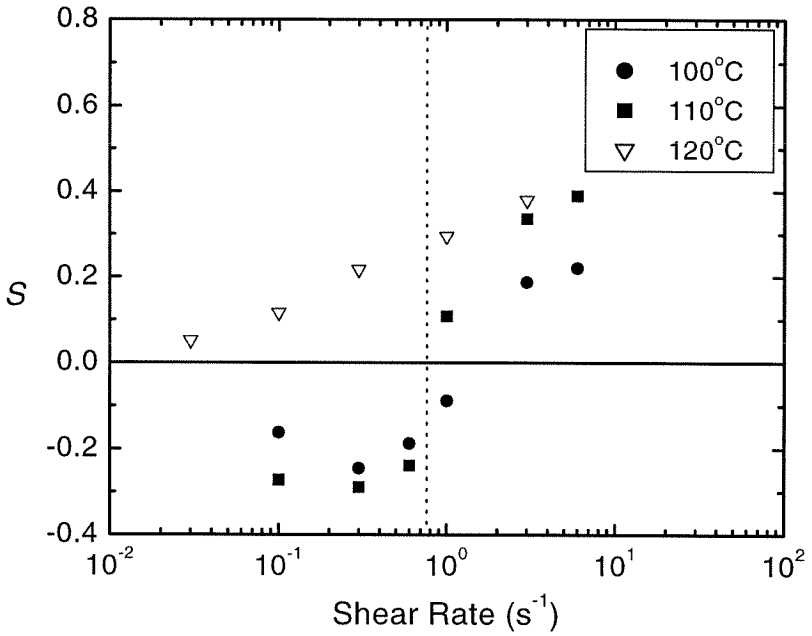

Figure 5.7: Orientation parameter as a function of shear rate at different temperature in Phase X. Negative values are used to represent data with the vorticity direction as the azimuthal coordinate. The vertical dot line indicates the critical shear rate at 110°C, below which perpendicular alignment is dominant, and above which parallel alignment is preferred (data from Ugaz and Burghardt).

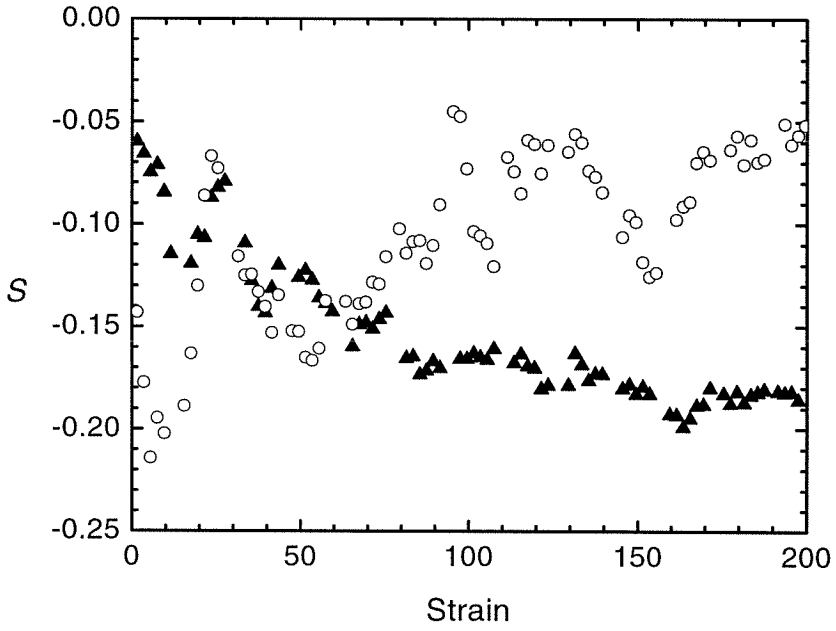

Figure 5.8: Effect of thermal history (residual order) on the stability of perpendicular alignment in the x-phase of 28K DHMS-7,9: (a) sheared after cooling from the isotropic state to 110°C [o]; (b) sheared after heating from room temperature to 110°C [solid triangle]. In both cases, the sample was subjected to steady shear at a shear rate of 0.1 s^{-1} ($\dot{\gamma} < \dot{\gamma}_c$) (data from Ugaz and Burghardt).

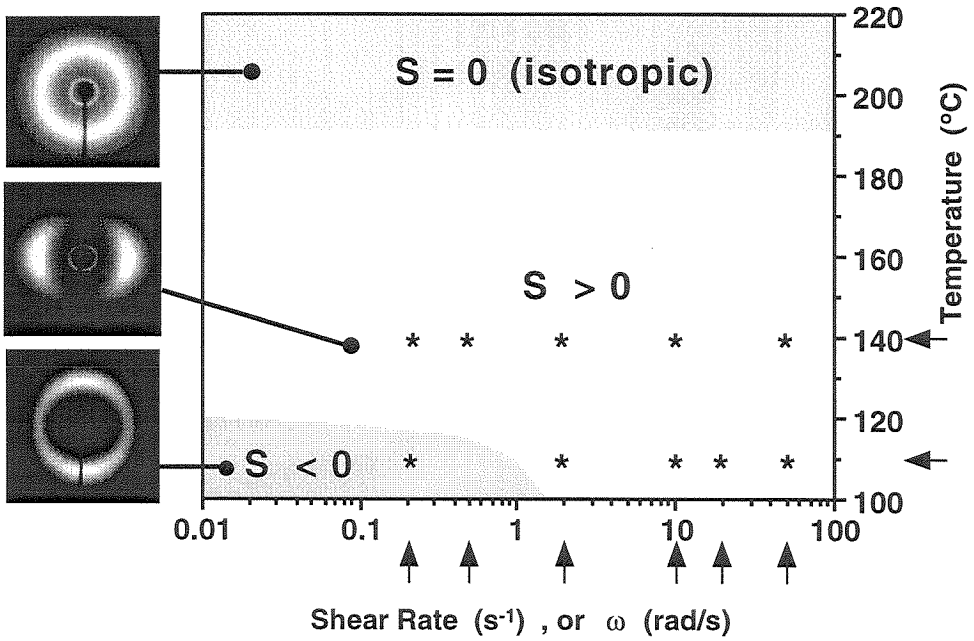

Figure 5.9: Mapping diagram of molecular orientation (S) in temperature-shear rate space (M_w = 28440 g/mol). Three representative diffraction patterns are also shown for the isotropic phase (no net alignment), parallel-aligned nematic and perpendicular-aligned x-phase, from top to bottom. A very similar orientational flipping was also observed using large amplitude oscillatory shear, and the asterisks indicate the selected oscillation frequencies we have studied.

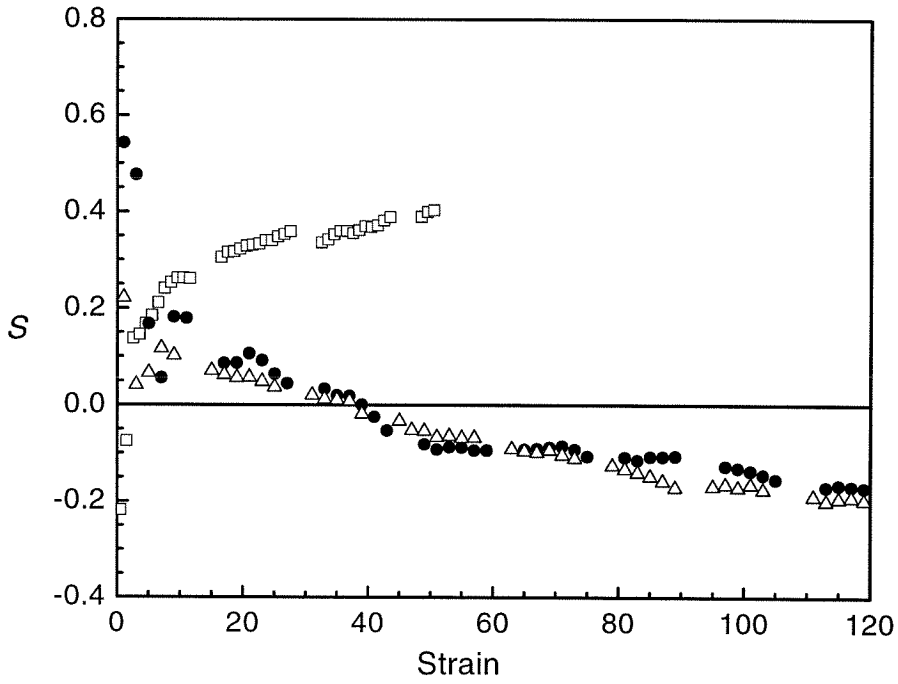

Figure 5.10: Evolution of orientation parameter as a function of strain during three attempts to flip orientation from parallel to perpendicular, or vice versa: heating from 110 to 130°C at 20°C/min and a shear rate of 0.1 s^{-1} [□]; quenching from 130 to 110°C at 20°C/min and a shear rate of 0.1 s^{-1} [•]; and a step down in shear rate from 3 to 0.1 s^{-1} at 110°C [△] (data from Ugaz and Burghardt).

a.

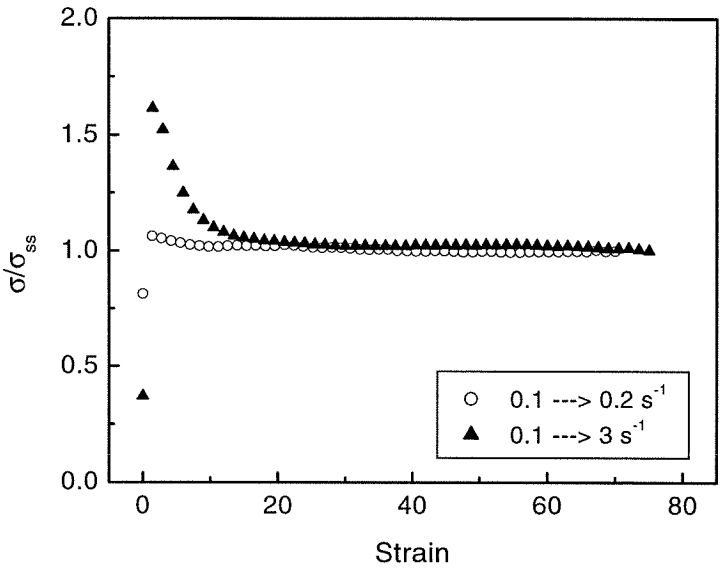

b.

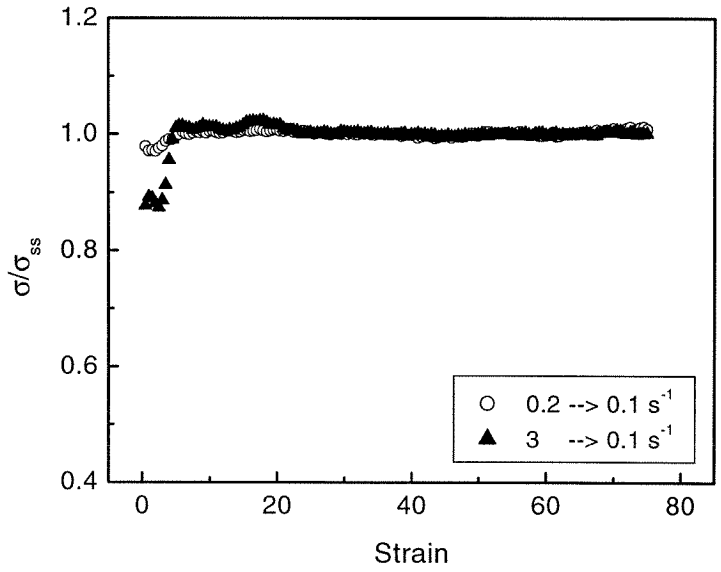

Figure 5.11: (a) Evolution of the normalized shear stress in response to a step up change of shear rate from 0.1 to 0.2 s^{-1} (both shear rates are within perpendicular alignment regime) and 0.1 to 3 s^{-1} at 110°C (perpendicular→parallel). (b) Evolution of the normalized shear stress after a step down change of shear rate from 0.2 to 0.1 s^{-1} (both shear rates are within perpendicular alignment regime) and 3 to 0.1 s^{-1} at 110°C (parallel→perpendicular).

a.

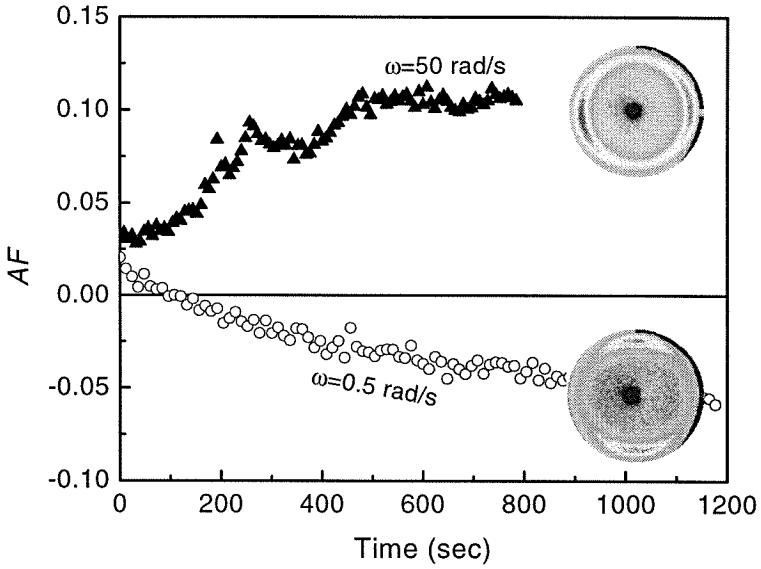

b.

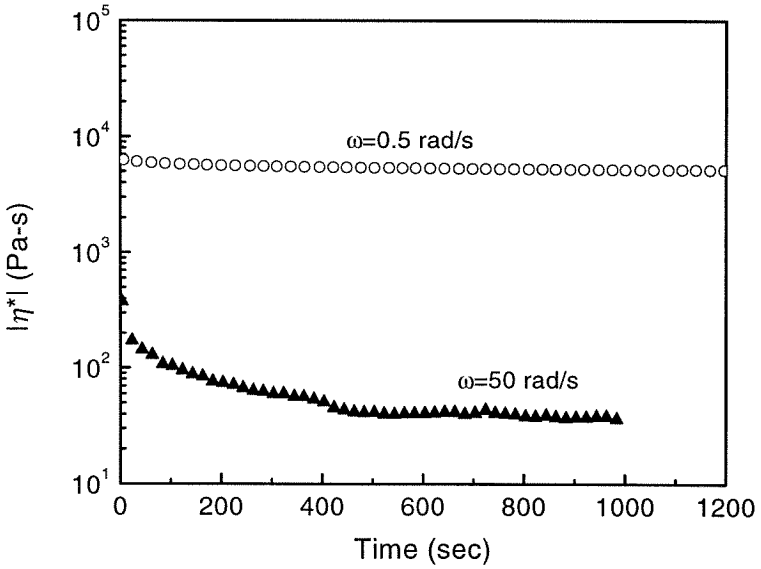

Figure 5.12: (a) Evolution of anisotropic factor (AF) during large amplitude oscillatory shear alignment at strain of 50% and frequency of 50 rad/s [solid triangle] and 0.5 rad/s [o] at 110°C (data from Vaish and Burghardt). (b) The corresponding evolution of the complex viscosity during large amplitude oscillatory shear alignment at strain of 50% and frequency of 50 rad/s [solid triangle] and 0.5 rad/s [o] at 110°C. In part (a), two X-ray scattering patterns are included, representing parallel alignment and perpendicular alignment from the top to the bottom, respectively. The flow direction is vertical.

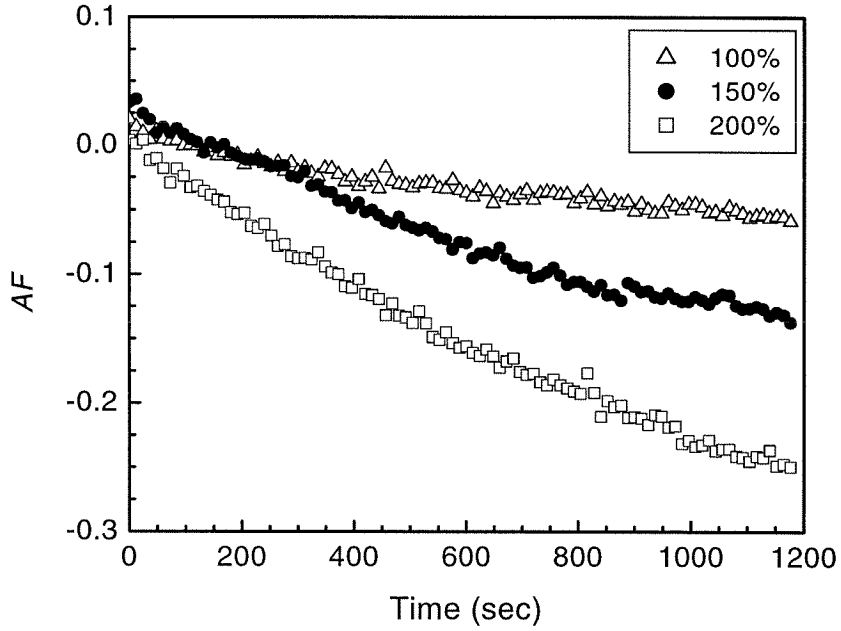

Figure 5.13: Evolution of anisotropic factor as a function of oscillation time during oscillatory shear alignment at a frequency of 0.5 rad/s and and strain amplitude of 100%, 150%, and 200%, demonstrating a higher degree of perpendicular alignment achieved at larger oscillatory strain (data from Vaish and Burghardt).

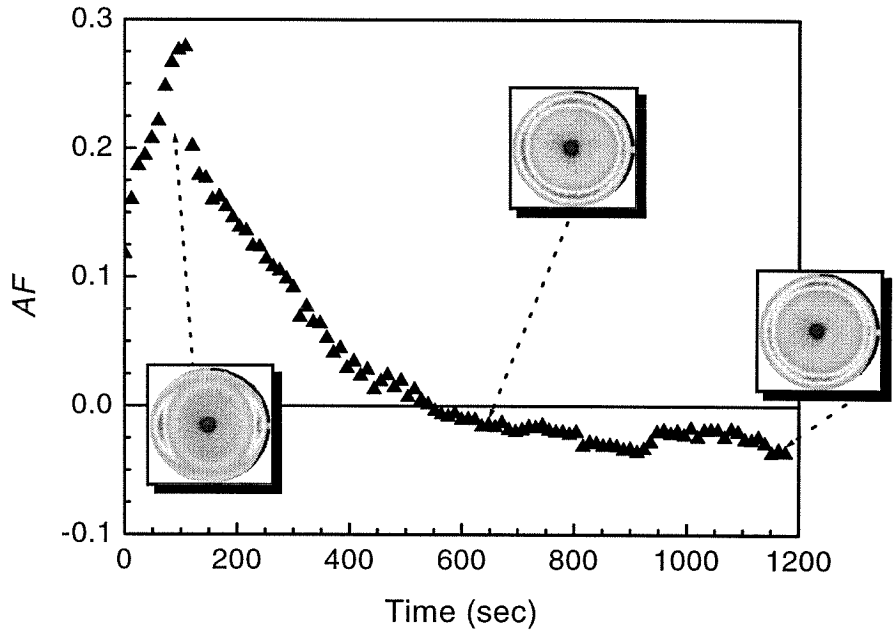

Figure 5.14: Evolution of anisotropic factor after a temperature jump from 140°C to 110°C during oscillatory shear at frequency of 0.5 rad/s and strain amplitude of 150% (data from Vaish and Burghardt).

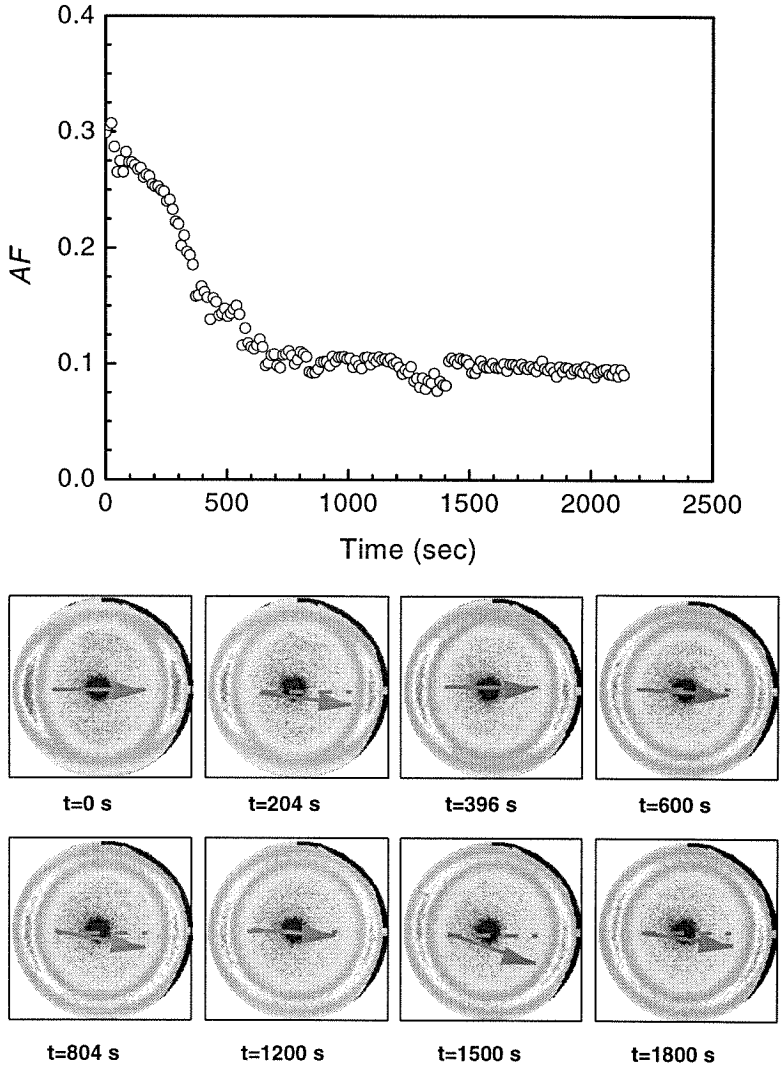

Figure 5.15: Evolution of anisotropic factor as a function of time after switching shear mode from steady shear at a shear rate of 2 s^{-1} to oscillatory shear at frequency of 0.5 rad/s and strain of 150%. At the bottom of the figure, several X-ray scattering patterns are included, showing the frustration of flipping orientation from parallel to perpendicular (data from Vaish and Burghardt).

a.

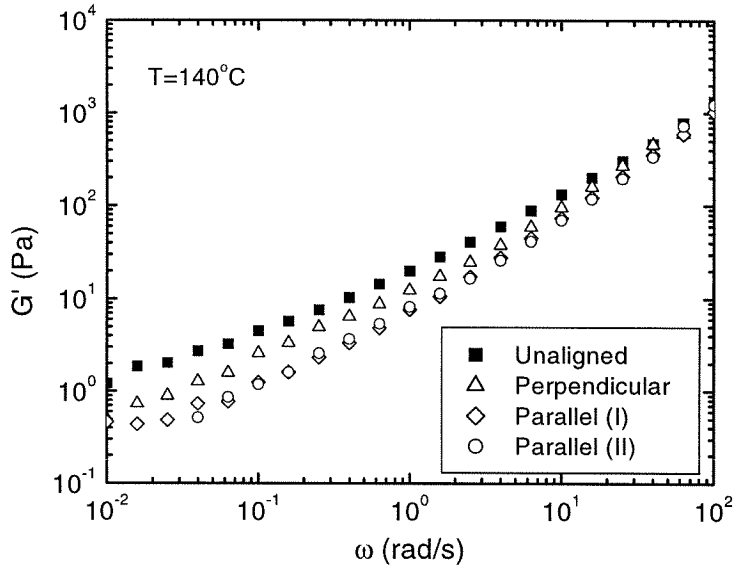

b.

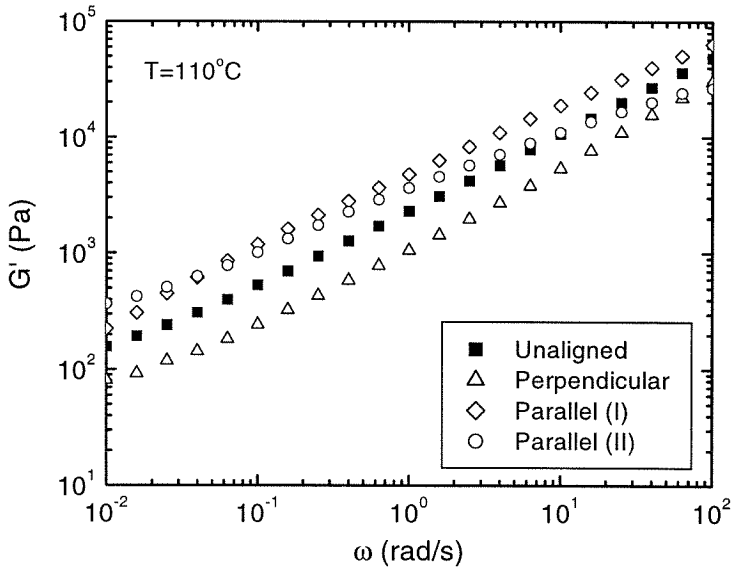

Figure 5.16: Effect of orientation on linear viscoelasticity behavior: (a) in the nematic phase at 140°C; (b) in the x-phase at 110°C. An unaligned sample was used as a reference. Two different paths of inducing parallel alignment were compared. Parallel (I): prealigned at 140°C at the shear rate of 3 s^{-1}. Parallel (II): prealigned at 110°C at the shear rate of 3 s^{-1}. Perpendicular: prealigned at 110°C at the shear rate of 0.1 s^{-1}.

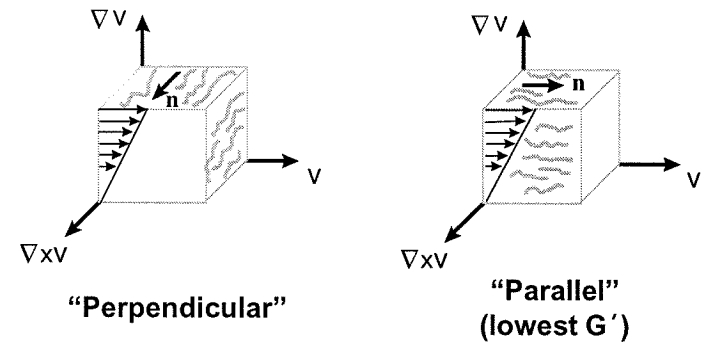

(a) Nematic Phase

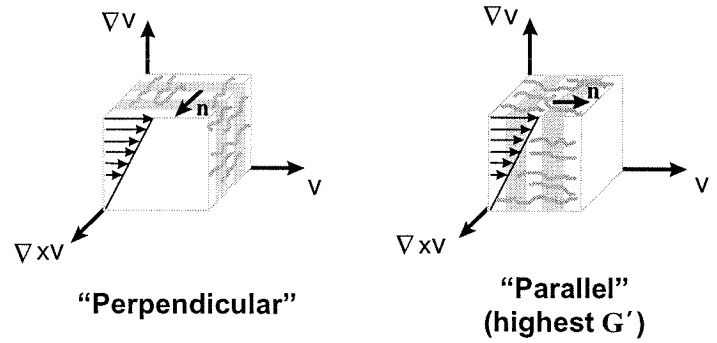

(b) A Layered Phase

Figure 5.17: Schematic illustration of a tentative mechanism to explain the observed viscoelastic behavior for unaligned, parallel and perpendicular orientation states: (a) nematic phase; (b) layered phase with lamellae on average normal to the chain axis. "Parallel" alignment corresponds to lamellae transverse to the flow; consequently, shear would distort this equilibrium layer spacing, resulting in a high modulus; "Perpendicular" alignment (director parallel to $\nabla \times \mathbf{v}$) corresponds to lamellae parallel to the flow plane ($\mathbf{v}$, $\nabla \mathbf{v}$-plane), so that this situation is not perturbed by shear even in the presence of fluctuations and the modulus would be relatively lower.

Bibliography

[1] E. Hall, C. K. Ober, E. J. Kramer, R. H. Colby, and J. R. Gillmor. *Macromolecules*, 26:3764, 1993.

[2] E.E. Hall, A. A. Robinson, S. G. McNames, C. K. Ober, and Y. S. Freidzon. *J. Mater. Sci.*, 30:2023, 1995.

[3] C. R. Safinya, E. B. Sirota, and R. Plano. *Phys. Rev. Lett.*, 66:1986, 1991.

[4] The layer spacing of 19.6 Å is approximately equal to the length of one mesogen-spacer repeating unit. The same value is used for estimation of contour length of polymer chains in the Discussion section.

[5] R. G. Larson S. G. Baek, J. J. Magda and S. D. Hudson. *J. Rheol.*, 38(5):1473, 1994.

[6] D. K. Cinader and W. R. Burghardt. *Polymer*, 40:4169, 1999.

[7] The *in situ* rheo-X-ray observation shows that shear induced orientation does not decay for at least 30 minutes in the nematic and x-phase. Thus, we assume the orientation obtained by steady preshearing in these experiments was maintained (at least qualitatively in terms of parallel vs. perpendicular) after the heating (or cooling) process and 5 minutes thermal equlibration at 140°C (or 110°C).

[8] S. D. Hudson, A. J. Lovinger, R. G. Larson, D. D. Davis, R. O. Garay, and K. Fujishiro. *Macromolecules*, 26:5643, 1993.

[9] A. Blumstein, S. Vilasagar, S. Ponrathnam, S. B. Clough, R. B. Blumstein, and G. Maret. *J. Poly. Sci. Poly. Phys.*, 20:877, 1982.

[10] J. Watanabe and S. Kinoshita. *J. Phys. II France*, 2:1237, 1992.

[11] S. Hanna, A. Romo-Uribe, and A. H. Windle. *Nature*, 366:546, 1993.

[12] K. F. Wissbrun. *British Polymer Journal*, 12:163, 1980.

[13] M. D. Dadmun, S. C. Clingman, C. K. Ober, and A. I. Nakatani. *J. Polym. Sci., Part B: Polym. Phys.*, 36:3017, 1998.

[14] M. D. Dadmun and C. C. Han. *Macromolecules*, 27:7522, 1994.

[15] A. Romo-Uribe and A. H. Windle. *Macromolecules*, 29:6246, 1996.

[16] R. G. Larson and H. C. Ottinger. *Macromolecules*, 24:6270, 1991.

[17] K. A. Koppi, M. Tirrell, F. S. Bates, K. Almdal, and R. H. Colby. *J. Phys. II France*, 2:1941, 1992.

[18] D. J. Alt, S. D. Hudson, R. O. Garay, and K. Fujishiro. *Macromolecules*, 28:1575, 1995.

Chapter 6 Concluding Remarks

In this work, we have applied various *in situ* structural probes to study the rheological behavior of a model thermotropic LCP. A main result has been the confirmation of flow-aligning behavior for mesogen-spacer type thermotrope. The quantitative determination of tumbling parameter as a function of order parameter provides the first opportunity to examine available molecular models, leading to a conclusion that flexible spacers between neighboring mesogens tend to frustrate tumbling motion because of chain connectivity. This is in direct contrast to rod-like lyotropic LCPs, for which director tumbling is the rule.

The tendency for flow-alignment in thermotropic LCPs has a profound impact on their flow behavior, resulting in simple and predictable stress and orientation response during shear flow. In steady shear, DHMS-7,9 exhibits high shear-induced orientation in the nematic phase that is nearly independent of shear rate, consistent with expectation for shear alignment. In transient shear, neither shear stress nor orientation parameter shows multiple oscillations due to the absence of director rotation. These qualitative features have been well captured by Ericksen polydomain model proposed by Ugaz and coworkers. Although there is no firm ground to neglect the distortional elasticity in Ericksen polydomain model, it is plausible that the effect of distortional elasticity diminishes for shear aligning nematics, since different domains tend to orient at the same Leslie alignment angle. The comprehensive set of results on DHMS-7,9—from the director response of monodomain to the flow behavior of polydomain, from bulk rheological properties to molecular orientation behavior, and from experimental data to computational simulation attempts, provide a strong foundation for interpreting the flow behavior of other thermotropic LCPs on the basis of shear alignment, particularly for those of mesogen-spacer type structure. We thus infer that the flexibility of mesogen-spacer type LCPs produces shear aligning behavior in general.

Within the scope of the present work, a major question remains to be answered with regard to the classification of shear aligning vs. director tumbling for commercial thermotropes. Those nematic chains only have limited flexibility arising from chain kinks, and the orientation of individual mesogen along the same chain is strongly coupled with each other. As a result, hydrodynamic torques might just rotate the entire chain as a slightly

bending rod in the flow field. Since a slightly bending rod is even more susceptible to flow instability than a rigid rod, as predicted by Subbotin, tumbling may still exist in this type of thermotropic LCPs. Unfortunately, monodomain experiments on commercial thermotropes are not realistic to pursue due to their poor thermal stability, yet long annealing time inside the magnetic field is necessary to prepare monodomains. Thus, a suitable "bridge" material that can mimic the molecular characteristics of commercial thermotropes is key to definitely classify whether they are flow-aligning or tumbling.

Another issue requires future efforts concerning the evolution of defects and disclinations in the flow field. A better understanding of disclination dynamics will shed light on theoretical modeling to predict stress and orientation development during processing flows, which would ultimately lead to rational design and control of material properties for final products. For tumbling lyotropic LCPs, the relevant length scale for determining the director response to applied flow field is associated with the density of defects. This texture length scale is refined in response to increasing shear rates. A different response is expected for shear aligning thermotropic LCPs as shear promotes macroscopic alignment throughout the sample. However, the inherent turbidity of thermotropic LCPs prevents the use of optical techniques (e.g., microscopy and light scattering) to study the defect structure. As a result, it is not even clear how the domain size varies with shear rate, as well as how defects evolve under flow. One possible avenue of future research is to investigate the disclination in a thin film, for example, a free-standing thin film, using surface microscopy.